

AD-A227 979  
DTIC FILE COPY

REPORT DOCUMENTATION PAGE			Form Approved OMB No. 0704-0188
<small>Public reporting burden for this collection of information is estimated to average 1 hour per response, including the time for reviewing instructions, searching existing data sources, gathering and maintaining the data needed, and completing and reviewing the collection of information. Send comments regarding this burden estimate or any other aspect of this collection of information, including suggestions for reducing this burden, to Washington Headquarters Services, Directorate for Information Operations and Reports, 1215 Jefferson Davis Highway, Suite 1204, Arlington, VA 22202-4302, and to the Office of Management and Budget, Paperwork Reduction Project (0704-0188), Washington, DC 20503</small>			
1. AGENCY USE ONLY (Leave blank)	2. REPORT DATE August 1990	3. REPORT TYPE AND DATES COVERED <del>XXXXXX</del> /DISSERTATION	
4. TITLE AND SUBTITLE Damage Processes and Fracture Surface Morphology in Laminated Composites		5. FUNDING NUMBERS	
6. AUTHOR(S)  Bryan H. Fortson			
7. PERFORMING ORGANIZATION NAME(S) AND ADDRESS(ES)  AFIT Student Attending: Georgia Institute of Technology		8. PERFORMING ORGANIZATION REPORT NUMBER  AFIT/CI/CIA-90-025D	
9. SPONSORING / MONITORING AGENCY NAME(S) AND ADDRESS(ES)  AFIT/CI Wright-Patterson AFB OH 45433-6583		10. SPONSORING / MONITORING AGENCY REPORT NUMBER	
11. SUPPLEMENTARY NOTES			
12a. DISTRIBUTION / AVAILABILITY STATEMENT Approved for Public Release IAW 190-1 Distributed Unlimited ERNEST A. HAYGOOD, 1st Lt, USAF Executive Officer		12b. DISTRIBUTION CODE	
13. ABSTRACT (Maximum 200 words)			
<div>DTIC ELECTE NOV 02 1990 S B D</div>			
14. SUBJECT TERMS		15. NUMBER OF PAGES 179	
		16. PRICE CODE	
17. SECURITY CLASSIFICATION OF REPORT	18. SECURITY CLASSIFICATION OF THIS PAGE	19. SECURITY CLASSIFICATION OF ABSTRACT	20. LIMITATION OF ABSTRACT

**DAMAGE PROCESSES  
AND FRACTURE SURFACE MORPHOLOGY  
IN LAMINATED COMPOSITES**

**A THESIS**

Presented to

The Academic Faculty

by

Bryan H. Fortson

In Partial Fulfillment

of the Requirements for the Degree

Doctor of Philosophy

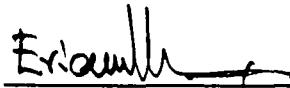
in the School of Aerospace Engineering

Georgia Institute of Technology

August 1990

**DAMAGE PROCESSES  
AND FRACTURE SURFACE MORPHOLOGY  
IN LAMINATED COMPOSITES**

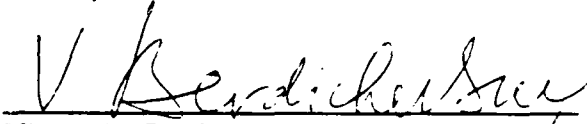
Approved:



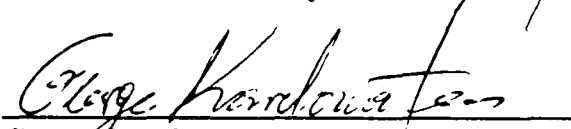
Erian A. Armanios, Chairman



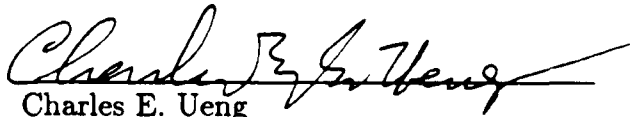
Stephen D. Antolovich



Victor L. Berdichevsky



George Kardomateas



Charles E. Ueng

Date approved by Chairman: 8/17/90

Accession For	
NTIC DCA&I	<input checked="" type="checkbox"/>
DTIC TAB	<input type="checkbox"/>
Unannounced	<input type="checkbox"/>
Justification	
By	
Distribution/	
Availability Codes	
Dist	Avail and/or Special
A-1	

## ACKNOWLEDGEMENTS

The author would like to thank his thesis advisor, Dr. Erian A. Armanios, for his technical guidance and his patient support of this work. Dr. Armanios always knew when I needed help, and when I could benefit from working a problem out myself. His positive attitude was invaluable in keeping my own attitude optimistic.

Thanks are also due to my first thesis advisor, Dr. Lawrence W. Rehfield, for the leadership that he provided during the first two years of my graduate studies.

The Air Force Institute of Technology's Civilian Institutions Program funded my graduate study for its entire four-year duration. I would like to thank my Program Managers, Captain Joseph Krawtz, Captain Gaylene Ujcik, and Captain Steven Payne, for their support and assistance.

In addition, major funding for this work was provided by the Army Research Office, under contract DAAL03-88-C-0003.

The Advanced Structures Group assembled by Drs. Rehfield and Armanios provided me with an atmosphere of dedication and camaraderie in which to conduct my work, and I would like to express my appreciation to each and every one of them.

Special thanks are due to graduate students Graham Webb and Tom Breunig, of the School of Materials Engineering at Georgia Tech, and Koi Marcucelli, of the School of Aerospace Engineering, who took time from their own projects to provide me with invaluable training in the use of equipment. I would also like to express

my gratitude to Mr. Richard Brown, of the School of Materials Engineering, for his help with the testing phase of this research, and to Mr. Robert Sigman, of the School of Aerospace Engineering, for important assistance on short notice.

Thanks are due to Dr. Steven J. Hooper, of Wichita State University, who supplied the Advanced Structures Group with the finite element code GAMNAS, and to Dr. John Masters of the American Cyanamid Corporation, who supplied many fractured specimens for study. Technical discussions with Dr. W.S. Johnson of NASA-Langley were very helpful during the testing phase, and are gratefully acknowledged.

Finally, I would like to thank my wife, Michele, for her constant support over the past two years, and my parents, Mr. and Mrs. C. Charles Fortson, without whose two decades of sacrifice this work would not have been possible.

## TABLE OF CONTENTS

	<u>Page</u>
ACKNOWLEDGEMENTS . . . . .	i
LIST OF TABLES . . . . .	vi
LIST OF ILLUSTRATIONS . . . . .	viii
LIST OF SYMBOLS . . . . .	xiv
SUMMARY . . . . .	xx

### Chapter

I. INTRODUCTION . . . . .	1
II. LITERATURE SURVEY . . . . .	5
2.1 Introduction	
2.2 Descriptions of Delamination	
2.3 Analyses of Short-Beam Tests	
2.4 Relevant Work in Materials Science	
2.5 Survey of Composite Specimen Geometries	
2.6 Summary	

III. FRACTURE BEHAVIOR OF THE SHORT-BEAM	
COMPOSITE SPECIMEN . . . . .	31
3.1 Introduction	
3.2 Background: The Three-Point Bend Test	
3.3 General Failure Analysis	
3.3.1 Specimen Design and Testing	
3.3.2 Numerical Methods	
3.3.3 Results of Numerical Analysis	
3.3.3.1 Stress Maps	
3.3.3.2 Failure Predictions	
3.3.3.3 Strain Energy Release Rate Analysis	
3.3.4 Results of Fractographic Analysis	
3.3.5 Summary of Fracture Analysis	
IV. A STRAIN ENERGY RELEASE RATE MODEL FOR THE	
SHORT-BEAM COMPOSITE CONFIGURATION . . . . .	70
4.1 Introduction	
4.2 Analytical Methods: Williamss Approach	
4.2.1 Revision for Laminated Plates	
4.2.2 Development of Bending Model	
4.2.3 Contact Stress Model	
4.3 Results and Discussion	
4.4 Conclusions	
4.5 Closing Remarks	
V. FRACTOGRAPHY OF THE CRACKED LAP SHEAR	
CONFIGURATION . . . . .	106
5.1 Introduction	
5.2 Specimen Configurations and Testing	

5.3 Quantitative Fractography and Statistical Analysis	
5.3.1 Point Counting	
5.3.2 Statistical Approach	
5.3.3 Specimen Preparation	
5.3.4 Fractographic Approach	
5.4 Results and Discussion	
5.4.1 Quantitative Fractography Results	
5.4.2 Mechanical Crack Propagation Model	
5.5 Closure	
VI. CONCLUSIONS AND RECOMMENDATIONS . . . . .	163
6.1 The Short Beam Specimen	
6.2 The Cracked Lap Shear Specimen	
Appendix: Development of the Sublaminar Model . . . . .	167
REFERENCES AND NOTES . . . . .	172
VITA . . . . .	179



## LIST OF TABLES

	<u>Page</u>
1. Dimensions of Quasi-Isotropic Short-Beam Specimen . . . . .	34
2. Physical Properties Of Short-Beam Specimen Constituent Materials . . . . .	36
3. Failure Loads of Quasi-Isotropic Short-Beam Specimens . . . . .	37
4. Locations of Failure of Short-Beam Specimens . . . . .	45
5. Typical Data for CLS Specimens . . . . .	108
6. Precracking Histories of AS4/PEEK Specimens, In Chronological Order . . . . .	111
7. Locations and Loads of Crack Arrests in AS4/B501-6 Specimens . . . . .	113
8. Locations and Loads of Crack Arrests in In-House AS4/PEEK Specimens . . . . .	113

9. Locations and Loads of Crack Arrests in AS4/BP907 Specimens . . . . .	114
10. Locations and Loads of Crack Arrests in AS4/PEEK Specimens . . . . .	115
11. Example Point-Count Data Set . . . . .	127
12. Locations of Statistically-Significant Morphology Changes in AS4/B501-6 Specimens . . . . .	130
13. Locations of Statistically-Significant Morphology Changes in AS4/BP907 Specimens . . . . .	137
14. Locations of Statistically-Significant Morphology Changes in AS4/PEEK Specimens . . . . .	143
15. Specifications of Specimen in Mechanical Crack Propagation Model . . . . .	157
16. Hypothetical Data Illustrating Derivation of $\Delta a$ vs. $a$ Curve . . . . .	160

## LIST OF ILLUSTRATIONS

	<u>Page</u>
1. Schematic of Laminated Plate Under Load . . . . .	7
2. The Three Fracture Modes . . . . .	10
3. The Short-Beam Shear Test . . . . .	12
4. Photo of a Short Beam Test . . . . .	14
5. Stress Field Around Fibers in a Laminate Under Transverse Loading, as Investigated By Reference 35 . . . . .	18
6. The Cracked Lap Shear Specimen . . . . .	21
7. Load-Displacement Trace of a CLS Specimen . . . . .	23
8. The Double Cracked Lap Shear Specimen . . . . .	24

9. The Double Cantilever Beam Specimen . . . . .	25
10. The End-Notched Flexure Specimen . . . . .	26
11. The Reeder-Crews Specimen . . . . .	28
12. Schematic of the EAL Mesh . . . . .	39
13. The Zero-Length Element . . . . .	40
14. Schematic of Mesh for the GAMNAS Model . . . . .	42
15. Ply and Interface Numbering . . . . .	44
16. Failed Short Beam Specimens . . . . .	46
17. Map of Peel Stress . . . . .	47
18. Map of Chordwise Stress . . . . .	48
19. Map of Shear Stress . . . . .	50
20. Map of Maximum Fraction of Critical Strain . . . . .	51
21. Map of Fraction of Critical Strain Due to Chordwise Stresses . . . . .	52
22. Map of Fraction of Critical Strain Due to Peel Stresses . . . . .	53
23. Map of Fraction of Critical Strain Due to Shear Stresses . . . . .	54
24. The First McCleskey Failure Mode . . . . .	56

25. Modelling of the First McCleskey Failure Mode . . . . .	57
26. The Second McCleskey Failure Mode . . . . .	58
27. Map of Nearness to Failure, Incorporating McCleskey Failure Modes . . . . .	60
28. Map of Fraction of Critical Strain Due to First McCleskey Failure Mode . . . . .	61
29. Map of Fraction of Critical Strain Due to Second McCleskey Failure Mode . . . . .	62
30. Strain Energy Release Rate Data from EAL . . . . .	64
31. Photomicrograph of Crack Beneath Load Nose . . . . .	65
32. Photomicrograph of Small Cracks Beneath Load Nose . . . . .	67
33. Matrix Failure of a 45° Ply . . . . .	68
34. Williamss Analysis of a Cracked Laminate . . . . .	72
35. Half Beam with Contact Stress Field and Centered Flaw . . . . .	84
36. The $r - \theta$ Coordinate System . . . . .	86
37. Strain Energy Release Rate Comparison for a Quasi-Isotropic Beam, Using Strength of Materials Model . . . . .	91
38. Strain Energy Release Rate Comparison for a Unidirectional Beam, Using Strength of Materials Model . . . . .	92

39. Shear Stress Distribution Near Crack Tip, Crack Located 14 Interfaces Below Midplane . . . . .	94
40. Shear Stress Distribution Near Crack Tip, Crack Located 14 Interfaces Above Midplane . . . . .	95
41. Chordwise Stress Distribution Near Crack Tip, Crack Located 14 Interfaces Below Midplane . . . . .	96
42. Chordwise Stress Distribution Near Crack Tip, Crack Located 14 Interfaces Above Midplane . . . . .	97
43. Chordwise Stress Map of Cracked Specimen . . . . .	98
44. Peel Stress Map of Cracked Specimen . . . . .	99
45. Shear Stress Map of Cracked Specimen . . . . .	100
46. Strain Energy Release Rate Comparison for a Quasi-Isotropic Beam, Using Contact Stress Model . . . . .	101
47. Strain Energy Release Rate Comparison for a Unidirectional Beam, Using Contact Stress Model . . . . .	102
48. Strain Energy Release Rate Comparison for a Quasi-Isotropic Beam, Using Contact Stress Model . . . . .	103
49. Non-Straight Crack Front in the DCLS Specimen . . . . .	110
50. Schematic of Point Counting . . . . .	117
51. Point-Count Marching . . . . .	118
52. Specimen Sectioning Plan . . . . .	122

53. Triaxial Stress State Near Edges of CLS Specimens . . . . .	124
54. The Four Fracture Modes . . . . .	126
55. Mode I Failure of Brittle Matrix Composite . . . . .	129
56. Mode II Failure of Brittle Matrix Composite . . . . .	129
57. Comparison of Crack Arrests and Morphology Changes for Specimen A . . . . .	132
58. Comparison of Crack Arrests and Morphology Changes for Specimen B . . . . .	133
59. CLS Specimen, Showing Bands of Different Shades on Surface . . . . .	135
60. Comparison of Crack Arrests and Morphology Changes for Specimen GD-7 . . . . .	138
61. Comparison of Crack Arrests and Morphology Changes for Specimen GD-8 . . . . .	139
62. Comparison of Crack Arrests and Morphology Changes for Specimen GD-2 . . . . .	141
63. Comparison of Crack Arrests and Morphology Changes for Specimen L-10 . . . . .	142
64. Interface Failure near Crack Starter in AS4/PEEK CLS Specimen . . . . .	144
65. Highly Ductile Failure in AS4/PEEK CLS Specimen . . . . .	145
66. Ductile Failure in AS4/PEEK CLS Specimen, Showing Shorter Fibrils . . . . .	146

67. Variation of Matrix Layer Thickness Along Crack Plane of CLS Specimen, Near Crack Starter . . . . .	147
68. Probability Distribution for the Number of Statistically-Significant Variations, Assuming Random Data . . . . .	150
69. Schematic Side View of CLS Specimen . . . . .	152
70. $G$ versus $\Delta a$ for CLS Specimen at Several Initial Crack Lengths . . . . .	156
71. $\Delta a$ versus $a$ for AS4/BP907 Specimens Tested By General Dynamics . . . . .	159
72. Notation and Sign Convention for a Generic Sublaminar . . . . .	169



## LIST OF SYMBOLS

- $a$  half the length of a centered crack in a three-point bend specimen
- $[A]$  matrix in 2-D sublaminar analysis
- $A$  cross-sectional area of a beam
- $A_{ij}$  laminate extensional stiffnesses
- $[B]$  matrix in 2-D sublaminar analysis
- $B$  width of a beam
- $B_{ij}$  laminate coupling stiffnesses
- $c$  distance from the central load to either support of a three-point bend specimen
- $C_0$  a function of the vertical position of a centered crack in a three-point bend specimen
- $[C]$  matrix in 2-D sublaminar analysis
- $C_0$  constant determined by specimen geometry
- $d$  thickness of coating on SEM specimen, in Angstroms
- $da$  increment of crack growth
- $D_{ij}$  laminate bending stiffnesses
- $D_{ij}$  number calculated when using Mann-Whitney U-test improved to accommodate ties
- $E_{ii}$  extensional moduli, where  $i = 1, 2, 3$

- $\{f\}$  the column vector  $\{\alpha_y \quad -q \quad m_y\}$
- $\bar{F}_i$  components of the force in a zero-length element in a finite-element analysis
- $F_i$  components of body force per unit mass
- $F_{total}$  the resultant chordwise force applied to one half of a three-point bend specimen due to the central load
- $G$  smeared shear modulus of a beam
- $G_{ij}$  shear moduli, where  $i = 1, 2, 3$ , and  $j = 1, 2, 3$ , and  $i \neq j$
- $G_I$  mode I strain energy release rate
- $G_{Ic}$  mode I fracture toughness
- $G_{II}$  mode II strain energy release rate
- $G_{IIc}$  mode II fracture toughness
- $G_M$  strain energy release rate due to moments
- $G_{oc}$  strain energy release rate required for delamination
- $G_P$  strain energy release rate due to lengthwise loads in a beam
- $G_T$  total strain energy release rate
- $h$  thickness of a laminate
- $H_{ij}$  material constants
- $J$  the Reissner functional
- $k$  a constant used in determining the coating thickness on an SEM specimen;  
 $k = 5$  for specimens coated in a argon environment;  $k = 2$  for specimens coated in nitrogen or air
- $K_0$  a constant determined by the loading, elastic properties, and geometry of a beam
- $KV$  voltage, in kilovolts, used in coating an SEM specimen
- $L$  one half the length of a beam
- $L(\theta)$  a function of  $\theta$  and  $S_{ij}$
- $m_1, m_2$  effective distributed moments
- $M$  a large, arbitrary constant
- $M_{ij}$  moment resultants;  $M_{i,}$  is abbreviated  $M_i$

$M_T$  total moment applied on a  $y$ -face of a beam  
 $M_w$  molecular weight of a polymer  
 $MA$  current, in milliamperes, used in coating an SEM specimen  
 $n_1, n_2$  population sizes for the Mann-Whitney U-test  
 $n_0$  total number of trials  
 $N$  number of layers considered in Pagano's analysis  
 $\mathcal{N}$  number of plies in a laminate  
 $N_{ij}$  normal stress resultants;  $N_{ii}$  is abbreviated  $N_i$   
 $p_i$  stress vector components  
 $\bar{p}_i$  functions defining forced traction boundary conditions  
 $p_0$  probability of a successful trial  
 $P$  magnitude of an applied point load  
 $P(y)$  approximating function for a point load  
 $PPD$  number of grid points lying on defects  
 $PPI$  number of grid points lying on interface failure regions  
 $PPM$  number of grid points lying on matrix microcracking regions  
 $PPS$  number of grid points lying on regions of shearing failure  
 $q$  an effective lateral pressure  
 $Q$  shear force in a beam  
 $Q_{ij}$  transformed reduced stiffnesses  
 $Q_y$  shear stress resultant  
 $r$  a radial coordinate centered at the point of application of the central load  
to a three-point bend specimen  
 $R$  load ratio of a fatigue test  
 $\mathcal{R}$  a material constant  
 $R_1$  number used in calculating Mann-Whitney  $z$ -statistic  
 $R_O$  Ramberg-Osgood constant  
 $\{\bar{R}(s)\}$  column vector defined in equation 85  
 $s$  independent variable in Laplace transforms

- $S_{ij}$  composite compliances
- $t$  number of ties in two data sets compared by Mann-Whitney U-test
- $t_c$  time, in minutes, used in coating an SEM specimen
- $t_{tab}$  thickness of fiberglass layers
- $t_{total}$  depth of beam
- $T_g$  glass transition temperature
- $u^0, v^0$  midplane displacements of a beam
- $U, V, W$  functions used in sublaminar analysis
- $U_e$  external work performed during crack extension
- $U_s$  strain energy
- $U_T$  number calculated when using Mann-Whitney U-test improved to accommodate ties
- $u_i$  displacement components
- $\bar{u}_i$  functions defining forced displacement boundary conditions
- $w$  out-of-plane deflection of a plate in bending
- $W_0$  deflection of three-point bend specimen at the center
- $x, y, z$  coordinate system frequently used for laminated plates
- $x_0$  number of statistically-significant morphology changes observed
- $\{X\}$  the column vector  $\{V \quad W \quad \beta_v\}^T$
- $\{\bar{X}(s)\}$  the Laplace transform of  $\{X\}$
- $Z$  a z-statistic, by definition normally-distributed
- $z_0$  z-coordinate of the interface between two plies in a laminate
- $Z_T$  normally distributed statistic resulting from Mann-Whitney U-test improved to accommodate ties
- $\alpha$  the ratio of the mode I strain energy release rate to the total strain energy release rate
- $\alpha_1, \alpha_2$  are effective distributed axial forces
- $\beta$  a geometric constant
- $\beta_1, \beta_2$  rotation terms

- $\delta_1, \delta_2$  geometric constants
- $\Delta_i$  components of the separation of the nodes of a zero-length element in a finite element analysis
- $\epsilon$  a uniform axial strain
- $\epsilon_{ij}$  strain components
- $\eta$  a coordinate
- $\eta_1, \eta_2$  functions of  $C_0$  and  $S_{ij}$
- $\gamma^{(k)}$  functions of integration for shear stress continuity in a laminate
- $\Gamma$  a function of  $\eta_1$  and  $\eta_2$
- $\kappa$  constant determined by the cross-sectional geometry of a beam
- $\lambda_1, \lambda_2$  roots of the characteristic equation  $S_{11}\lambda^4 - (2S_{12} + S_{66})\lambda^2 + S_{22} = 0$
- $\lambda_i$  a material constant
- $\mu_m$  a constant
- $\mu_U$  mean of distribution resulting from Mann-Whitney U-test
- $\mu_T$  mean of distribution resulting from Mann-Whitney U-test improved to accomodate ties
- $\nu_{ij}$  Poisson's ratio, where  $i = 1, 2, 3$ , and  $j = 1, 2, 3$ , and  $i \neq j$
- $\Omega_k$  region defining the top surface of the  $k$ -th layer of a laminated plate
- $\Omega_k^o$  portion of  $\Omega_k$  where neither traction boundary conditions nor displacement boundary conditions are applied
- $\phi$  inclination angle of a plate in bending
- $\varphi$  Ramberg-Osgood exponent
- $\Psi$  a contraction introduced in equation (A - 15)
- $\rho$  mass density of a body
- $\sigma_i$  normal stress components
- $\sigma_{ij}^{(k)}$  shear stress components in the  $k$ -th layer of a laminate
- $\sigma_T$  standard deviation of distribution resulting from Mann-Whitney U-test improved to accomodate ties
- $\sigma_U$  standard deviation of distribution resulting from Mann-Whitney U-test

$\tau_{ij}$  shear stress components

$\tau_I$  interlaminar shear stress in a short-beam shear test at failure

$\theta$  orientation angle of plies in a laminate

$\Upsilon_0$  complementary energy density

$\xi$  geometric constant

$\pi = 3.14159\dots$

$\zeta$  a coordinate

## SUMMARY

Because of the complex mechanical behavior of laminated composite materials, the failure processes of these materials are often ill-understood. This is of particular importance when the issue of composite fracture testing is considered. Without an adequate understanding of why a laminate fails, there is the danger of producing useless data, along with the greater danger of being guided by that data. Clearly, it is highly important to understand *how* laboratory specimens fail.

This work encompasses in-depth examination of the failure mechanisms of two widely-used composite laminate configurations: the three-point short-beam bend test, used to characterize the interlaminar shear strength of a composite, and the cracked lap shear test, which is used to determine critical strain energy release rates for delamination, and to characterize resistance to delamination growth. These configurations have been analyzed and modelled as structures, in order to gain detailed understanding of their behavior during testing. Particular emphasis has been placed upon three areas. The first is the correlation between the observed morphology of the fracture surface and the predicted and actual data produced by the configuration during testing. The second area is the identification of the actual damage modes leading to failure. The third area is the way in which these damage modes interact to cause final failure. *(SDW) ✓*  
*these*

The short-beam three-point bend configuration was analyzed for the case of a quasi-isotropic layup, a layup of great practical importance. The analysis reveals that the laminate does not fail in interlaminar shear, as is assumed. Rather, failure is due to a combination of damage modes, all driven by excessive local strain of the

material. Analyses based upon fracture mechanics and the critical strain criterion have been developed in order to predict the configuration behavior. It is found that the fundamental assumptions undergirding this test do not apply to the case examined.

The fracture mechanics analysis described above produced data concerning the variation of the strain energy release rate associated with assumed flaws in a short-beam specimen, as a function of their vertical location. The construction of a simple model to explain this data was attempted. Two models were tried: one that modelled the short-beam specimen as a beam in bending, and one that modelled it as a semi-infinite body under a point load. Surprisingly, the first model produced poor agreement with the finite element data, while the second produced good agreement, qualitatively and quantitatively. The significance of this result is twofold. First, the analysis of the configuration behavior is seen to be more like a contact stress problem than a bending problem, from a fracture mechanics point of view. Second, a model is constructed that produces accurate results in closed form, reproducing the results of protracted and expensive finite element analyses.

The first stage of the CLS investigation centered around quantitative fractography. The fracture surfaces of failed CLS specimens were examined using a scanning electron microscope, and point-counting techniques were combined with statistical analysis to locate significant variations in the morphology of the fracture surface. These locations of significant morphology changes were compared to the locations of crack arrest during testing. The correlation was observed to be poor. However, a further statistical analysis indicated that the point-counting was probably measuring some physical property of the specimens. This property is found to be the variation in the thickness of the matrix layer along the crack plane. The absence of a link between fracture morphology and crack arrest suggests that arrest is driven by purely mechanical considerations.

The findings of this research emphasize the importance of understanding the fracture behavior of test configurations before interpreting data from them. Most



importantly, the fracture characteristics described herein have applications to other test configurations, laying the ground for further inquiry and for practical use of the techniques and characteristics detailed in this work.

## CHAPTER I:

### INTRODUCTION

Advanced organic-matrix composite materials are of greater interest than ever to the aerospace industry, especially in high-performance applications. Press<sup>[1]</sup> notes that the United States production of advanced structural materials, such as composites and ceramics, is currently about 2 billion dollars per year, and is expected to grow to 20 billion dollars per year within a decade. The impact of advanced materials extends to performance, as well as economics. Ratwani<sup>[2]</sup>, reviewing historical data and future trends, anticipates that well over half of the cumulative reduction in the structural weight of American fighter aircraft between the years 1950 and 2010 will be due to advances in materials technology. While developments in metallurgy produced most of the gains of the 1950's, advanced composites have been the most promising structural materials technology, in terms of weight savings, since their advent in the 1960's.

There are many examples of the importance of laminated composite materials in the aerospace industry and for the national defense. The high specific stiffness, strength, and design flexibility of composites made possible the forward-swept wing of the X-29 experimental aircraft. The F-117A stealth fighter and the B-2 stealth bomber owe their radar-evading capabilities largely to their composite skins. Com-

posite materials were instrumental in the design of the tilt-rotor V-22 Osprey, an aircraft that may assume much greater importance as preparation for low-intensity conflicts plays a greater role in American defense strategy. Composite components are being moved into aircraft such as the AV-8B attack plane, the C-130, C-141, and Boeing 767 transports, and the F-15 fighter, to take advantage of their light weight and their excellent corrosion and fatigue properties. The United States is not the only nation to recognize the potential of advanced composites in military aircraft: the British Jaguar fighter has incorporated advanced composite components, as has the joint British-West German built Tornado fighter; additionally, Sweden's Saab Aerospace has begun using advanced composite materials in its military aircraft.<sup>[3]</sup> In 1986, the all-composite *Voyager* set the record for nonstop flight around the world. Having played so prominent a role in so many of the most exciting developments of modern aeronautics, composites are clearly one of the most exciting technologies in the aerospace field.

In addition, composites technology can be made cost-effective. While composite materials can be expensive, and the front-end cost of manufacturing with them is high, these disadvantages can be greatly outweighed by gains due to increased automation of production, assembly savings due to reduced need for fasteners, more efficient final forming due to near-net-shape technology, and resulting decreases in labor costs. In summary, the performance and cost efficiency of composites make them attractive materials for use as primary structures in high performance applications.

Nonetheless, composites do have their challenges. They are vulnerable to environmental effects such as high temperatures, moisture, ultra-violet radiation, and lightning strikes. Laminated composites are very weak in the direction normal to the plies, so they are used as plates, shells, thin-walled members, and other applications in which triaxial stress states are not predominant. However, they have complicated modes of failure, and are difficult to analyze. As a result, the mechanical behavior of many test configurations is not well understood.

A specific challenge of composite mechanics arises when in-plane loads give rise to interlaminar stresses which cause separation of layers, or delamination. These stresses, caused by Poisson's ratio and inplane shear stiffness mismatches and by differences in the coefficients of moisture and thermal expansion between plies, arise at ply terminations, cutouts, holes, voids, and free edges. Delamination plays a role in many types of composite failure, from the buckling of a stiffened structure to the failure of a helicopter rotor hub. It can be a problem whether a composite is in tension or compression, bending or torsion, so it is an issue of importance in virtually every composite application. Understanding delamination, and its interaction with other damage modes, in order to develop a design philosophy that will minimize it, is the purpose of this effort.

Delamination must be considered both as a mechanics problem and as a materials problem. Only by detailed analytical work on the mechanics of delamination can the stress state of the composite be understood, and only by an understanding of the composite's material behavior under this stress state can an effective design philosophy be implemented. Thus, fractography and mechanics must be integrated to present a complete picture of the delamination phenomenon, and its interaction with other damage modes.

However, higher-order type analyses are frequently time-consuming, and thus inconvenient for the practicing engineer. This is especially true in designing with composites, because their complex mechanical behavior often makes simple closed-form solutions unfeasible for even the least complicated problems. Thus, there is a need for approaches to composite mechanics problems that will give adequate answers, and help to identify the parameters controlling the behavior, without requiring extensive computational effort. While progress has been made in this area, there is still a great demand for simpler tools for the design engineer.

Furthermore, some basic composite test configurations remain poorly understood. The processes assumed to lead to failure of these configurations may not be those actually responsible. In such a case, it is necessary to analyze the configura-

tion in sufficient depth to permit a conclusive statement about its failure modes. Such knowledge will ensure that material characterization data are not based upon erroneous assumptions about specimen behavior.

The general aims of this research are twofold: development of an in-depth model to explain delamination growth rates and their interaction with other damage modes, and development of a simple model to predict composite failure effectively and quickly. The first aim will involve both analytical mechanics and materials science, as fractographic analyses are used to form and support an analytical model of a specific laminate configuration. The second aim will be predominantly analytical, as models are developed to explain the behavior of previously-failed short beam specimens. The methods developed will be judged by accuracy of solution, speed of calculation, and ease of use. Comparisons will be made to results from laboratory testing and finite element analyses.

## CHAPTER II:

### LITERATURE SURVEY

#### 2.1. INTRODUCTION

The problem of composite delamination is a challenge to both the mathematical analyst and the materials scientist. Exact elasticity solutions to the problem have been developed, but were soon seen to become intractable for all but the simplest cases. Numerical methods also have limitations, due largely to the high stress gradients found near the free edges of composite specimens. Accurate modelling of these regions requires an extensive computational effort, and it is precisely these regions that are the sites of most delaminations. The first part of this chapter provides a history of the development of these numerical methods, a review of currently-used approaches, and a discussion of the limitations of the various techniques.

The second part of this chapter concerns analyses of a composite beam under three-point loading. This configuration is often used in quality-control testing, so solutions have been developed for stresses, displacements, and strain energy release rates in this configuration. Standard test methods, and their potential problems,

are reviewed.

The third section concerns background research in materials science. If a composite failure surface is to be analyzed, the researcher must be familiar with the manifestations of the various forms of damage. Such phenomena as matrix microcracking, shear yielding, and fiber-matrix interface failure can be interpreted in terms of the mechanical states that produced them. A survey is made of typical damage modes, their morphological consequences, and quantitative methods.

Finally, other laminate configurations are surveyed, including discussion of their mechanical behavior and limitations in application.

## 2.2. DESCRIPTIONS OF DELAMINATION

Figure 1 shows a schematic of a laminated plate under in-plane loading. All externally-applied loads are in the  $x$ - $y$  plane. Using the coordinate system shown in Figure 1, there are three stress components that would tend to separate the laminae at their interfaces: the shear stresses  $\tau_{xz}$  and  $\tau_{yz}$ , and the normal stress  $\sigma_z$ . In classical laminated plate theory, these stresses are neglected. Unlike conventional isotropic materials, composite materials exhibit mechanical properties that vary with orientation. The directional nature of the composite material's mechanical properties in a laminated composite results in a large extensional modulus along the fiber directions relative to the extensional moduli in the lateral directions and the shear moduli. The result is that the relative importance of physical effects is influenced by the directional nature of the properties and their relative magnitudes. Transverse shear, transverse normal strain, and other effects ignored in classical engineering structural theories are more pronounced for composite structures, and cannot be neglected.

An interesting illustration of the specificity of delamination problems to a given material and ply layup was provided by Chan and Ochoa<sup>[5]</sup>, who demonstrated a significant increase in delamination resistance in composites when a selected ply

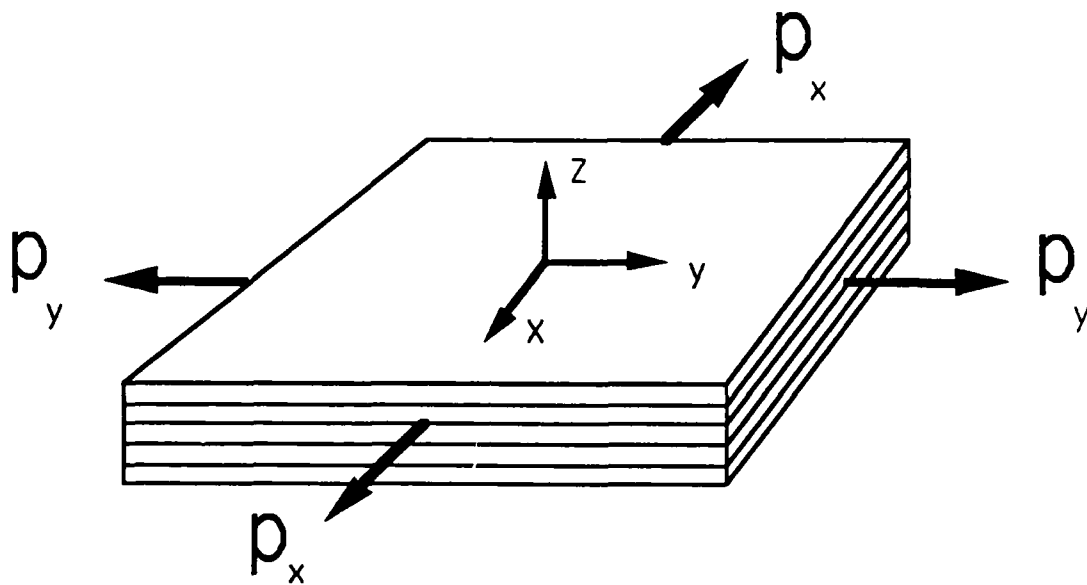


Figure 1: Schematic of laminated plate under load



was terminated near the specimen edge. Reference 5 notes that, when there are 90° plies near the midplane of a laminate, delamination generally takes place at an interface bordering one or more of those 90° plies, due largely to the Poisson's ratio mismatch between the plies on either side of that interface. Terminating a 90° ply just before it reaches the edge of a specimen means that this Poisson's ratio mismatch is not combined with the triaxial stress state near the specimen's edge. Thus, even though this method effectively places a region of weak matrix material in precisely the region where delamination is most likely, it results in a significant improvement of the delamination resistance, because the stress state that leads to delamination has been altered.

In 1970, Puppo and Evensen<sup>[6]</sup> analyzed a simple laminated plate under three specific cases of external loading, modelling the laminate as a stack of anisotropic layers separated by anisotropic shear layers. Their analysis showed that  $\tau_{xz}$  was largest in magnitude at the free edges of a finite plate, while the interlaminar shears vanished for an infinite plate. It was noted that if a plate under uniaxial stress was bent about the loading axis to form a tube, the vanishing of the two free edges led to the vanishing of interlaminar shears in the gage section. However, interlaminar shears were still present near the free edges at the grips. Pagano and Pipes<sup>[7]</sup>, using a finite difference technique, produced qualitatively similar results for plates, although their calculations indicated the presence of singularities in  $\tau_{xz}$  at the free edges. Together, these two efforts showed that  $\tau_{xz}$  could not be neglected near the free edges of laminated plates.

In 1973, Pagano and Pipes<sup>[8]</sup> documented the phenomenon of composite failure by catastrophic delamination under uniaxial tension, and argued that such failure was due to the presence of the normal stress  $\sigma_z$ . Later, Pagano and Pipes<sup>[9]</sup> bolstered this argument by analyzing stacking sequence effects on  $\sigma_z$ , which showed that in some cases the normal stress could become quite large. Then Pagano<sup>[10]</sup>, drawing upon the cylindrical bending theory developed by Whitney and Sun<sup>[11]</sup>, developed an approximate solution for  $\sigma_z$  for cross-ply, symmetric laminates.

Figure 2 shows the three basic fracture modes: *opening* (Mode I), *shearing* (Mode II), and *tearing* (Mode III). Note that the presence of  $\tau_{xz}$  near the free edge translates into Mode II loading along the laminar interfaces, and the presence of  $\sigma_z$  translates into Mode I loading along these interfaces. That the Mode I crack extension is most critical in graphite/epoxy composites is indicated by the results of Reddy *et al.*<sup>[12]</sup> and Armanios *et al.*<sup>[13]</sup>, in which considerable improvement in delamination fracture behavior was achieved by applying a normal load to suppress  $\sigma_z$ . Also, Jordan and Bradley<sup>[14]</sup> noted that, for brittle-matrix composites, the Mode II delamination fracture toughness may be as much as three times the Mode I delamination fracture toughness, while in toughened-matrix composites the two delamination fracture toughnesses are roughly equivalent. Techniques such as the stitching or wrapping of free edges are currently in use for this reason, as they suppress the Mode I delamination loading component.

By 1978, according to a survey by Wang and Dickson<sup>[15]</sup>, it had become clear that solving for  $\sigma_z$  for the general laminated plate problem was impractical if closed-form elasticity solutions were used, and the emphasis had turned to the development of appropriate numerical methods. Because of the complexity of the free-edge stress problem, it is natural that finite-element and finite-difference approaches should be attempted. Yet, even these techniques have their limitations, because of the high stress gradients located near the free edges. An illustration of this is provided by the work of Wang and Crossman<sup>[16]</sup>, who attempted to gain a realistic picture of the stress field in a composite laminate by using an extremely fine finite element mesh of 196 elements per layer.

Isakson and Levy<sup>[17]</sup>, using constant-strain elements, achieved good correlation with shear-stress results obtained using basic methods of incorporating shear effects into laminated plate theory. The three-dimensional finite-element solution of Rybicki<sup>[18]</sup> improved upon this analysis. However, the finite element studies cited here produced contradictory stress solutions near the free edges. Also, the edge stresses have been observed to increase with decreasing element size in these

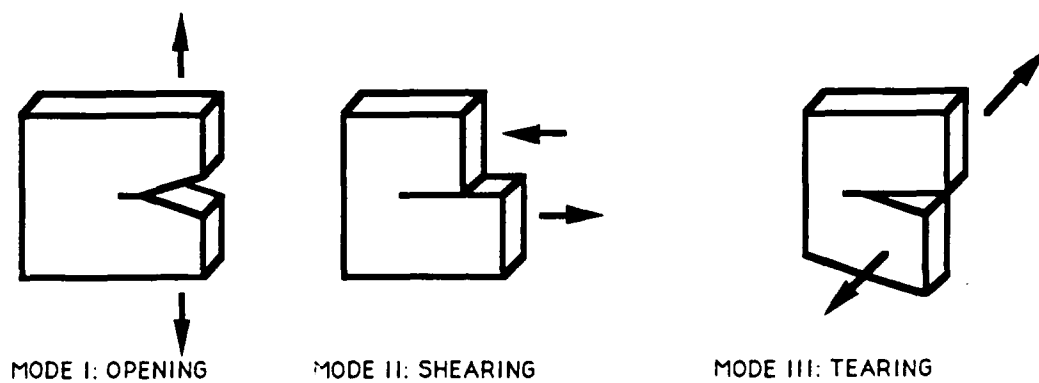


Figure 2: The three fracture modes

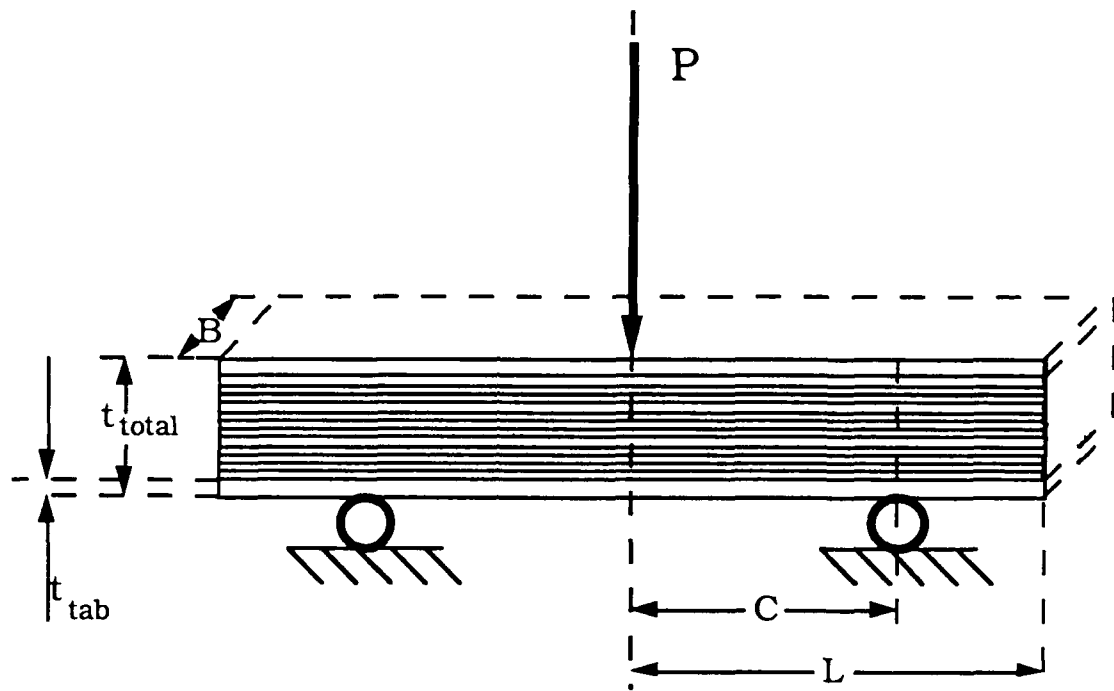
analyses.

Armanios<sup>[19]</sup> and Armanios and Rehfield<sup>[20]</sup> contributed a computationally simple, closed form approach to the problem of edge delamination, using the method of sublaminates analysis. A simplification was introduced in Reference 20 by neglecting thickness strain. The structure is modelled as an assembly of *sublaminates*: groups of plies considered as individual units. Each sublaminate is described by a set of constitutive relations, and by a set of boundary conditions along the edges and interfacial continuity conditions. This approach leads to considerable simplification for laminates with many plies. The result of this analysis is an approach that yields accurate values of interlaminar shear stresses, total energy release rate, and energy release rate components, without the need for involved, expensive numerical analyses. Because of the important role that sublaminate analysis plays in the current effort, an in-depth review of the development of this approach is presented in the appendix.

Dattaguru *et al.*<sup>[21]</sup> developed a geometrically nonlinear finite-element analysis for adhesively-bonded joints, which proved useful for analyzing composite structures. This analysis incorporated nonlinear strain-displacement relations, resulting in nonlinear governing equations that could be solved iteratively. Later, Whitcomb and Dattaguru<sup>[22]</sup> documented a finite-element program called GAMNAS (Geometric and Material Nonlinear Analysis of Structures), which added the capacity for material nonlinearity to the analysis of Reference 21.

### **2.3. ANALYSES OF SHORT-BEAM TESTS**

While the method of References 19 and 20 is much less complex than numerical analyses, there is still a demand for even simpler methods for practical applications. One example of this need is the short beam three-point bend test, shown in Figure 3. This test is commonly used in quality control of composites, but the behavior of the specimen is not well understood.



$$\tau_I = \frac{3P}{4A}$$

Figure 3: The short beam shear test

Reference 23 describes the standard procedure for the short-beam shear test, as it has been used since at least 1969. It is usually a small specimen, and was originally intended for use with unidirectional composites with fibers oriented along the length of the specimen. A typical thickness would be fifteen plies. The test, as described in Reference 23, provides some reasons for concern about its validity. As Figure 4 shows, the specimen aspect ratio is so small that the applicability of Saint-Venant's principle at the failure site is questionable. Furthermore, the test description does not mention the failure mode, raising questions as to how well the specimen's behavior was understood when it was designed. Finally, the interlaminar shear stress at failure is derived from a simple beam-theory analysis, with its assumptions of parabolically-distributed shear stresses and constant shear-force magnitudes away from the loads. It remains to be seen if these assumptions are realistic.

The specimen is assumed to fail by Mode II fracture at the midplane; however, Whitney and Browning<sup>[24]</sup> have observed that unidirectional specimens can exhibit other failure modes, such as compressive buckling near the load nose, or yielding through combined compression and shear. Numerical analyses cast further doubt upon the effectiveness of the short beam test. The elastoplastic finite element analysis of Berg *et al.*<sup>[25]</sup> showed extremely high shear stresses near the load nose, and the finite-difference analysis of Sandorff<sup>[26]</sup> showed that St. Venant's principle is not satisfied in an orthotropic beam of low span-to-depth ratio, with the result that the stress-concentration effects near the load nose and the supports are never dissipated. Furthermore, tests on quasi-isotropic layups, discussed in Reference 19, showed off-midplane cracking, implying mixed-mode failure. Note also that failure is expected to occur in a location where, according to beam theory, stresses should be negligible. This suggests that the mechanics of the short beam specimen cannot be adequately described by a classical beam-type theory. The challenge lies in developing an analysis that is accurate enough to be useful, but simple enough for the design engineer with many candidate layups to examine.

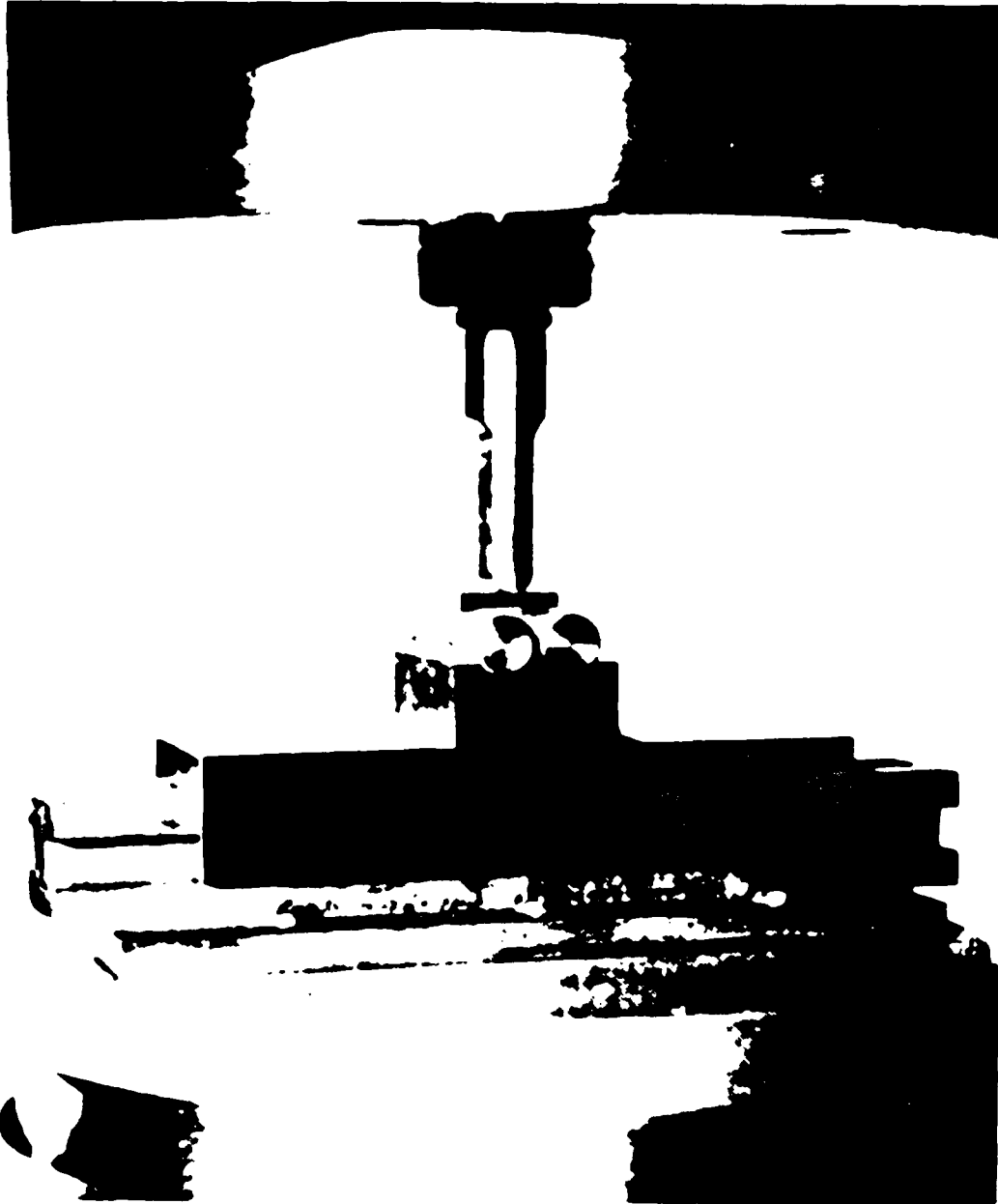


Figure 4: Photo of a short beam test<sup>[23]</sup>

An example of such an approach is the analysis of Whitney<sup>[27]</sup>, who used a series approximation to the loads on a four-point bending specimen to develop a closed-form elasticity analysis of an orthotropic beam. This analysis, which includes three-point bending as a special case, allows the computation of stress and displacement fields without the use of numerical methods, although the series solution converges slowly due to the point loads. Thus, the model is computationally intensive, but much less so than a finite element model. While this approach is limited to beams with smeared properties, it does provide insight into the role of physical parameters in the deformation process, something that a numerical model cannot do.

Also useful is the work of Williams<sup>[28]</sup>, who developed a simple expression for the strain energy release rate of a cracked orthotropic laminate. This analysis, modified to describe arbitrary layups, will be an integral part of the beam theory analysis of the short beam configuration, presented in the third chapter of this work.

## **2.4. RELEVANT WORK IN MATERIALS SCIENCE**

While mechanical analyses are indispensable, they must be combined with knowledge of material behavior if a fracture surface is to be properly interpreted. Thus, it is appropriate to review current knowledge in polymer fracture.

While most analytical approaches to the delamination problem focus on ply-level mechanics, some researchers choose to examine the resin found between layers of the reinforcing fibers. This results in an analogy between the failure of a composite (resin failing between fibers) and the failure of an adhesive bond between two adherends. Lee<sup>[29]</sup>, has observed that this analogy cannot be exact; if it was, the composite fracture toughness would depend entirely upon the fracture toughness of the matrix material, and the observed variation of composite fracture toughness with volume fraction of fibers would not be expected. Reference 29 suggests that the size of the crack tip plastic zone formed in the matrix is critical to the composite fracture toughness, and it is further suggested that the composite fracture toughness



can be divided into two components: one determined by the neat resin properties and layer thickness, and one determined by the residual stresses inside the resin layer. While the presence of two non-derivable constants in Lee's  $G_{Ic}$ -equations makes them as yet unsuitable for predictions, Reference 29 illustrates that ply-level mechanics is not the only analysis being tried for the delamination problem.

Reference 29 also illustrates the importance of plastic deformation near the crack tip during fracture, which is governed by the brittleness or ductility of the polymer. Kausch<sup>[30]</sup> suggests a yield stress of 100 MPa as a dividing line between ductile and brittle resins, noting that resins with higher yield stresses tend to exhibit limited crack-tip plasticity, and thus stable crack propagation, while resins with lower yield stresses may develop enough plastic flow near the crack tip to cause blunting and subsequent arrest. Reference 30 also notes that stable, continuous crack propagation leads to relatively featureless fracture, while crack arrest is usually followed by a striated fracture surface in epoxide resins, polyimides, and phenol-formaldehyde resins. This is in concurrence with the observations of Rosen *et al.*,<sup>[31]</sup> who note that rapid fracture of polymers is manifested by smooth fracture surfaces, while slower initial fracture leads to a rougher surface.

Plastic deformation also bears upon the issue of ductile versus brittle fracture. According to Engel *et al.*<sup>[32]</sup>, there is no brittle fracture in polymers, of the type associated with metal cleavage; fibrils will always be present on the fracture surface, even if they are very small. Reference 32 defines brittle fracture of polymers as occurring when the fibrils are 1  $\mu$ m or less in length. Brittle fracture of this sort is most likely to be found in *thermosetting* resins, the molecular chains of which are cross-linked, restricting them and thus reducing the material's ability to deform. The structure of thermosets causes them to exhibit very little plastic or viscoelastic deformation, resulting in brittle behavior. *Thermoplastic* resins, by contrast, are not cross-linked, and their macromolecules can be stretched and oriented before failure takes place, resulting in much more ductility. However, this process requires time, making the deformation of these materials highly dependent upon strain rate.

Clearly, whether the matrix of a composite is thermoplastic or thermosetting will have a great impact upon its fracture behavior.

One of the more prominent damage modes exhibited by polymers is *crazing*, in which, according to Hertzberg<sup>[33]</sup>, a region of oriented polymer fibrils interspersed with interconnected voids is formed on a plane normal to the applied principal stress. This region is capable of supporting less stress than the surrounding, uncrazed material. However, Bascom *et al.*<sup>[34]</sup>, using Mode I specimens of a unidirectional carbon-fiber composite with AS4/3501-6 resin, determined that shear yielding was the prevalent matrix mode, and do not mention crazing as playing any part. Furthermore, Reference 34 states that the evidence against the presence of crazes in thermosetting resins is strong. Thus, one can assume that crazing will play little, if any, role in the fracture of composites with thermosetting resin matrices.

Newaz<sup>[35]</sup> considered the stress state around a fiber in a unidirectional composite, under transverse loading, as shown in Figure 5, and determined that the fibers would have a maximum radial tensile stress oriented in the direction of applied load, with a maximum radial compressive stress oriented normal to the direction of applied load. Reference 35 adds that there will be a shear stress at the point on the fiber where the radial stress component changes from tension to compression. Considering the peel stress  $\sigma_z$  as a transverse load, it is seen that the fiber will be "peeled out" of the matrix by the tensile load normal to the fracture surface, and that localized shear yielding of the matrix can occur where the radial stress changes sign. Reference 34 notes that yielding can be detected by heating the failed composite above the matrix glass-transition temperature,  $T_g$ , and looking for observable changes in the appearance of the fracture surface due to relaxation of the plastically-deformed areas.

Bascom, Ting *et al.*<sup>[36]</sup> documented localized plasticity effects in a modified epoxy polymer. They discovered localized plastic deformation in the region of initial, slow growth, with much less plastic deformation in the region of rapid fracture. Bascom, Cottingham *et al.*<sup>[37]</sup> observed the same behavior in epoxy- and elastomer-

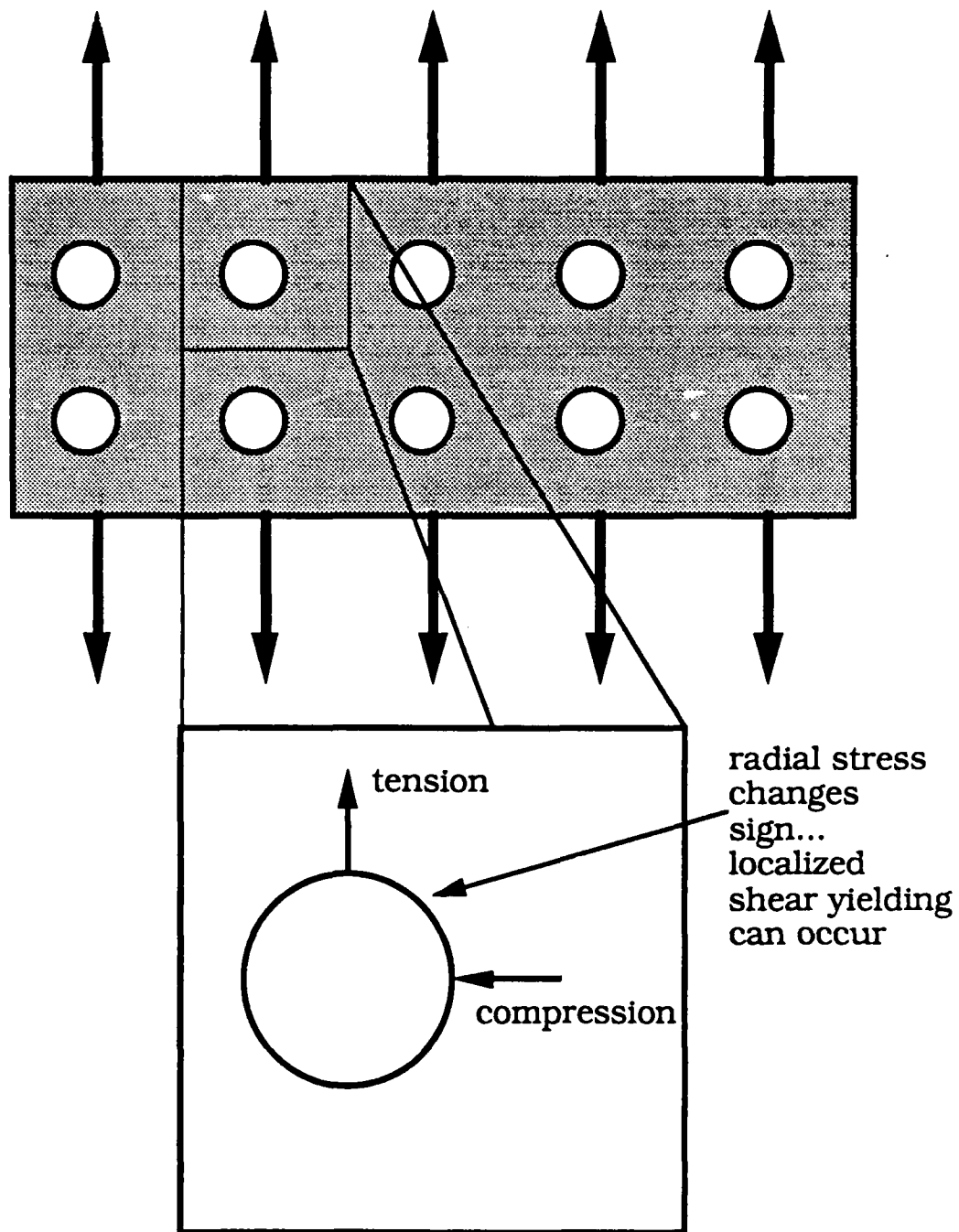


Figure 5. Stress field around fibers in a laminate under transverse loading, as investigated by Reference 35

modified epoxy polymers. It is seen that the role of plastic deformation in delamination failure may be neither negligible nor simple, even for composites with brittle epoxy matrices.

Johannesson *et al.*<sup>[38]</sup> studied the delamination fracture surfaces of angle-ply T300/1034 composites laid up according to  $[\pm\theta]_{2s}$ , with  $\theta \in \{5^\circ, 15^\circ, 30^\circ, 45^\circ\}$ . The specimens were strips cut from rectangular composite sheets and tested in tension. Reference 38 concludes that the fracture surfaces could be divided into resin-rich areas, which showed the imprints of the fibers, and resin-poor areas, which showed the debonded fibers themselves. The resin-rich interlaminar regions originated the cracks, which alternated from one ply to the next during propagation. Serrations were found in the outermost part of the plies on the fracture surface, and these serrations were observed to be tilted in correlation with the direction of the major tensile principal stress. Reference 38 suggests that there are three steps in the delamination fracture process: debonding of fibers, crack opening by  $\sigma_z$ , and linking together of the fractures caused by individual debondings.

Richards-Frandsen and Naerheim<sup>[39]</sup> examined the fracture morphology of an AS/3501-6 graphite-epoxy composite under three-point bending fatigue. The dominant fracture surface features were matrix cleavage, hackle formation, and wear. The wear can be attributed to the cyclic nature of the loading; References 34 and 38, which are concerned with non-fatigue loading, make no reference to wear. In Reference 39, it was determined that defects in the composite did not initiate cracks, but served to enhance crack propagation in their vicinity. Reference 39 also explains the formation of hackles in terms of a local critical shear strength model. For a specimen in bending, shear stresses exist between plies located on opposite sides of the delamination plane. When a critical shearing stress (or strain) is reached in the matrix between the fibers of these two layers, small matrix cracks will form, growing until they reach the fiber-matrix interface. The number of cracks needed to accomodate a given strain is inversely proportional to the distance between the fibers.

The fractography of thermoplastic polymers varies a great deal from material to material. Reference 30 notes that the magnitude of localized plasticity on a thermoplastic fracture surface can be as high as several hundred percent. In some thermoplastics, cleavage fracture cannot be produced at all by bending at room temperature; only situations such as impact loading can induce cleavage. Moreover, the degree of plastic deformation is a function of the molecular weight of the polymer: for some thermoplastics of extremely high molecular weight ( $M_w > 10^6$ ), room-temperature cleavage fracture cannot be produced at all. The reason for this high degree of plasticity lies in the nature of the molecular coils that make up a thermoplastic. Only after the substantial deformation of these coils by a sufficiently large shear displacement can any axial forces be developed; thus, failure can only occur after extensive plastic deformation.

Individual thermoplastic resins have their own peculiar characteristics, making thermoplastic fractography less amenable to generalizations than thermosetting polymer fractography. For example, if a thermoplastic has a spherulitic structure, cleavage fracture can be extensive. Thermoplastics, unlike thermosetting polymers, may exhibit crazing, with the craze pattern providing clues as to the speed of crack propagation. Add to this the molecular-weight effect mentioned earlier, and it is clear that interpretation of thermoplastic fracture surfaces must proceed on a material-by-material basis.

## **2.5. SURVEY OF COMPOSITE SPECIMEN GEOMETRIES**

Several specimens have been developed for laboratory investigation of delamination. The most popular are the cracked-lap-shear (CLS) specimen, the double cracked-lap-shear (DCLS) specimen, the double cantilevered beam (DCB) specimen, and the End Notch Flexure (ENF) specimen. The CLS specimen is shown in Figure 6. It generally exhibits mixed-mode (Mode I and Mode II) crack behavior, in proportions determined by the specimen layup, geometry, material, and loading.

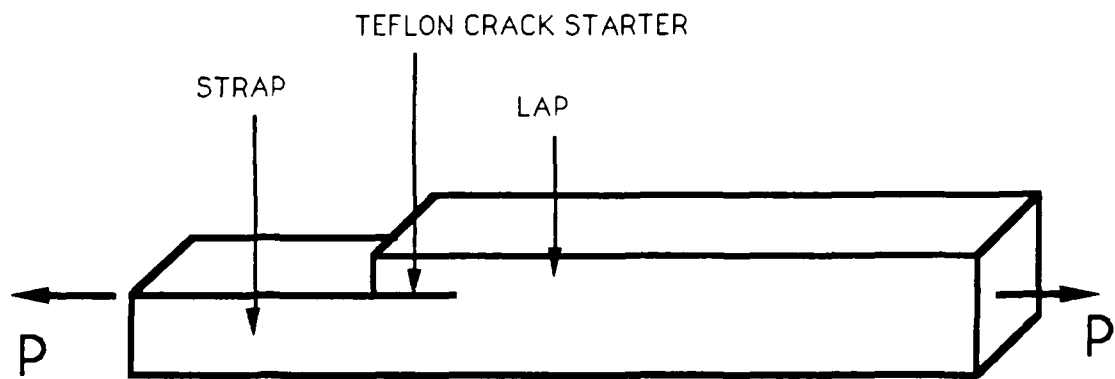


Figure 6: The cracked lap shear specimen

Figure 7 shows a typical load-displacement trace for a CLS specimen for a brittle resin system. Under tensile loading, the specimen exhibits sudden crack growth followed by crack arrest. When the specimen is unloaded and reloaded, the same behavior is observed, with the sudden growth and arrest occurring at an equal or higher load level. Repeating the loading and unloading can produce several crack arrests in the same specimen, as Figure 7 shows.

The DCLS specimen, shown in Figure 8, has the advantage of symmetry over the CLS specimen. Because of this, it does not exhibit the out-of-plane bending response that is observed in the CLS specimen, and which can be troublesome in specimens with few plies. Also, Armanios *et al.*<sup>[40]</sup> have observed that, for quasi-isotropic layups, the DCLS specimen gives less scatter in load-versus-delamination-growth data than does the CLS specimen, as well as a less tortuous crack path. In addition, the DCLS can be loaded to produce pure Mode II behavior, by reversing the loading.

Figure 9, after Hibbs *et al.*<sup>[41]</sup>, shows the DCB specimen. The figure illustrates how the DCB specimen can be loaded to produce pure Mode I, pure Mode II, or mixed-mode crack loading. In Reference 41, it was found that increasing the Mode II loading resulted in increased resistance to the onset of crack propagation, as measured by the total energy release rate required to propagate the crack.

Figure 10 shows the ENF specimen. It is similar to the DCB specimen as shown in Figure 9c, and it produces pure Mode II loading. The use of standard three-point bending fixtures makes this a convenient specimen for experimenters. In addition, as Salpekar *et al.*<sup>[42]</sup> have determined, beam theory leads to reasonably accurate closed-form solutions for compliance and strain-energy-release rates for unidirectional specimens.

Reeder and Crews<sup>[43]</sup> designed an innovative variation on the ENF specimen, which is shown in Figure 11. A lever and hinge apparatus is added to the standard ENF test configuration, resulting in the addition of opening-mode loading. The relative magnitude of the opening- and sliding-mode loads can be determined by

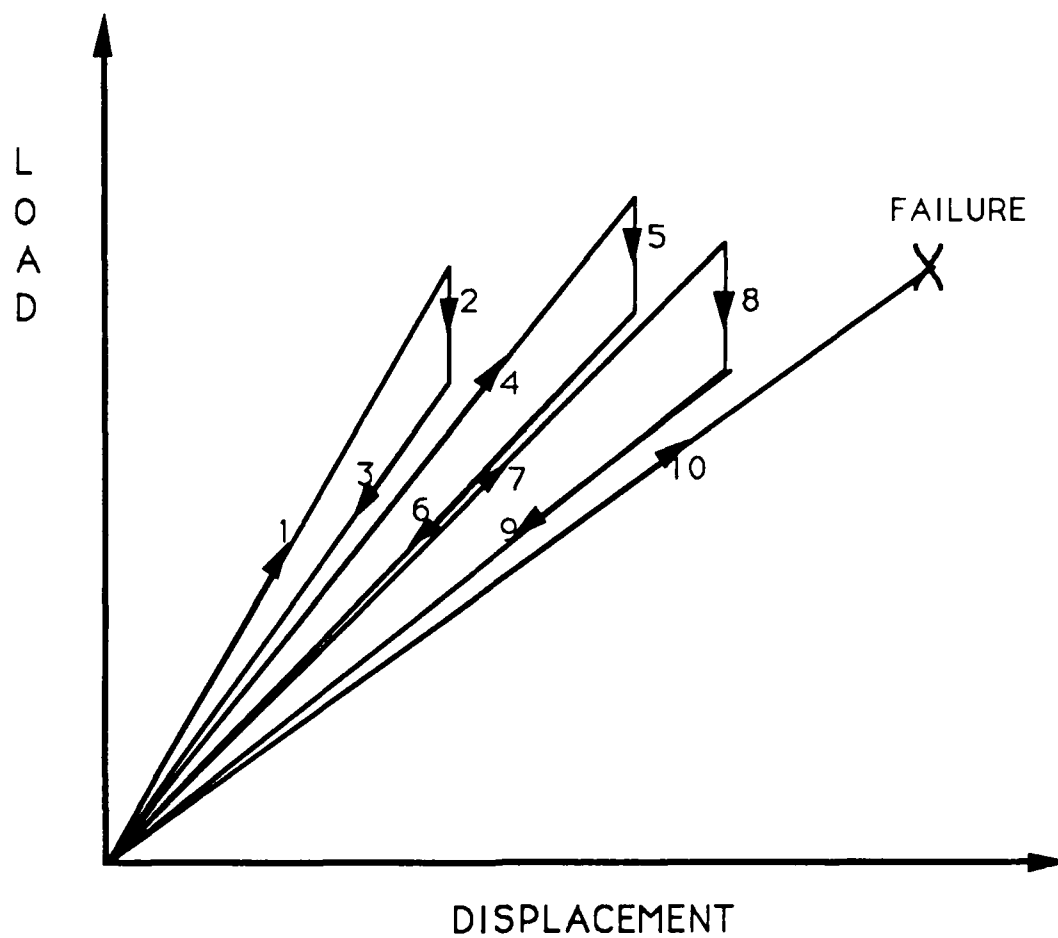


Figure 7: Schematic load-displacement trace  
of a CLS specimen



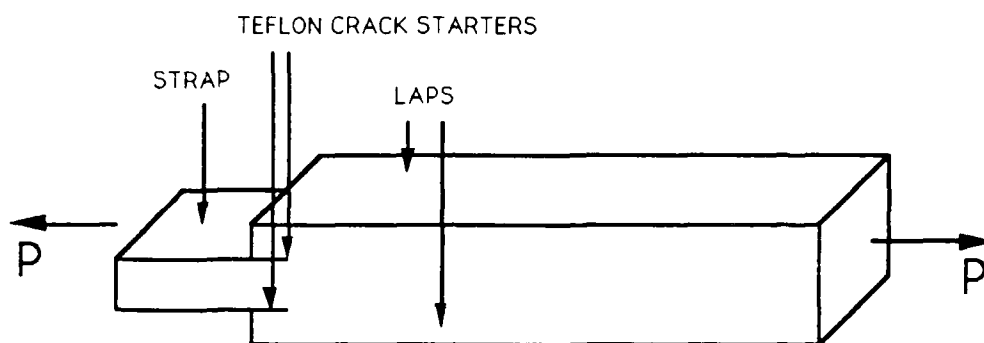
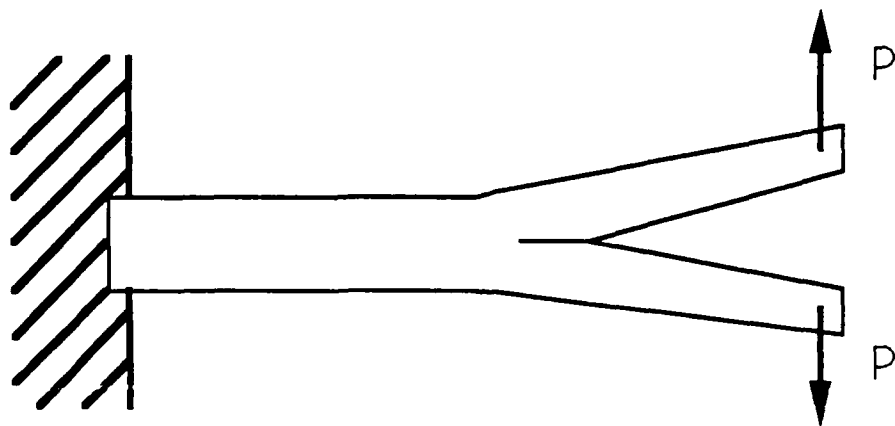
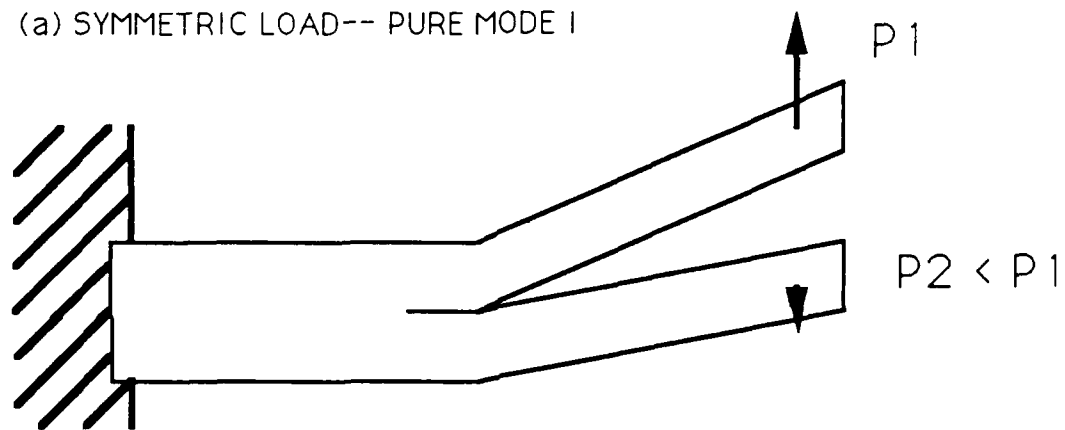


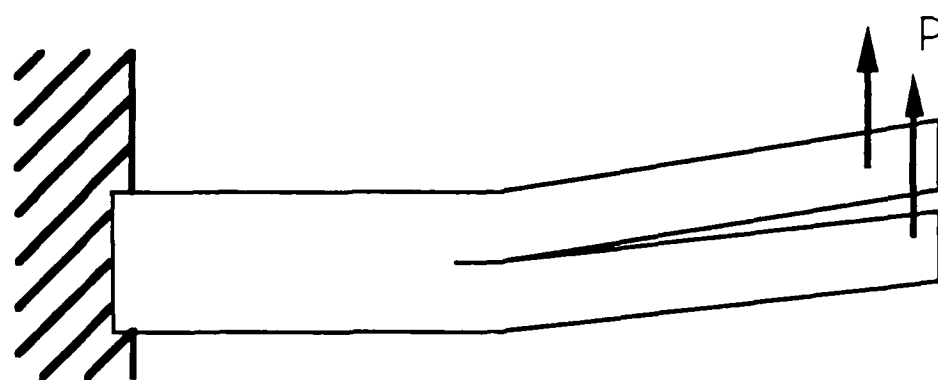
Figure 8: The double cracked lap shear specimen



(a) SYMMETRIC LOAD-- PURE MODE I



(b) NON-SYMMETRIC LOAD-- MIXED MODE I / MODE II



(c) NON-SYMMETRIC LOAD-- PURE MODE II

Figure 9: The double cantilever beam specimen

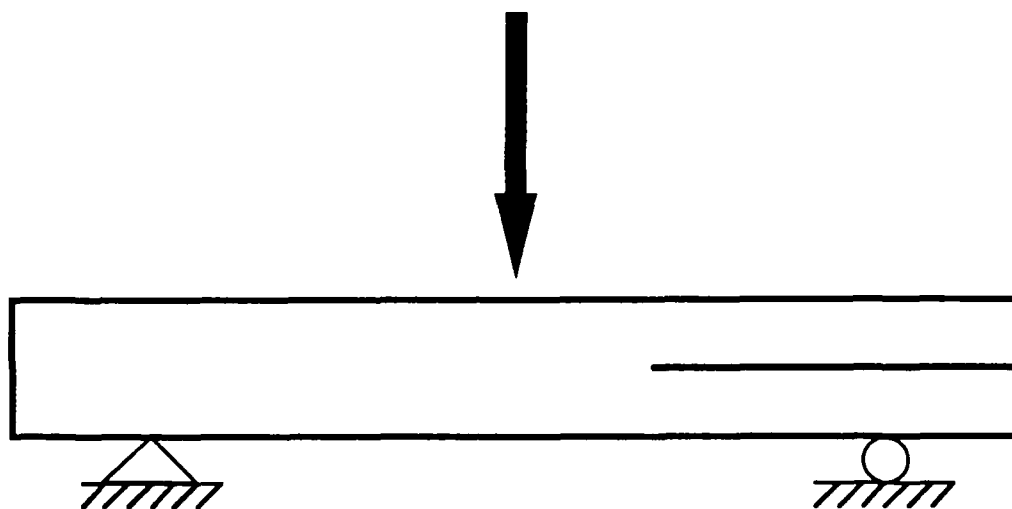


Figure 10: The end notched flexure specimen

varying the length  $c$  of the moment arm about the load nose of the loading lever. For example, when  $c = 0$ , pure mode II loading results. Reference 43 offers simple closed-form solutions for the mode I and mode II components of the loading, which can be substituted into the appropriate beam theories to provide strain energy release rate solutions.

One difficulty that arises during testing of unidirectional specimens is *fiber bridging*, which is said to occur when fibers are pulled out of the matrix and cross from one side of the delamination plane to the other. As noted by Johnson and Mangalgiri<sup>[44]</sup>, this increases the apparent delamination fracture toughness of a composite, because "bridged" fibers must be broken before failure can occur, whereas the peel stress  $\sigma_z$  usually bears only on the relatively weak matrix material. Fiber bridging leads to an unconservative estimate of delamination fracture toughness. Reference 44 concludes that fiber bridging may be reduced, if not necessarily eliminated, by slight cross-plying at the delamination interface, leading to reduced nesting of fibers between plies oriented in the same direction. However, even in the absence of fiber nesting, some bridging may occur, due to the effects of weak fiber-matrix interfaces, or of large crack tip yield zones.

When considering the behavior of a given composite configuration, it is important to consider the layup used, as the stacking sequence can have a profound effect upon failure. This has been demonstrated by Harris and Morris<sup>[45]</sup>, who found that the notched strength of T300/5208 laminated composites varied considerably with changes in stacking sequence. Reference 45 attributed this variation to changes in the fracture processes associated with each layup.

Two other areas of interest are the detectability of delamination and the interaction of delamination with other damage modes. Detectability is an important factor in product reliability, because if flaws cannot be detected well before they grow to critical size (that is, the size above which they will cause failure before the next inspection), a retirement-for-cause maintenance approach is impossible. Damage mode interaction can be used to make damage work in the favor of the

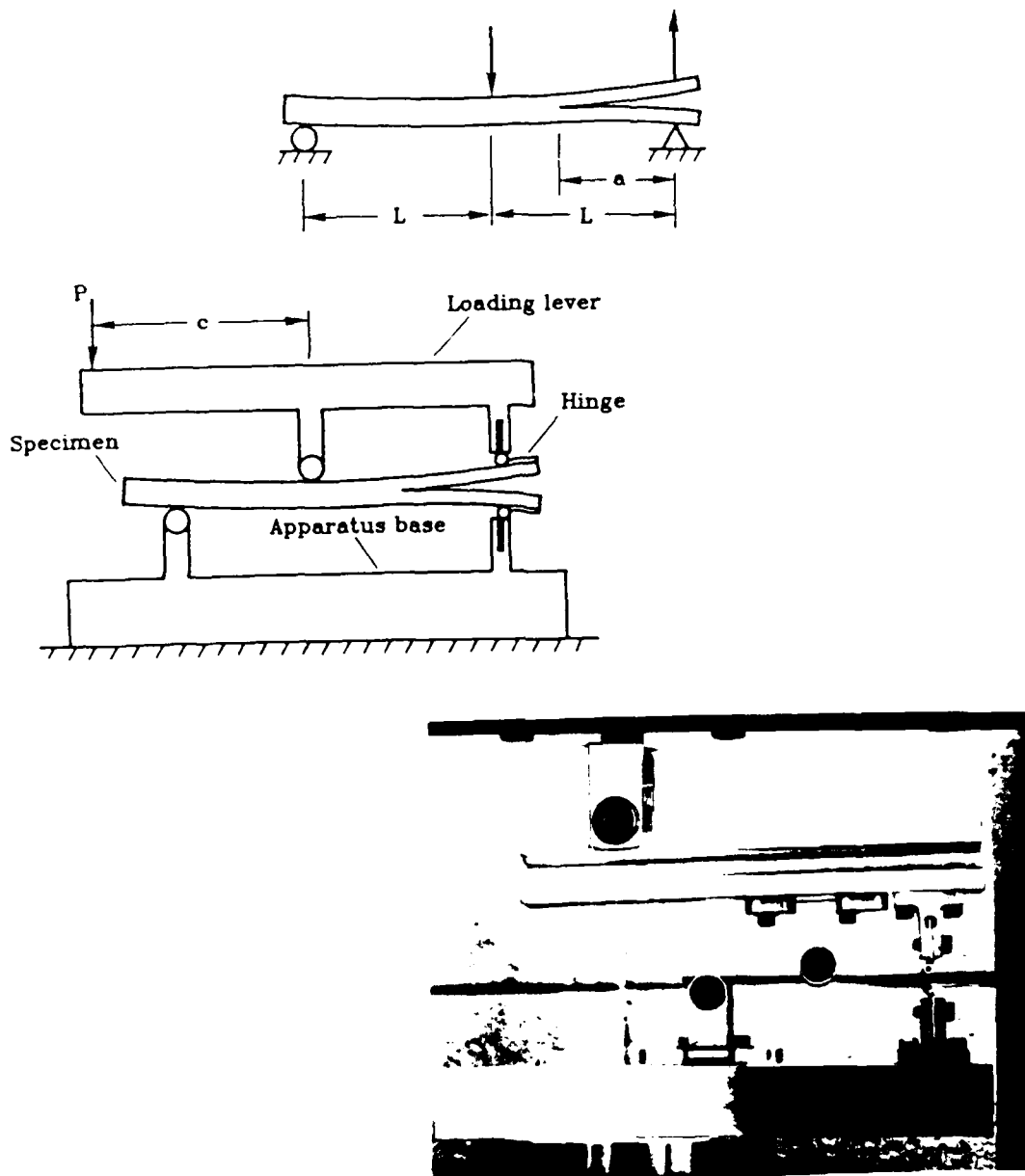


Figure 11: The Reeder-Crews specimen.<sup>[43]</sup> (a) test specimen and loading (b) schematic of apparatus (c) photograph of apparatus

designer, as has been shown in Reference 13. This reference identifies three damage modes present in a quasi-isotropic DCLS specimen: matrix microcracking, which is controlled by the resin strain to failure; delamination, which is controlled by the fracture toughness, and fiber breakage, which is controlled by the fiber strength. Generally, it is the first two modes that are evident in crack propagation, with fiber breakage occurring, if at all, during the final failure phase. It was found that matrix microcracking can work to reduce the Mode I component of delamination, significantly increasing the resistance to crack growth of the material. Thus, further investigation of interaction phenomena is in order.

## **2.6 SUMMARY**

This chapter has surveyed the means of analyzing composite failure from the standpoint of mechanical analysis and from that of materials science. It is seen that the problem of delamination and its interaction with other damage modes cannot be modelled by a classical theory. Furthermore, the critical events in delamination occur in a volume so small as to require that numerical models be extremely large. Sublaminar analysis offers a viable alternative combining the best combination of accuracy and simplicity, but even this approach requires an in-depth understanding of laminate behavior.

Examining fracture of the three-point bend specimen in particular, it is seen that the validity of the test is in doubt. Several analyses have demonstrated that the failure mode of these specimens is not as assumed. It remains to be seen if the three-point bend test is of any use, and if not, how the specimen actually fails.

A review of the literature in polymer science reveals that study of polymer fracture surfaces lead to knowledge of the circumstances that produced the fracture. Information on factors such as the degree of brittle fracture, the presence or absence of crazing, the significance of fiber breakage, and the relative importance of shear and normal stresses can be gained from the fracture surface.

A brief survey of composite fracture specimen types is offered. A correlation between fracture surface morphology and observed test configuration behavior is needed. In particular, the damage mechanisms underlying the arrest phenomenon in the CLS specimen must be better understood.

**CHAPTER III:**  
**FRACTURE BEHAVIOR**  
**OF THE SHORT-BEAM COMPOSITE SPECIMEN**

**3.1. Introduction**

Composite materials have complex failure modes that include delamination, fiber debonding and breakage, and matrix microcracking. In this chapter, the influence of these damage modes on the failure of the short-beam three-point bend test is investigated for a composite with a quasi-isotropic layup. It is found that failure initiates in a region near the point of application of the load, a location where classical type analytical descriptions of specimen behavior are unreliable. Furthermore, the locations of delamination show little reproducibility. Observed fracture behavior is explained in terms of the overall stress state in the beam prior to fracture, and failure is predicted from the stress map, using the maximum strain criterion.

**3.2. Background: The Three-Point Bend Test**

The three-point short-beam bending test, as shown in Figure 3, has long been



used to quantify the shear strength of laminated composite materials. In this test, a small composite beam of rectangular cross-section is cut from a plate with a diamond cutoff wheel, inspected for flaws, and loaded in displacement control at a crosshead speed of 0.05 inches per minute. The interlaminar shear stress at failure is then calculated using the equation

$$\tau_I = \frac{3P}{4A} \quad [1]$$

where

$\tau_I$  is the interlaminar shear stress

$P$  is the applied load at failure

$A$  is the cross-sectional area of the specimen

Since it is based upon a simple strength of materials analysis, this equation neglects the effects of stress concentrations and anisotropy.

This test is frequently used to screen materials based on their interlaminar shear strength. However, there is concern that use of the test relies upon incorrect assumptions concerning the nature of the failure process. Equation [1] is based on a parabolic through-the-thickness shear stress distribution with a maximum at the beam midplane. While this is correct for an isotropic material, it is misleading for a composite beam. Whitney and Browning, in Reference 24, examining the failure of of unidirectional short-beam specimens, discovered that pure Mode II failure along the specimen midplane was not the mode of fracture. Rather, compressive stresses in the regions of high interlaminar shear stress were found to suppress interlaminar-shear failure modes, and initial damage due to vertical cracking was found to precede final failure due to large scale delamination. If the failure process is this complex, then the applied load at failure does not depend solely on the interlaminar shear strength, making the test useless for its intended purpose.

Because of this uncertainty, there is a need for reexamination of the short-beam

three-point bend specimen for specific composite configurations. Such an examination must determine whether a simple relationship between loading and fracture exists, and, if not, what fracture processes are taking place. The current effort answers these questions for a laminate with a resin matrix and a quasi-isotropic layup.

### 3.3. General Failure Analysis

#### 3.3.1. Specimen Design and Testing

The subject of the investigation was a short-beam specimen with dimensions given in Table 1. A sample panel was fabricated by the Lockheed-Georgia Company and inspected for quality, using standard aerospace industry practice, before sectioning into specimens. Two fiberglass plies, each of thickness 0.018 inches, were bonded to the upper and lower surfaces, in order to minimize the bearing effect at the supports and the applied load location.

The material properties for the graphite/epoxy and for the fiberglass plies are given in Table 2. The material was an AS4/3502 graphite/epoxy system, and the layup was  $[\mp 45/0/90]_{6s}$ . The subscript denotes that an eight-ply unit, of layup  $[\mp 45/0/90/90/0/\pm 45]$ , is repeated six times. This layup meets the definition of quasi-isotropy:

$$A_{11} = A_{22} \quad [2]$$

$$A_{16} = A_{26} = 0 \quad [3]$$

$$A_{66} = \frac{1}{2} [A_{11} - A_{12}] \quad [4]$$

TABLE 1: DIMENSIONS OF  
QUASI-ISOTROPIC SHORT-BEAM  
SPECIMEN, INCHES  
(see figure 3 for nomenclature)

$L$	1.00
$c$	0.625
$t_{tab}$	0.018
$t_{total}$	0.283
$B$	0.375

where  $A_{ij}$  are extensional stiffnesses. Equations [2], [3] and [4] indicate that the properties of the material are approximately isotropic in the  $x - y$  plane.

Four specimens were tested to failure in three-point bending, with failure loads as given in Table 3. The shear strength predictions in the table are based on Equation [1]. The failed specimens were sectioned with a silicon carbide saw of blade width 0.015 inches, and the sections were mounted upon scanning electron microscope (SEM) stubs with silver paint. After coating by a gold-palladium sputter coater, the sections were examined under the SEM, to investigate fractographic characteristics and their relationship with the prevalent damage modes. This provided information on all of the phenomena contributing to final specimen failure.

### **3.3.2. Numerical Methods**

Numerical analysis of the specimen concentrated on the phenomenon of delamination. Delamination analysis can be based on two approaches: the strain energy release rate approach and the interlaminar stress approach. The interlaminar stresses are due to Poisson's ratio mismatch and to differences in the coefficients of thermal and moisture expansion between plies. Delamination occurs when these stresses reach the interlaminar strength of the material. The strain energy release rate approach is based on the actual process of fracture, rather than the strength concept. Delamination can propagate when the strain energy release rate at the crack front is sufficient to overcome the material's fracture resistance or toughness.

Finite Element Method (FEM) analysis of the specimen was performed using two codes: Engineering Analysis Language (EAL), a linear code, and Geometrically and Materially Nonlinear Analysis of Structures (GAMNAS), a NASA-developed code described in Reference 22. Both codes were run using meshes consisting entirely of four-noded, rectangular elements, using a two-dimensional plane stress model. Both meshes considered one ply to be one element thick. The EAL mesh

**TABLE 2: PHYSICAL PROPERTIES OF  
SPECIMEN CONSTITUENT MATERIALS**

CONSTANT	AS4/3502	FIBERGLASS
$E_{11}$	20.5 Msi	3.19 Msi
$E_{22} = E_{33}$	1.67 Msi	3.19 Msi
$G_{12} = G_{13}$	0.87 Msi	0.57 Msi
$G_{23}$	0.5 Msi	0.43 Msi
$\nu_{12} = \nu_{13}$	0.26	0.11
$\nu_{23}$	0.43	0.42

**TABLE 3: FAILURE LOADS OF  
QUASI-ISOTROPIC SHORT-BEAM  
SPECIMENS, LBS**

TEST #	LOAD	SHEAR STRENGTH, PSI
1	1,025	6,830
2	1,120	8,096
3	1,055	6,753
4	1,325	7,700

employed elements of aspect ratio 5:1, except within five ply thicknesses of the load nose and support, where the ratio was 1:1. These ratios were not the same in the fiberglass plies, which were also one element thick but had a greater real thickness than the other plies. The EAL mesh modelled only one half of the specimen, taking advantage of the symmetry of the problem about the loading axis. Figure 12 shows the mesh used for the EAL model. The number of elements is 1,900, and the total number of degrees of freedom is 3,940. The heavy vertical line in the figure corresponds to an assumed crack.

Subsequent EAL models involving assumed cracks in the specimen near the free end also had mesh refinement to an aspect ratio of 1:1 in the vicinity of the crack tip. These models were used to find the strain energy release rates associated with the assumed cracks, using the zero-length element method illustrated in Figure 13. A one-dimensional element of finite stiffness and zero initial length is used to connect two nodes near the crack tip. When a load is applied, the zero-length element experiences forces  $F_1$  and  $F_2$  in the  $x$ - and  $z$ -directions, respectively. At the same time, the nodes connected by this element are separated by deflections  $\delta_1$  and  $\delta_2$ . Assuming that elements in the region of the crack tip have an aspect ratio of 1:1, the strain energy release rates  $G_i$  in each mode are given by<sup>[46]</sup>

$$G_i = \frac{1}{2} \left( \frac{F_i \delta_i}{B \times \Delta a} \right) \quad i=1,2 \quad [5]$$

where  $B$  is the specimen width, as shown in Figure 3, and  $\Delta a$  is the length of one side of an element. In this case,  $G_1$  and  $G_2$  correspond to Mode II and Mode I fracture, respectively. Mode III cracking is negligible for this specimen design.

The GAMNAS model did not employ a symmetry plane, and all elements were of approximate aspect ratio 4:1, except for elements in the fiberglass plies, which were of approximate aspect ratio 1.2:1. Figure 14 shows the mesh for the GAMNAS model. There are 2,600 elements and 5,404 degrees of freedom in this mesh. The mesh is coarse in comparison with the EAL discretization, since the element is based

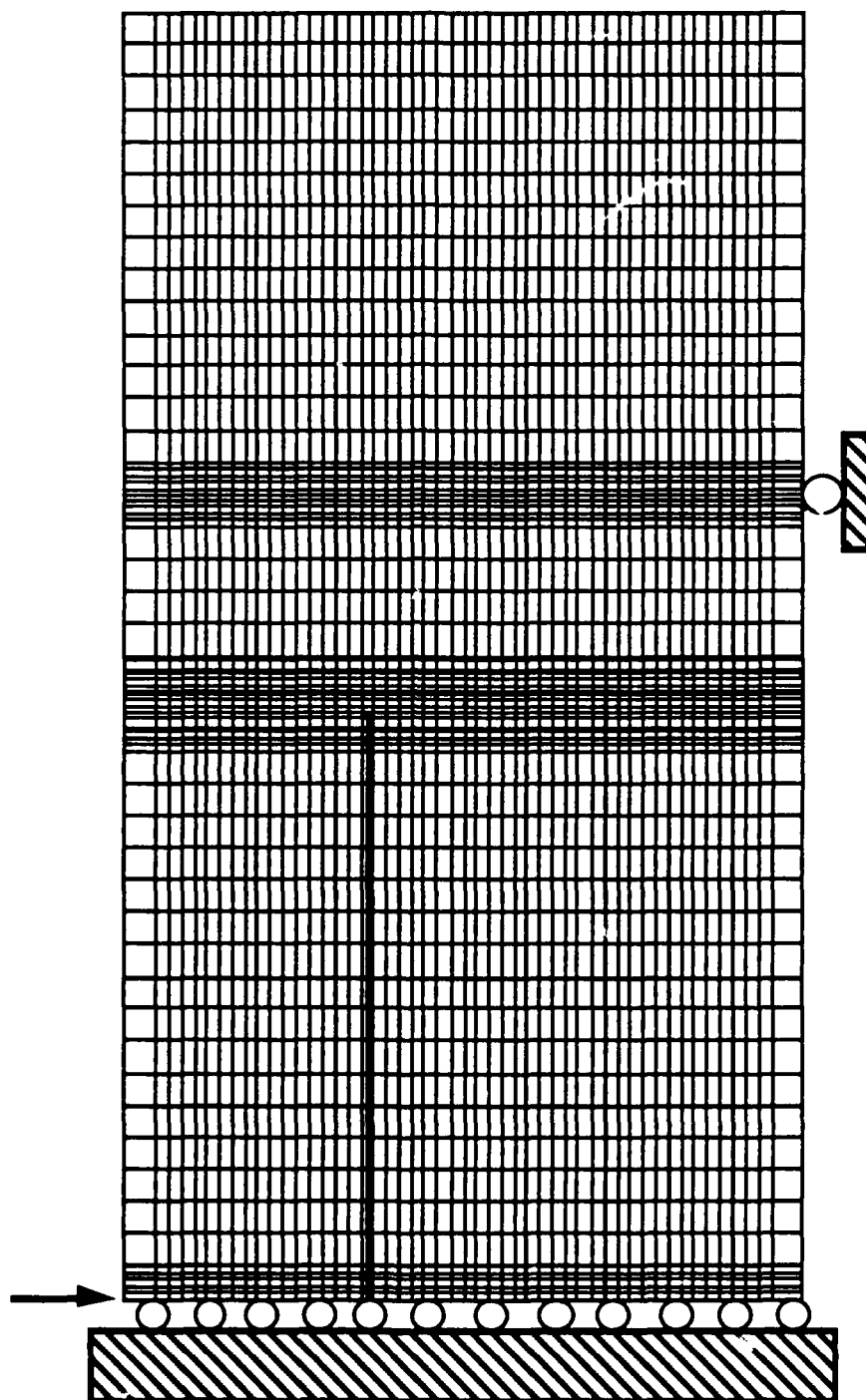


Figure 12: Schematic of the EAL mesh



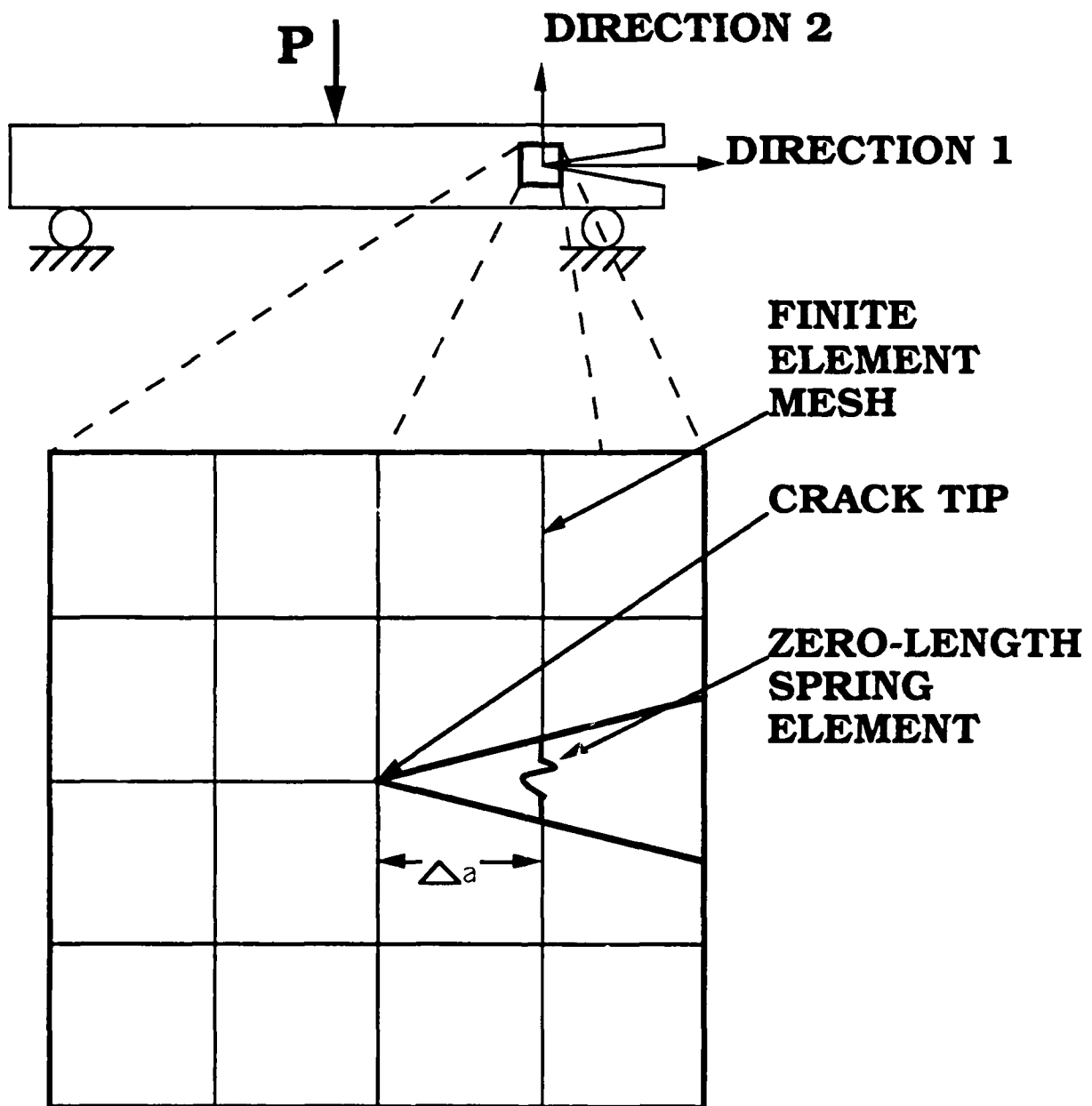


Figure 13: The zero-length element

upon a nonlinear formulation.

The GAMNAS model was used to predict the stress field in the specimen, using an assumption of geometric nonlinearity. The EAL model was used to predict the strain energy release rate using the zero-length element, as well as the stress field. Comparison of the stress field results from the two codes showed geometric nonlinearity effects to be negligible. This supports the use of the linear EAL model, which was much simpler to use for a large number of similar but non-identical configurations.

### **3.3.3. Results of Numerical Analysis**

#### **3.3.3.1. Stress Maps**

Table 4 shows the locations of delamination failure observed for a representative group of samples. Figure 15 shows the ply and interface numbering scheme. The table lists, for each interface, the number of specimens where final failure was observed for that interface. Since the layup includes 50 plies, there are 49 interfaces, of which interface 25 is the midplane. It is seen that the failures took place well away from the midplane. Note the large amount of variation in the locations of delamination. No single interface accounts for even a majority of the observed failures. This would not be the case if fracture was driven by a simple mechanical process. In other materials, such variation in fracture behavior might be attributed to the random distribution of material defects. Several types of processing defects, such as voids, resin-rich areas, and bridged fibers, can affect fracture behavior. However, such defects usually do not drive fracture behavior to the extent found in Table 4. It should also be noted that several specimens showed additional, secondary cracking above the midplane, indicating a complex failure process. It was observed that the delaminations did not extend for the full length of the specimen. Finally, it should

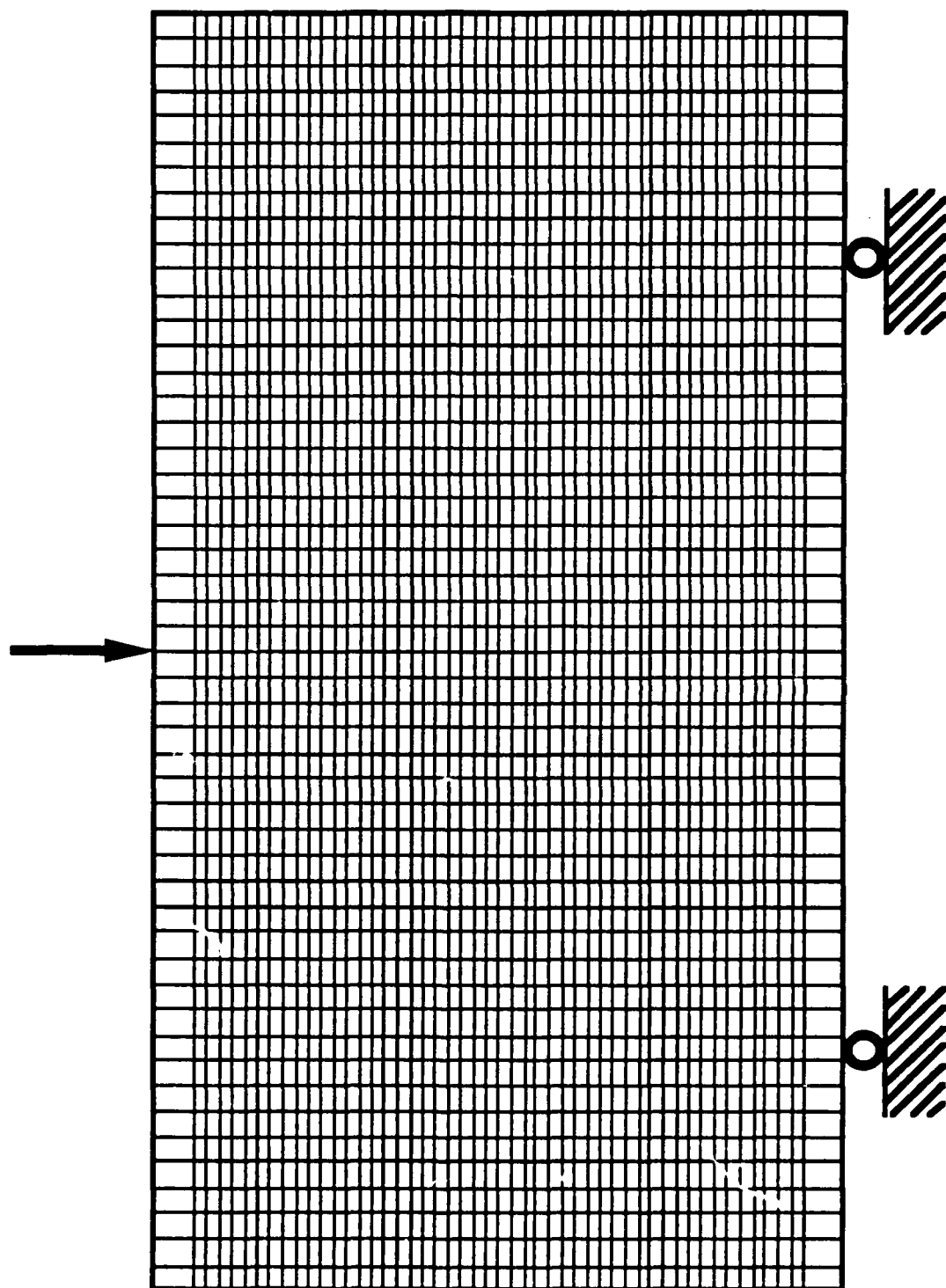


Figure 14: Schematic of mesh for the GAMNAS model

be noted that all of the specimens in which one primary delamination appeared to the naked eye had that single delamination below the midplane.

Figure 16 shows actual failed specimens, illustrating the variability in crack location.

GAMNAS analysis yielded stress profiles for the specimen under load, which are shown as Figures 17, 18, and 19. On the basis of the data shown in Table 3, a load of 1000 pounds was selected for these calculations. These figures show one half of the  $y$ - $z$  plane. The coordinate system can be understood in terms of Figure 3, which also shows the  $y$ - $z$  plane. The origin of the coordinate system is at the midplane, directly beneath the load nose. Thus, the load is applied at the point  $(0, t_{total}/2)$ , and the supports are located at the points  $(\pm c, -t_{total}/2)$ . A direction normal to the  $y$ - $z$  plane is used for the stress values.

Figure 17 maps the peel stress  $\sigma_{xz}$ . The figure shows high values of compressive stress near the load nose and the support, and relatively small values of peel stress elsewhere, suggesting that mode I cracking is limited in this specimen

Figure 18 maps the chordwise stress  $\sigma_{yy}$ . This figure is much as would be expected, with a typical bending-stress profile and the largest magnitudes near the load nose. As a check for reasonableness, a two-dimensional plot of  $\sigma_{yy}$  appears on the back wall of Figure 18. These values are taken at  $y = 0.3125$  inches, a location well-removed from the stress concentrations at the load nose and support, and are shown as the light line on the back-wall plot. The heavy line graphs the  $\sigma_{yy}$ -values predicted from isotropic beam theory for an homogeneous beam with smeared properties. This simple model well represents the magnitude and trend of the finite element data, as it should.

The map of the shear stress  $\sigma_{xz}$ , shown in Figure 19, is the most significant. Major deviations from the parabolic stress profile expected from beam theory are seen. High values of shear stress are found near the load nose and support. The maximum stress values between the load nose and support are consistent with the predictions of beam theory. This is shown by a back-wall plot similar to that of

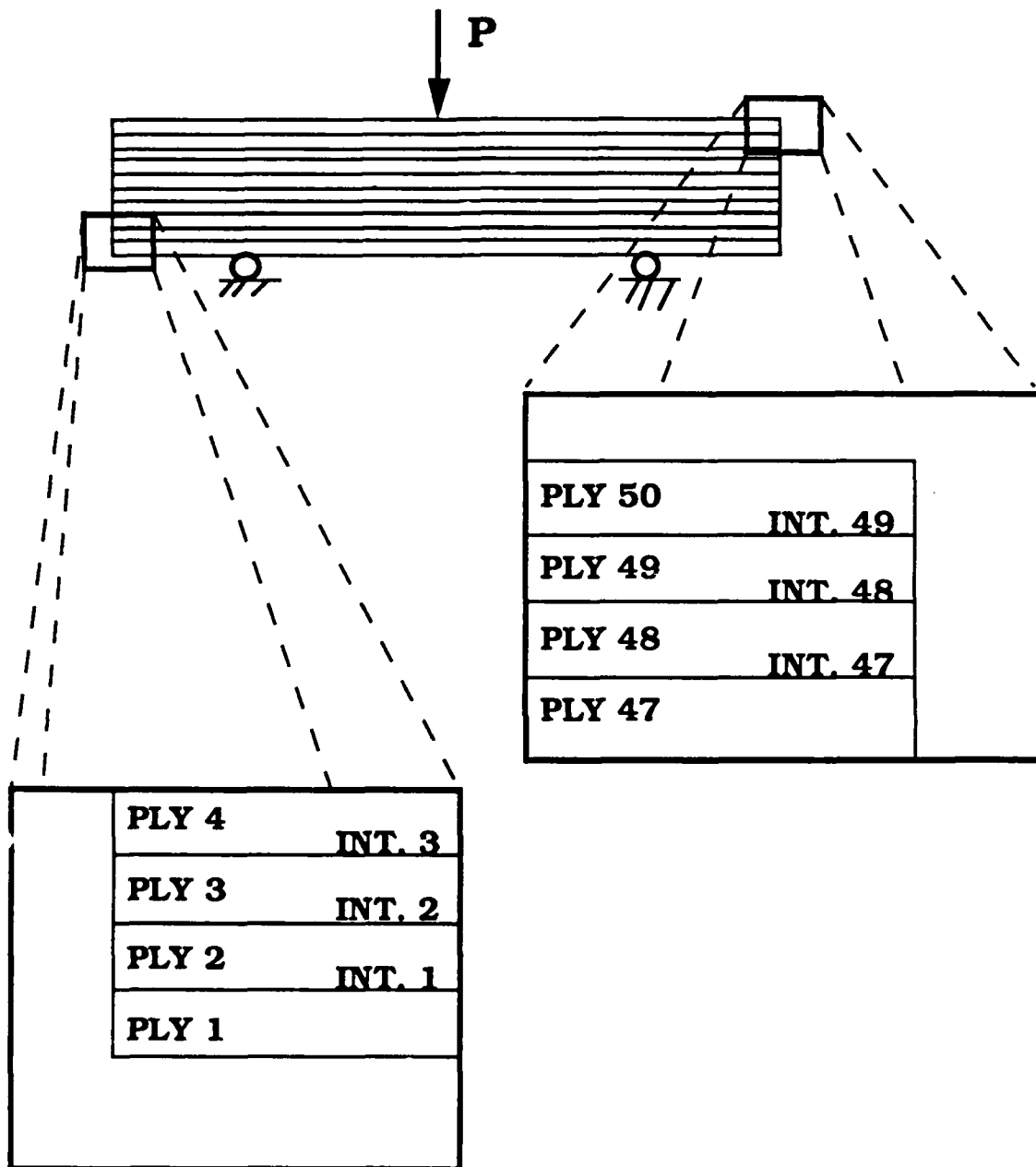


Figure 15: Ply and interface numbering

**TABLE 4: LOCATIONS OF FAILURE OF  
SHORT-BEAM SPECIMENS**

LOCATION, INTERFACE #	NUMBER OF FAILURES
14	5
11	2
7	2
6	2
12	1



Figure 16: Failed short beam specimens

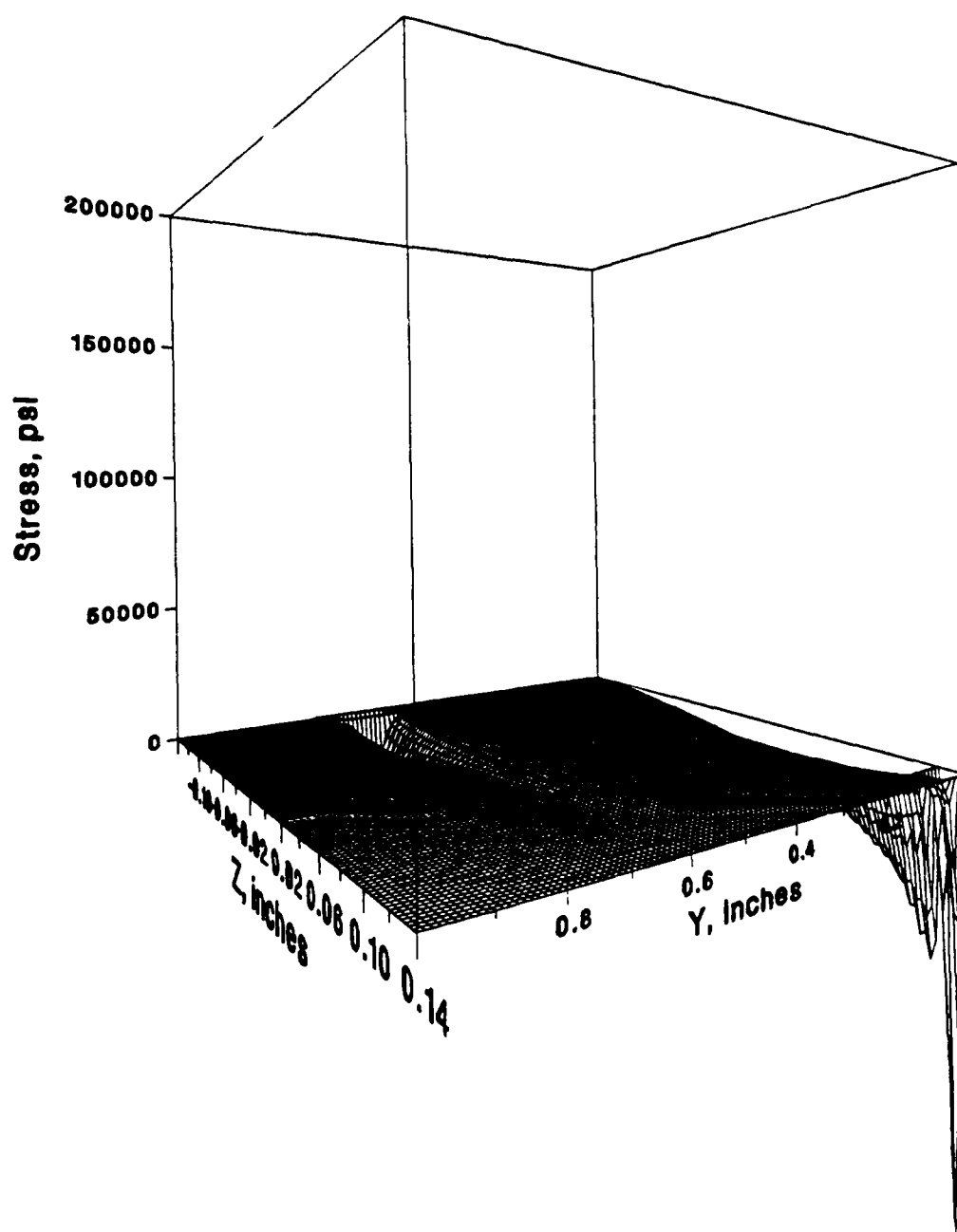


Figure 17: Map of Peel Stress



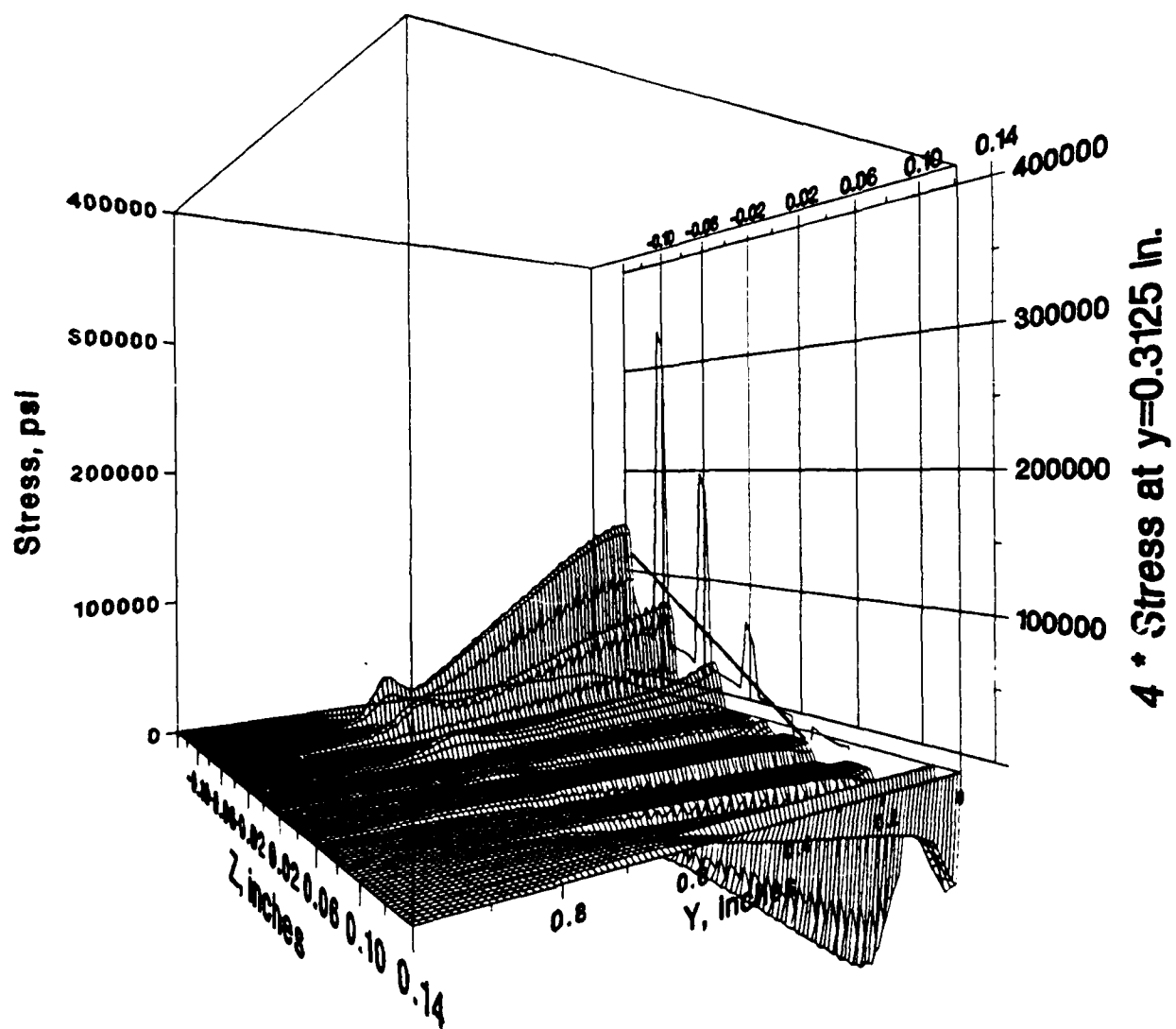


Figure 18: Map of Chordwise Stress

Figure 18.

In summary, the beam-theory analysis used to derive equation [1] significantly underestimates the magnitude of the stress beneath the load nose and near the support, while adequately predicting it elsewhere.

### 3.3.3.2. Failure Predictions

Figures 17, 18, and 19 indicate that it is unlikely that damage initiates at the specimen free ends, which are, as would be expected, nearly stress free. To confirm this, failure of the specimen was analyzed, using the maximum-strain criterion. Stress data from each element in the GAMNAS model were converted to strain data, and these strains were compared to the material strain to failure. The fraction of the critical strain in the fiber, matrix, and shear orientations was calculated, and the largest of these was selected, with the assigned data values capped at 100 % of strain to failure. The resulting data provide a map of nearness to failure at each location in the specimen, and are shown in Figure 20. The load used for this figure is 1200 pounds. This is similar to the actual failure loads.

Figures 21, 22, and 23 show nearness to failure maps for the three stress components: chordwise, peel, and shear. Considered along with Figure 20, they offer insights into the possible causes of failure at various locations. For example, Figure 20 shows that failure is imminent in the region near the load nose; reference to Figures 21, 22, and 23 shows that this is due to crushing. Failure due to crushing is also incipient near the support, and failure due to chordwise stresses below the midplane near the load nose is also a possibility. In contrast, the midplane, where beam theory predicts the largest shear stresses, is the region least vulnerable to failure. This is consistent with the observed cracks in the tested specimens, which failed below the midplane and sometimes above it, but never on or near the midplane.

The maximum strain to failure map of Figure 20 was modified to include additional failure modes observed by McCleskey<sup>[47]</sup> in his studies of glass-epoxy lam-

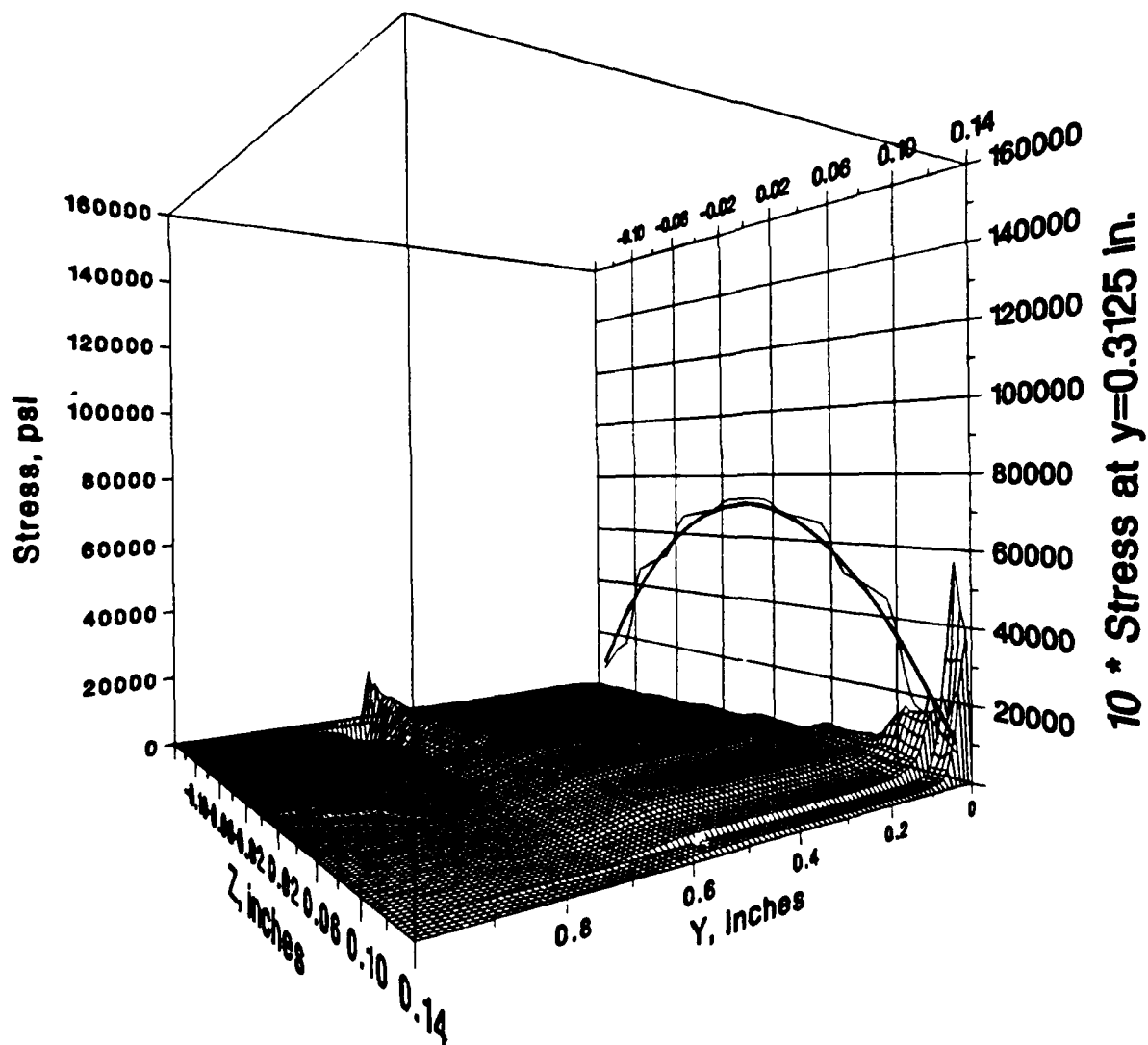


Figure 19: Map of Shear Stress

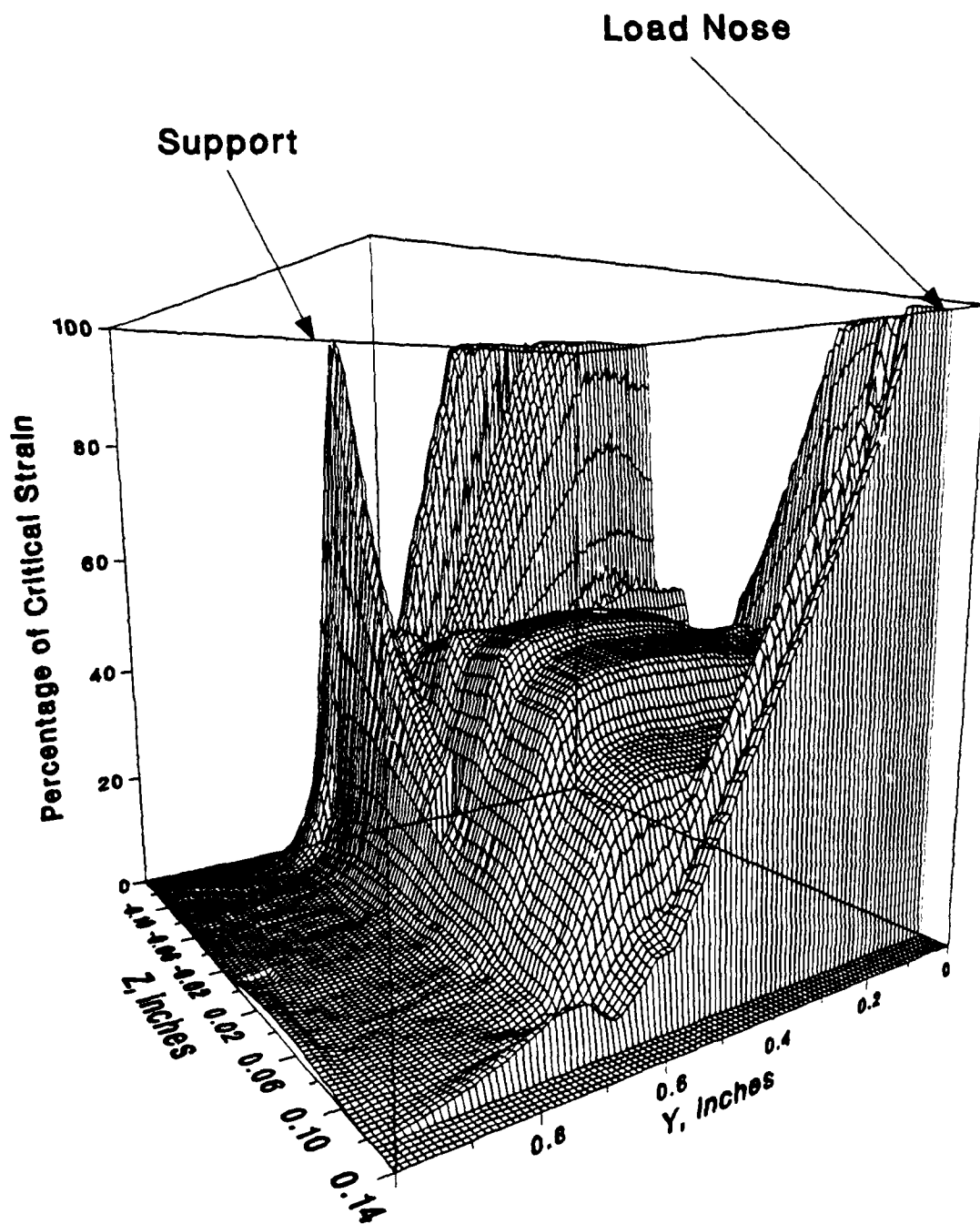


Figure 20: Map of maximum fraction of critical strain

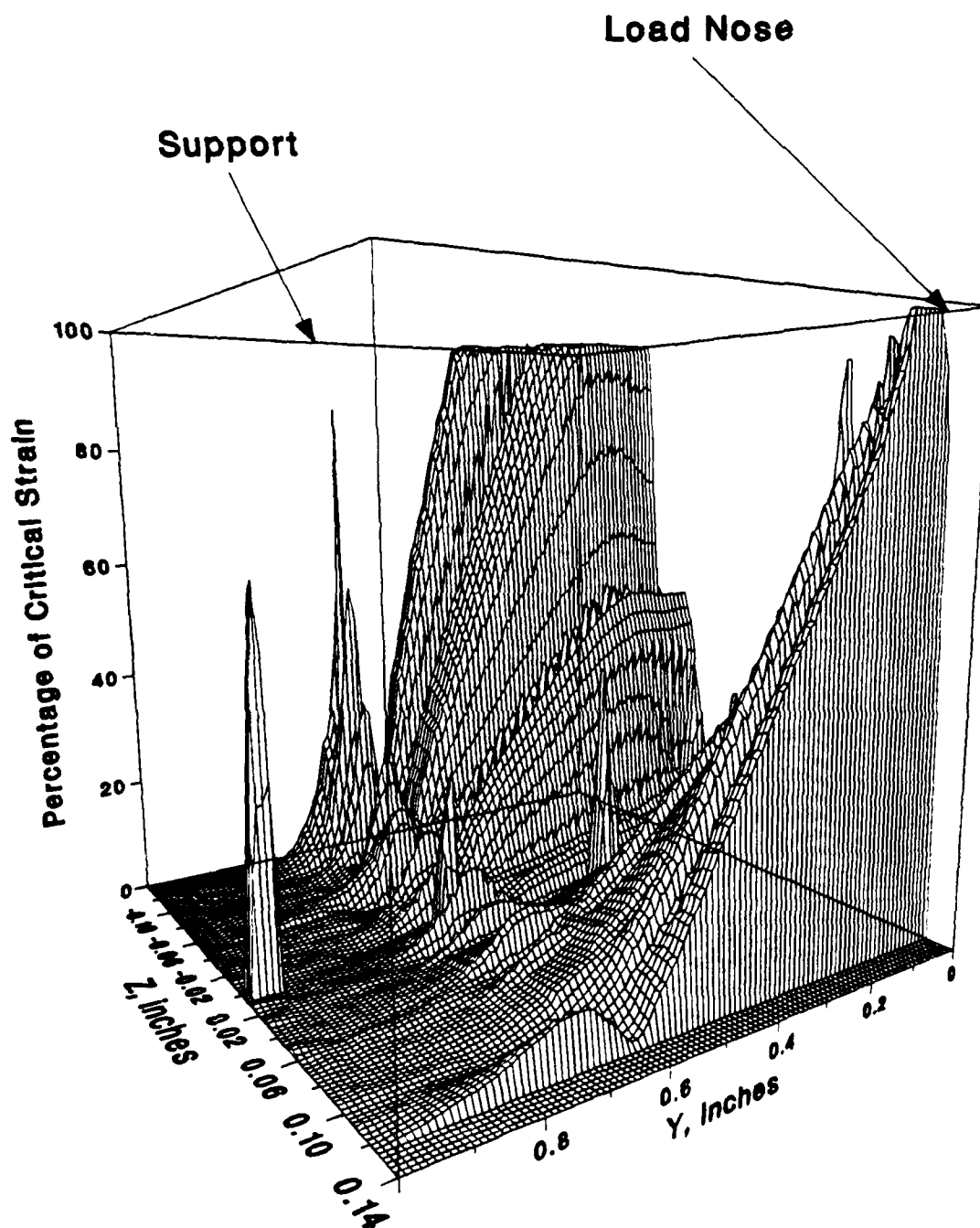


Figure 21: Map of fraction of critical strain due to chordwise stresses

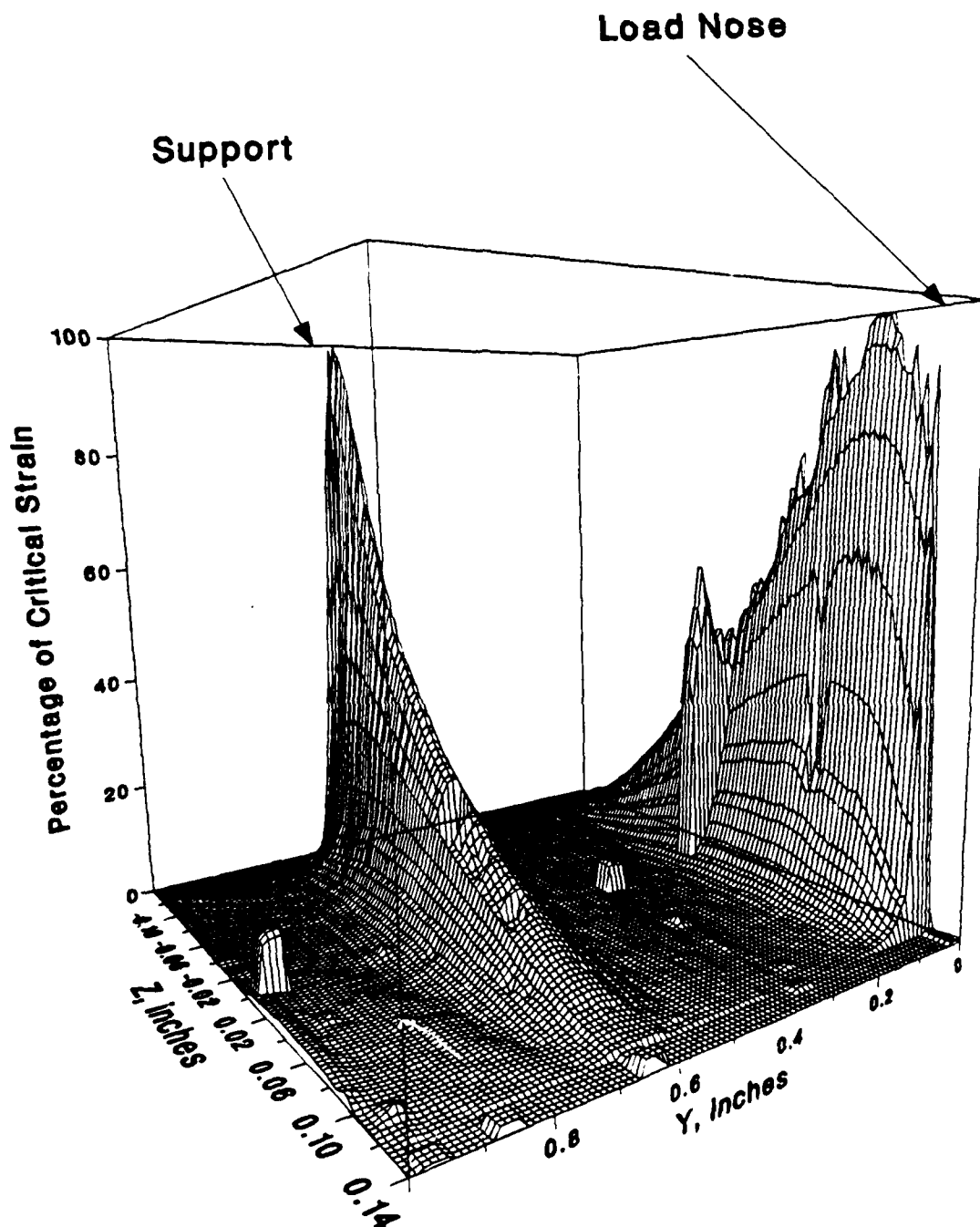


Figure 22: Map of fraction of critical strain due to peel stresses

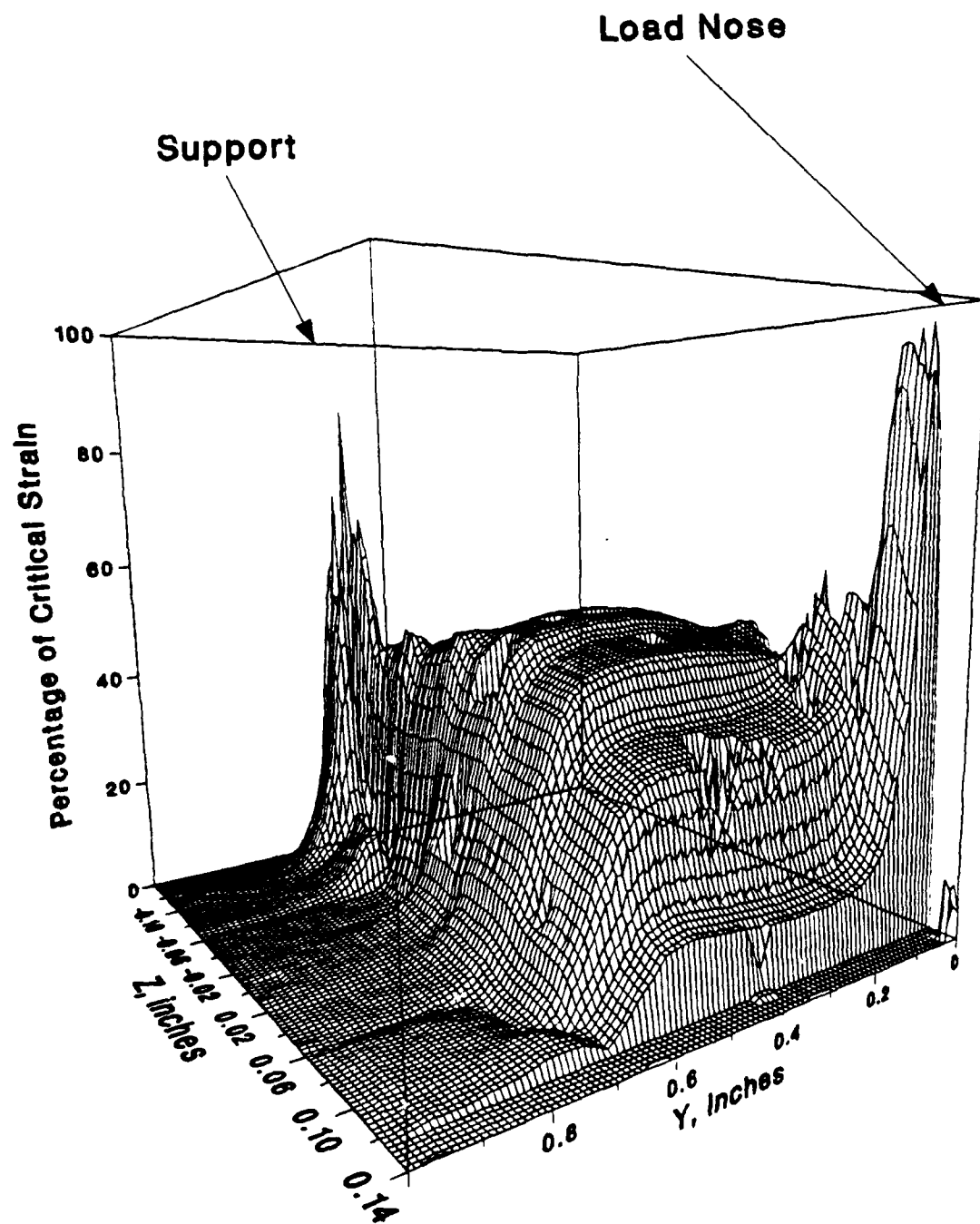


Figure 23: Map of fraction of critical strain due to shear stresses

inates. McCleskey's laminates consisted of eight plies, each of thickness 0.0325 inches, and were of layup  $[90/-45/45/0]_s$ . When these specimens were tested in three-point bending, a zero-degree ply near the midplane was observed to crack at an angle of 45 degrees to the midplane, as shown in Figure 24. McCleskey suggested that these failures were due to the state of nearly pure shear near the specimen midplane resolving itself into a tensile stress at a 45-degree angle to the midplane. This stress would act upon the matrix of a zero-degree ply.

This effect could be modelled as shown in Figure 25. It is assumed that any normal stress in the  $y - z$  plane leads to matrix-driven failure in a zero-degree ply. Thus, in order to determine the maximum effect of normal stresses upon such a ply, it is necessary to determine the largest normal stress operating in the  $y - z$  plane; if  $\sigma_{xx}$  is assumed to be zero, then this largest normal stress is the principal stress with the largest magnitude. The percentage of strain to failure can then be calculated using this largest principal stress and the appropriate tensile or compressive modulus for loads applied normal to the fibers.

A similar phenomenon might take place in the 45-degree plies, leading to a failure surface as shown in Figure 26. To predict this second additional failure mode, it would be necessary to determine the traction normal to the fracture surface shown in this figure, and therefore to perform a three-dimensional stress transformation, assuming the out-of plane stresses to be zero. The percentage of strain to failure for this fracture mode could then be calculated using the traction resolved on this face, and the appropriate tensile or compressive modulus for loads applied normal to the fibers.

The analysis that produced Figure 20 was modified to include the two additional failure modes and was repeated, with results as shown in Figure 27, 28, and 29. The areas where Figures 20 and 27 differ are, therefore, areas where one of the McCleskey failure modes determines fracture. Comparison of figures 20 and 27 shows one change due to these new modes of failure: some interior plies become much more highly strained in the region between the load nose and the support.



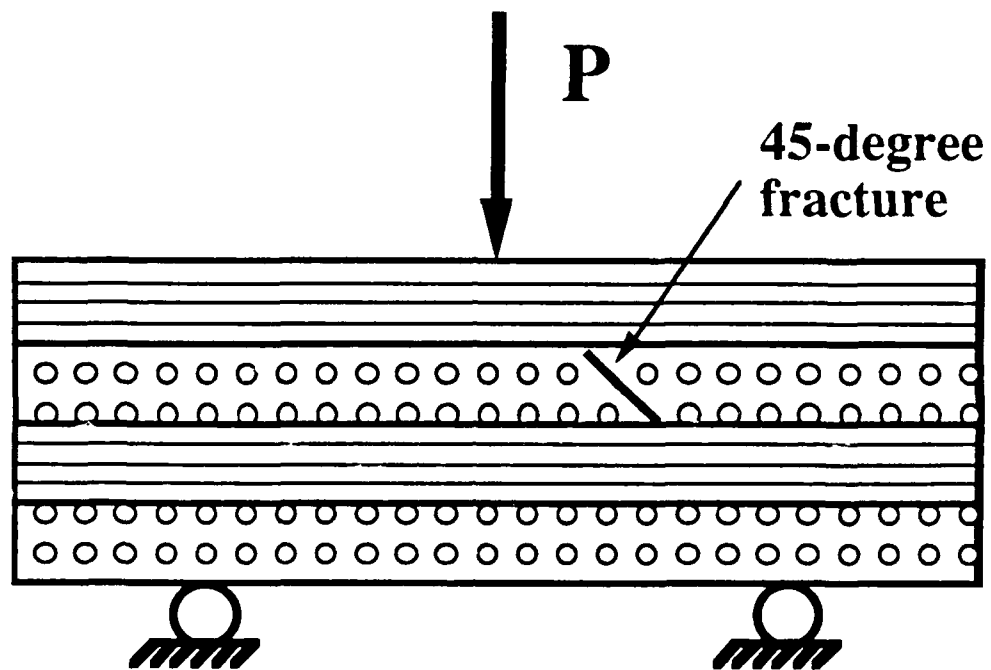


Figure 24: First McCleskey failure mode

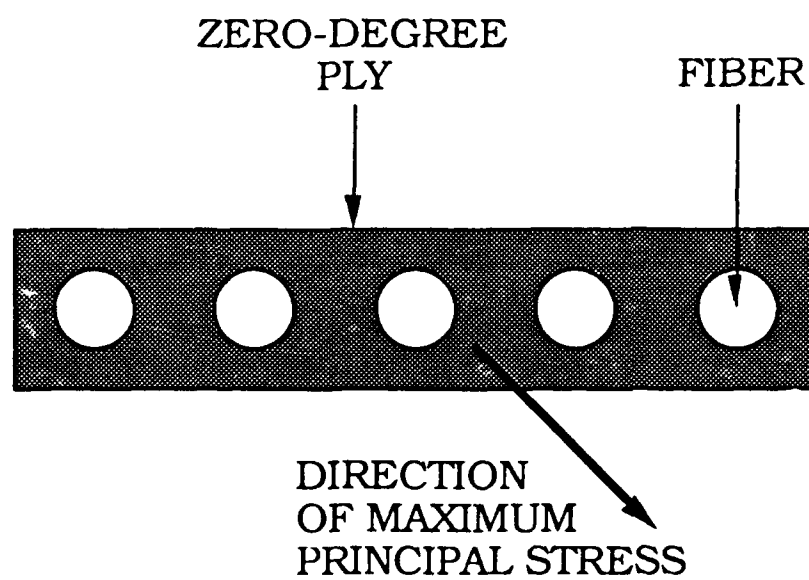


Figure 25: Modelling of first McCleskey failure mode

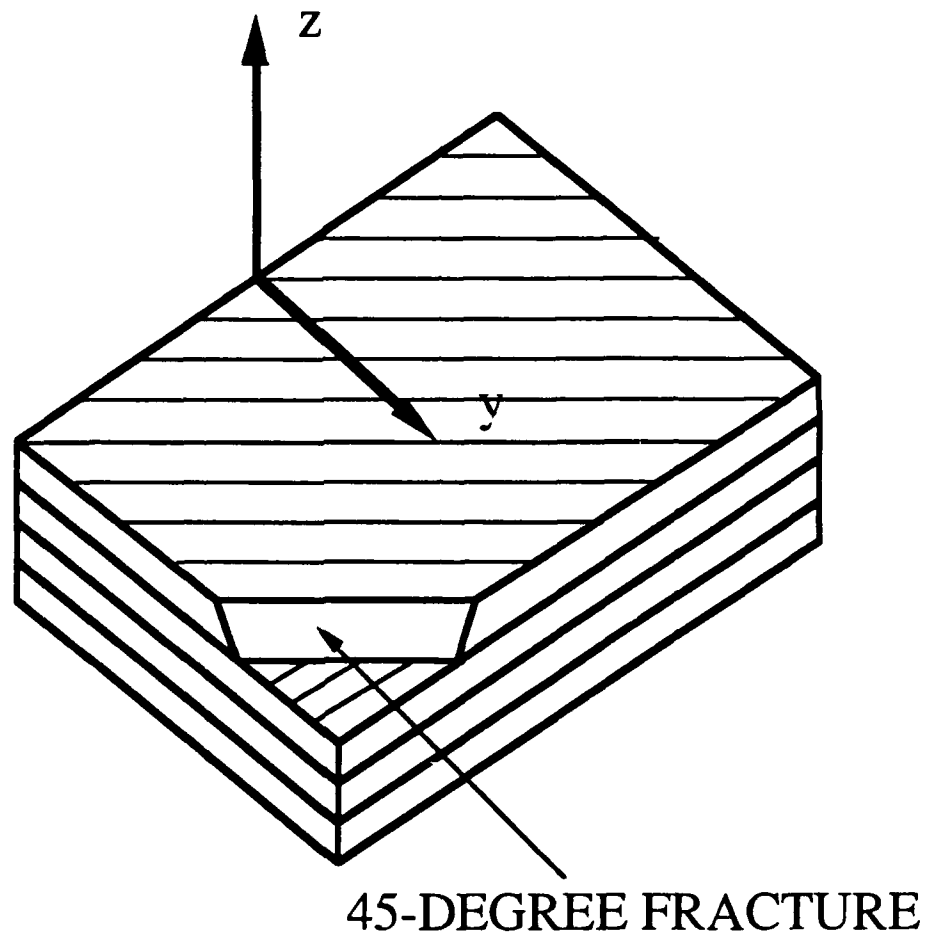


Figure 26: The second McCleskey failure mode

These are zero-degree plies, with the new failure mode being the one shown in Figure 25. Figures 28 and 29 show the contributions of the two individual McCleskey failure modes.

It is worth noting that the increase in percentage of critical strain is not symmetric about the midplane. This is because the chordwise stress component affects the principal stress component that drives the failure mode shown in Figure 24. Large tensile chordwise stresses, found below the midplane, increase the principal stress value and thus the maximum percentage of critical strain. Additionally, the principal axes are redirected as the chordwise stress becomes large; plies exhibiting this failure mode well below the midplane would not crack at the 45-degree angle shown in Figure 24.

In summary, Figure 27 includes the two failure modes observed by McCleskey. By comparison with Figure 20, the map of Figure 27 shows a significantly increased nearness to failure in the interior of this specimen. While there is not enough of an increase to make this a principal initial failure location, the possibility of cracking in the interior of the specimen is significantly enhanced.

#### 3.3.3.3. Strain Energy Release Rate Analysis

EAL modelling was used to construct strain energy release rate profiles at three locations. In the first profile, a crack of length 0.07 inches, centered beneath the load nose, was considered. It was necessary to make the crack this length in order to distance the crack tip from the region of the symmetry plane used in the model. A schematic of the mesh was shown in Figure 12. This crack was assumed at each of the various interfaces, and the resulting strain energy release rates were calculated. This addressed specimen behavior in the region of maximum absolute chord stress and peel stress. In the second profile, this was repeated for an assumed crack of length 0.01 inches, centered 0.40 inches from the load nose, near the region of maximum absolute shear stress. Finally, a crack of length 0.10 inches was assumed

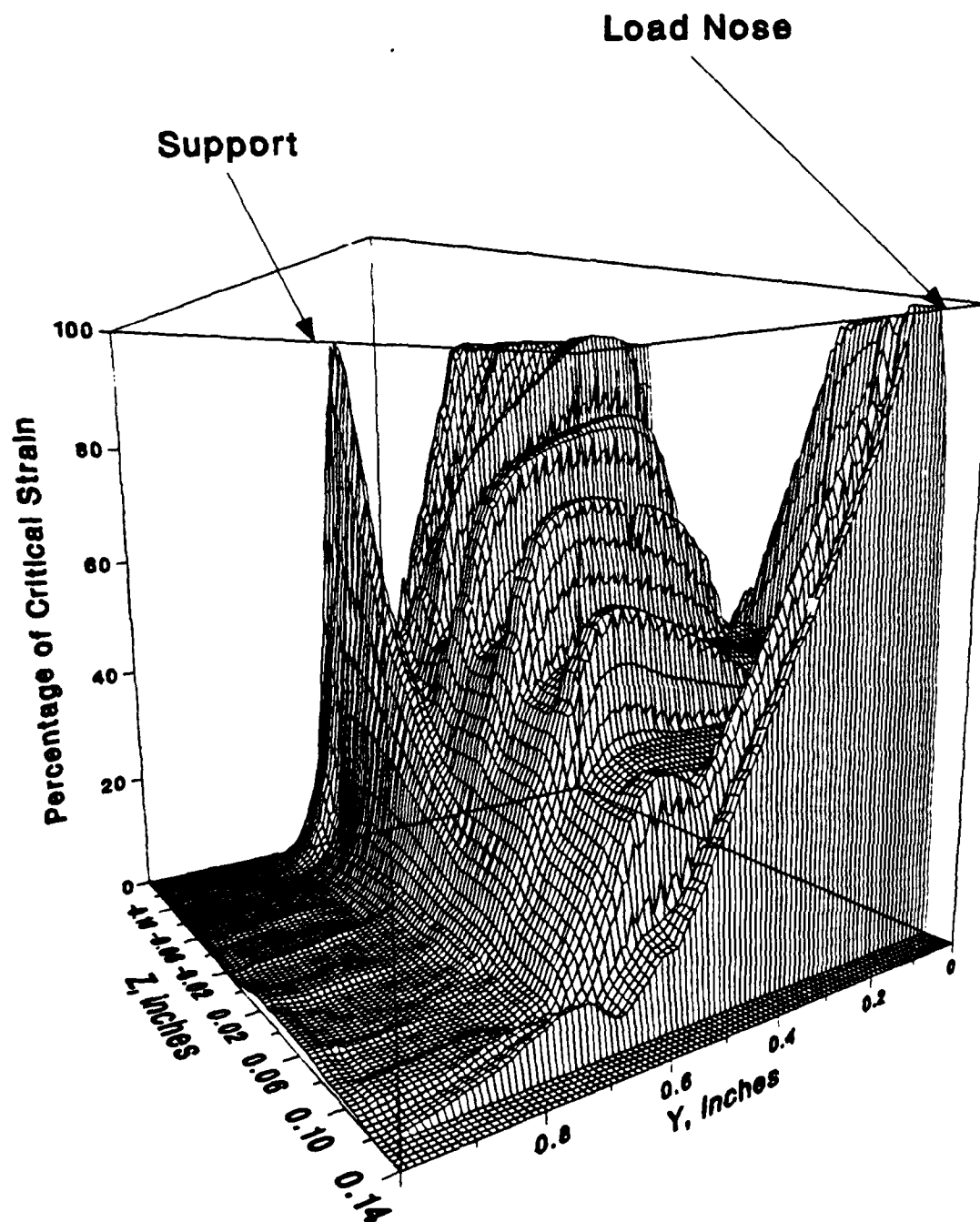


Figure 27: Map of nearness to failure,  
incorporating McCleskey failure modes

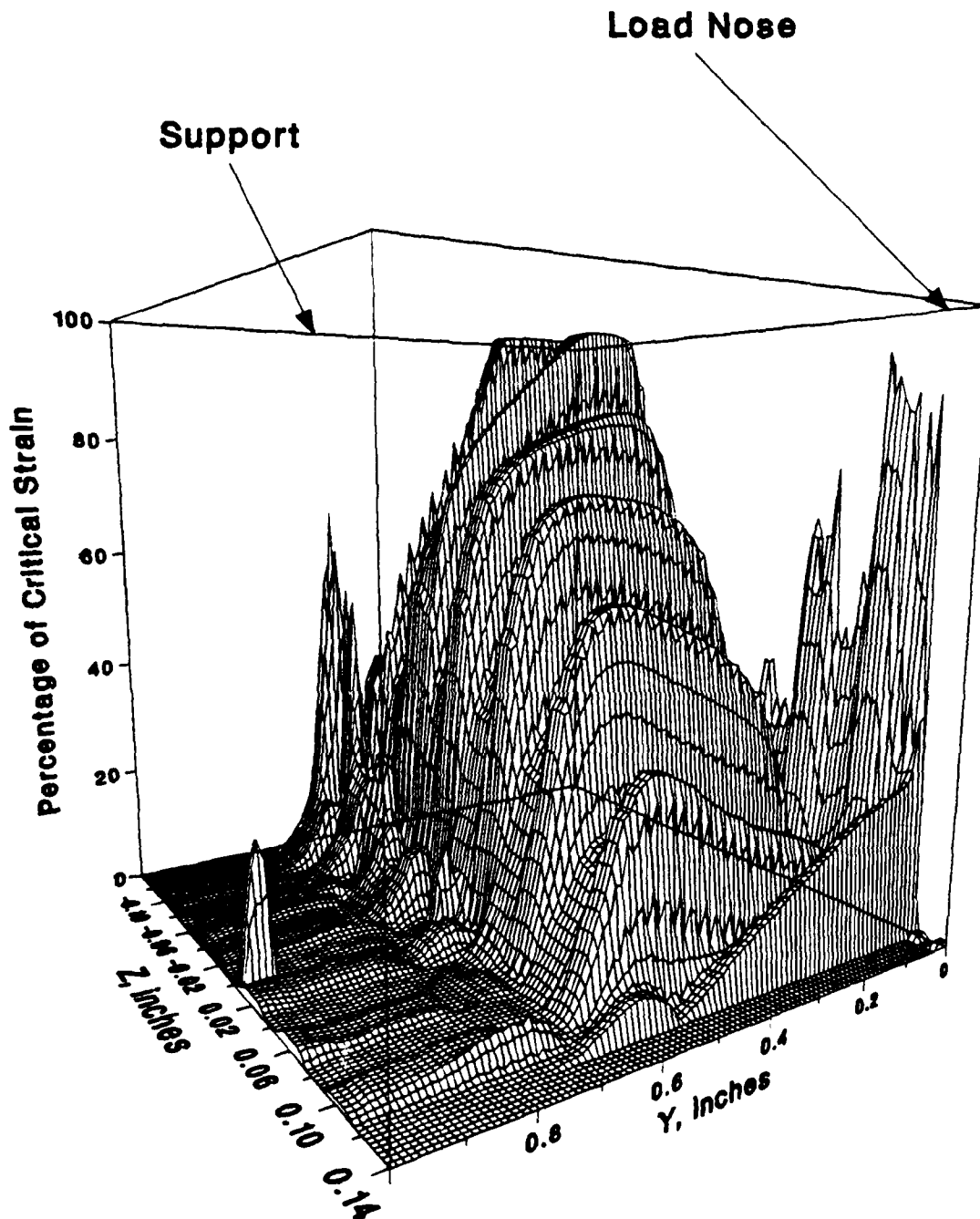


Figure 28: Map of fraction of critical strain due to first McCleskey failure mode

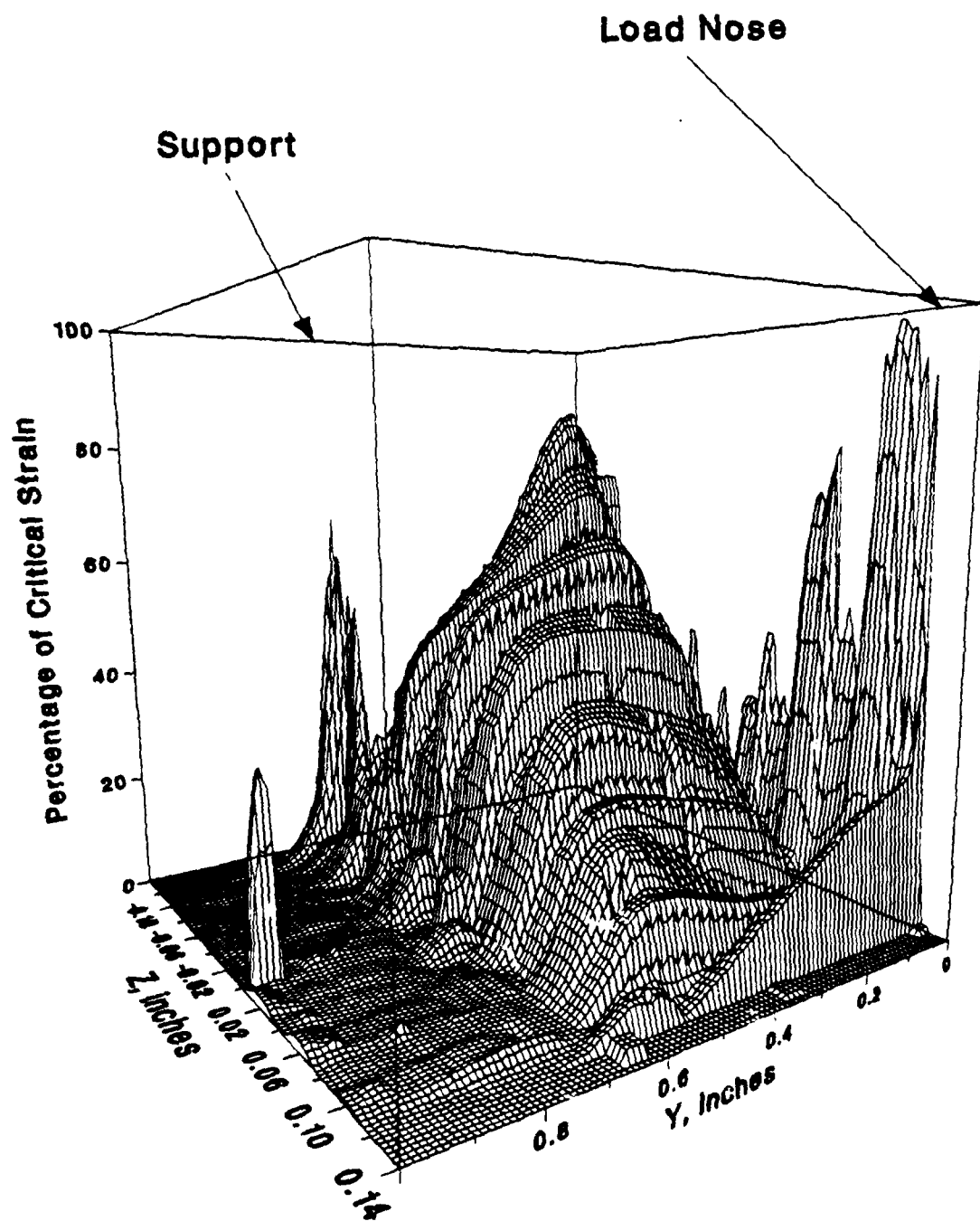


Figure 29: Map of fraction of critical strain due  
to second McCleskey failure mode

at the free end, suggested by initial observation to be the site of crack initiation. The applied load in all cases was 1000 pounds, as with the stress maps.

The profile for the assumed crack near the free end showed what Figures 17, 18, and 19 suggest: negligible values of the strain energy release rate, too small to produce failure. The data for the first two profiles appear as Figure 30. The distance  $x$  is as defined in Figures 17, 18, and 19.

It should be noted that all data points shown in Figure 30 are taken from locations at least 0.04 inches from the surface of the specimen. Thus, for all data points, the peel stress is negligible, as indicated by Figure 17. Consequently, crack growth is predominantly mode II. The spikes in the  $G$ -distribution result from variations in elastic properties from ply to ply.

As shown in Figure 30, the strain energy release rate for assumed interlaminar cracks beneath the load nose increases rapidly as the flaw is placed nearer to the point of application of the load. However, for flaws assumed in the range of high shear stress away from the load nose, strain energy release rates remain relatively negligible. The fracture toughness of AS4/3502 composite is assumed to be 2 in-lb/in<sup>2</sup>; thus, Figure 30 shows that cracking can occur in plies near the load nose, but is unlikely away from this region. This supports the data of Figure 20, which indicate that overstress failure is confined to this same region.

#### **3.3.4. Results of Fractographic Analysis**

Microscopic analysis of a failed specimen showed several pertinent features, many of which were visible with the naked eye after the specimen had been sputter-coated. Directly beneath the load nose, many cracks were observed running perpendicular to the direction of load application. One such is shown in Figure 31. This crack was approximately 0.25 inches long, and was found beneath the load nose, above the midplane.

Figure 32 shows some smaller flaws in the same region. The presence of such



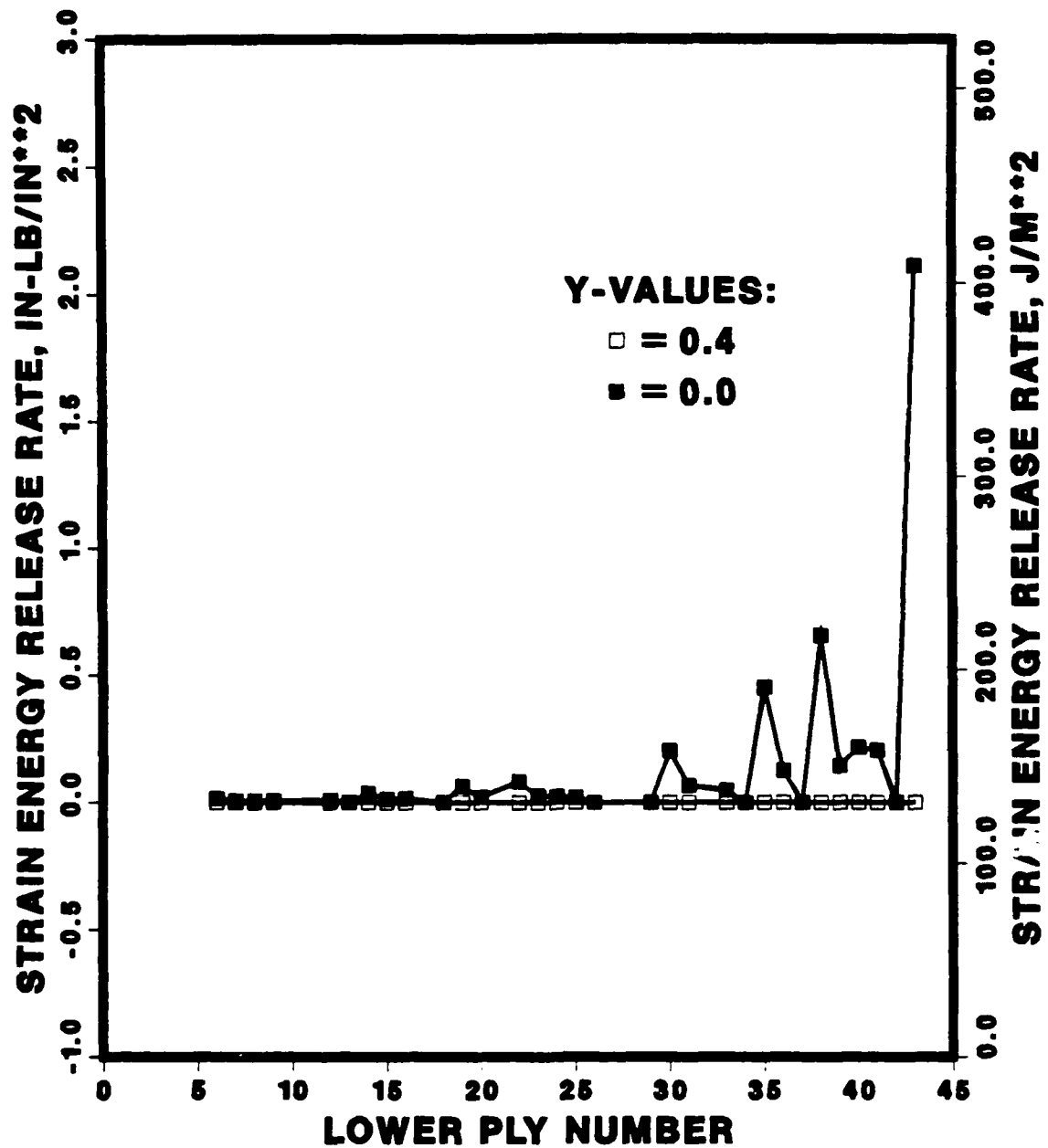


Figure 30: Strain Energy Release Rate Data from EAL

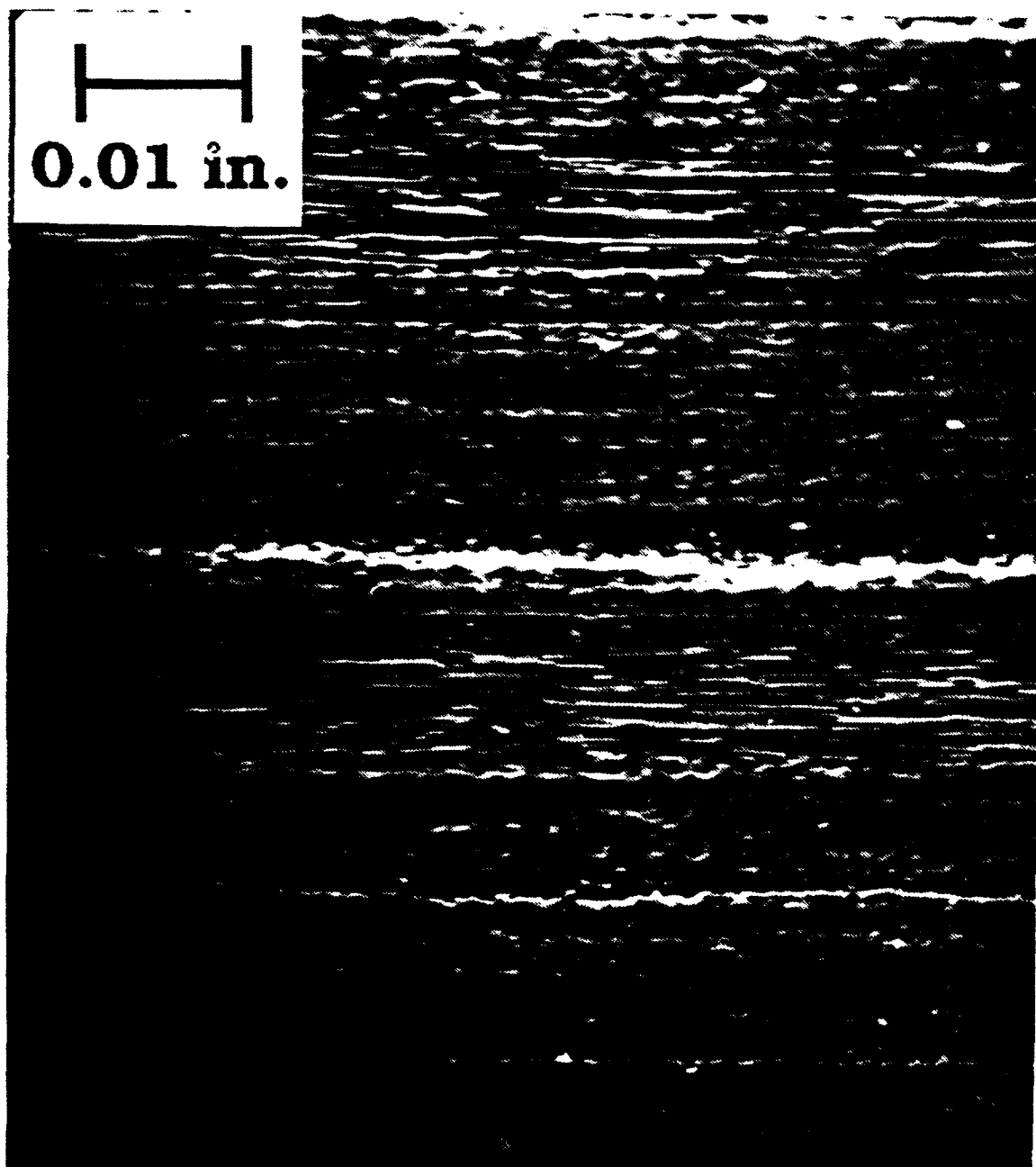


Figure 31: Photomicrograph of crack beneath load nose

flaws supports the analytical determination that extensive damage due to crushing in this region will lead to the growth of cracks.

Figure 33 shows the failure of a 45° ply below the midplane, near the load nose. This ply has experienced matrix failure, splitting in two along the fiber direction. This supports the analytical prediction of ply failure in this location due to chordwise stresses.

The presence of matrix failure suggests an explanation for the failure of all specimens below the midplane. In this region, the chordwise stresses are positive, leading to possible tensile failure of the matrix, which is more likely to lead to complete specimen failure than is the compressive failure which is to be found above the midplane.

Figures 20 and 30 indicate that an interlaminar flaw of length 0.07 inches, centered beneath the load nose, is sufficient to produce interlaminar fracture. Defects of approximately this length have been observed in these specimens.

### **3.3.5. Summary of Fracture Analysis**

Finite element analyses have been used to describe the behavior of a quasi-isotropic short beam specimen. Short beam specimens have been tested and the results compared with the analyses, and the fracture surfaces of failed specimens have been examined.

Fractographic analyses show that numerous small cracks are created directly beneath the load nose, possibly causing fracture to proceed from this location. This is supported by the presence of large magnitudes of peel, shear, and chordwise stresses in the vicinity of the load nose, as shown by the FEM analysis, and by comparison of strain energy release rate values obtained at the same locations.

The following mechanism may be postulated: strains cause matrix failures beneath the load nose. Above the midplane, this failure is caused by crushing stresses in the  $z$ -direction; below the midplane, it is caused by chordwise tensile stresses.

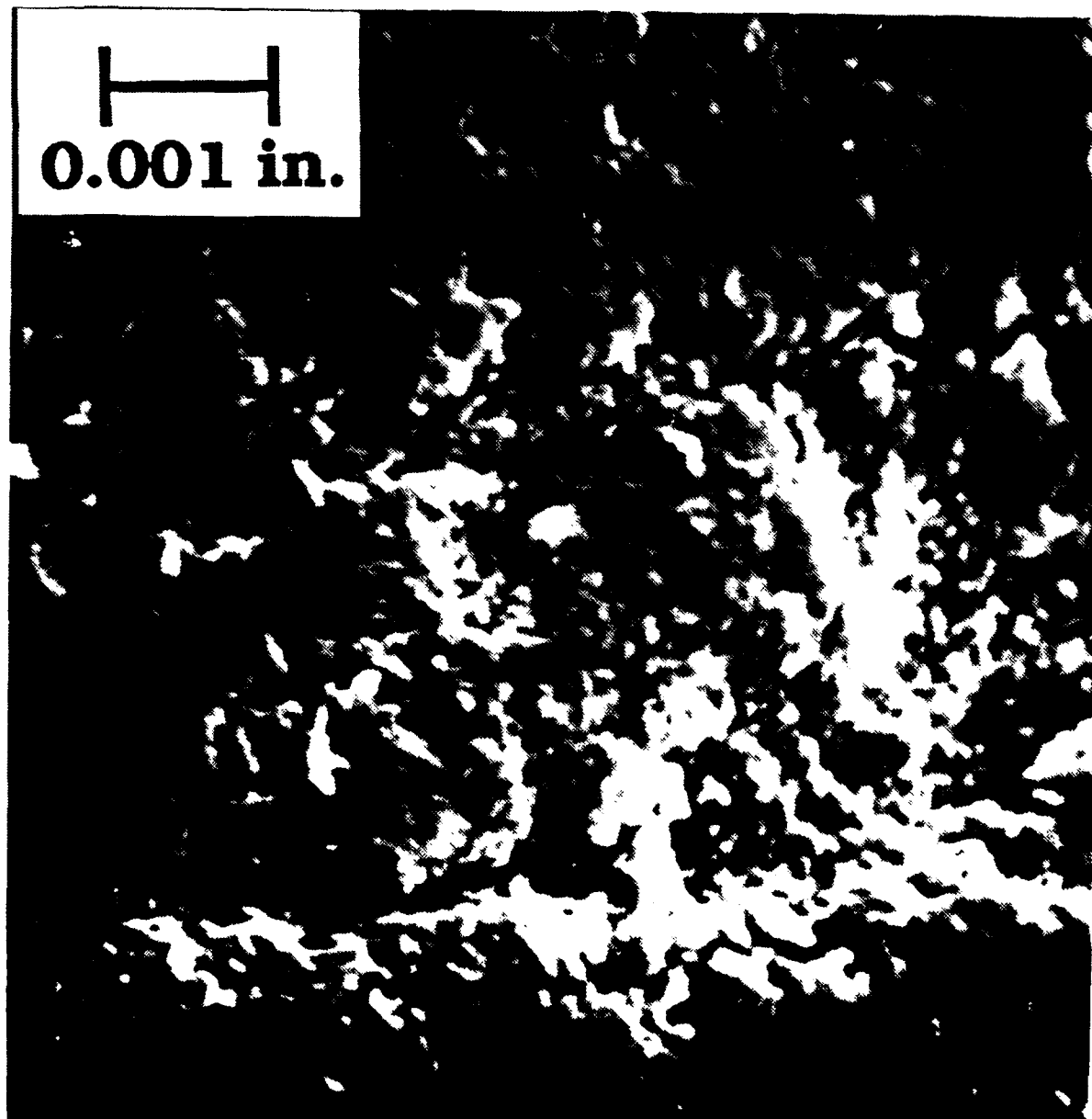


Figure 32: Photomicrograph of small cracks beneath load nose

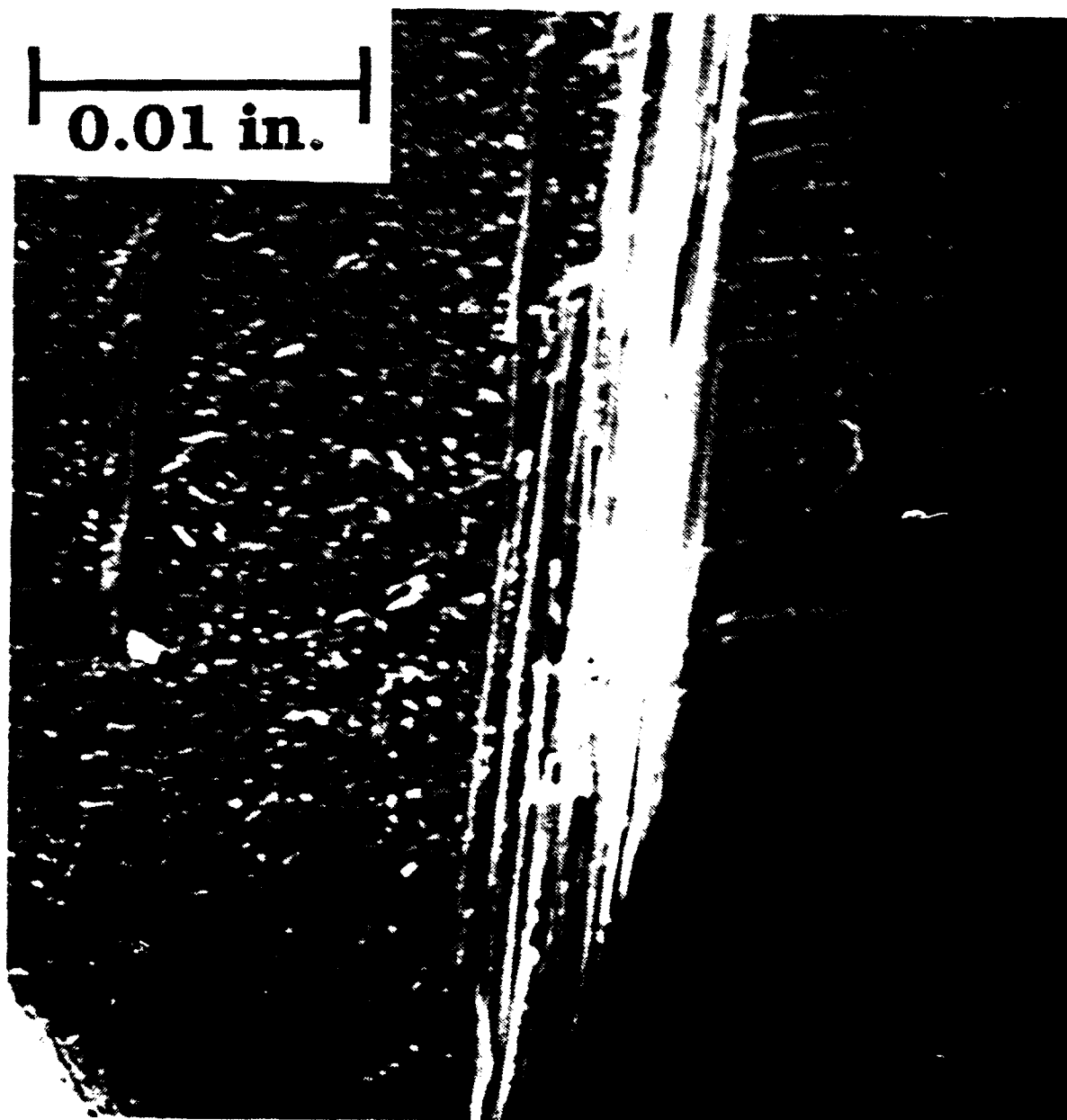


Figure 33: Matrix Failure of a 45° Ply

These regions of damage are sites from which delamination cracks can propagate. Eventually, the region beneath the midplane becomes sufficiently damaged to produce a delamination crack that will propagate to failure. The cracks originating above the midplane are subjected to a compressive chordwise stress, and to a larger compressive peel stress.

The strength of materials method neglects the chordwise and crushing loads which are the driving causes of failure in this type of specimen. Therefore, the three-point short-beam shear test does not measure the interlaminar shear strength of a quasi-isotropic laminated composite. Because of the interaction of damage modes in this configuration, the quantitative data cannot be interpreted as a measure of a simple, isolated failure mode.

**CHAPTER IV:**

**A STRAIN ENERGY RELEASE RATE MODEL  
FOR THE SHORT-BEAM COMPOSITE CONFIGURATION**

**4.1. Introduction**

Current methods of calculating strain energy release rates for the short beam shear specimen can be tedious and expensive. An example is the analysis performed in section 3.3.3.4, using the zero-length element. In the current effort, two simple strain energy release rate models are developed and evaluated. One model assumes that crack growth is driven by bending stresses, while the other assumes that contact stresses near the load nose provide the driving force. The second model is found to provide a better representation of actual specimen behavior, as determined by finite element modelling. This method is seen to be a quick, simple, and inexpensive way to estimate strain energy release rates in cracked composite beams.

Finite element analyses are used to check a design, rather than define a configuration, and consequently do not yield an understanding of the role of the parameters controlling the behavior, such as material and geometry. Closed-form solutions, such

as the global-local model of Pagano and Soni<sup>[48]</sup> and the sublamine model of Reference 19 have been proposed. However, these models can require more time than a preliminary investigation requires, especially if several candidate configurations are to be considered. There is a need for an economical, reasonably accurate strain energy release rate solution method that is easy to use.

Three analysis techniques are used in this work. The first is a linear finite element code, which allows detailed modelling of composite specimens, including ply-by-ply modelling of elastic behavior. These models produce data that can be used as a standard of comparison for solutions from simpler analyses. The two remaining analyses are based upon a general strain energy release rate model for cracked laminates. This solution is specified for two cases: that of a laminated beam in pure bending, and that of a laminated beam under contact loading. The models obtained are applied to specific problems of three-point bending of composites, and the results are compared with those from the finite element model.

## **4.2. Analytical Methods: Williams' Approach**

### **4.2.1. Revision for Laminated Plates**

Reference 28 details a simple, general method for determining the strain energy release rate for a cracked laminate. The revision of this model for the case of laminated plates with arbitrary layup is as follows.

Consider the cracked laminate shown in Figure 34, exposed to loading conditions involving moments, through-thickness shears, and in-plane tensions. For simplicity, begin by taking only the moments into account. For a laminate in bending,



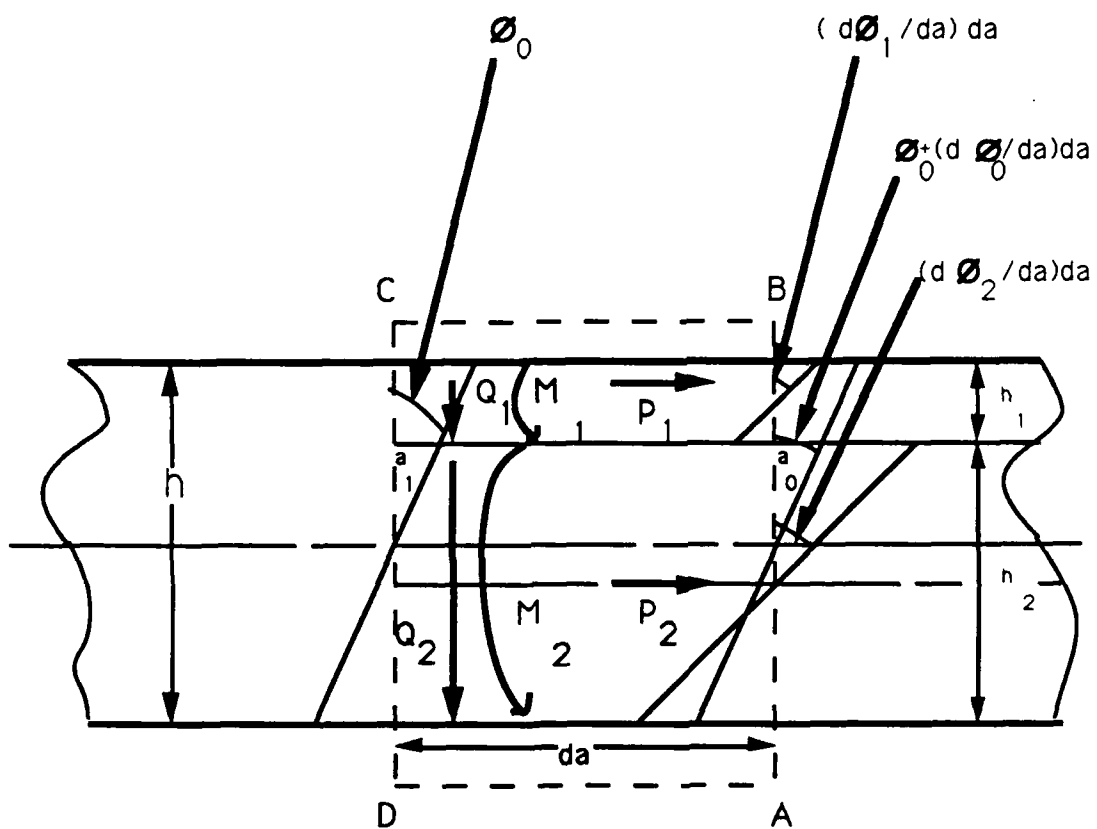


Figure 34. Williams's analysis of a cracked laminate.

$$M_y = B_{12}u^0_{,x} + B_{26}(u^0_{,y} + v^0_{,x}) + B_{22}v^0_{,y} - D_{12}w_{,xx} - 2D_{26}w_{,xy} - D_{22}w_{,yy} \quad [6]$$

where

$M_y$  is the moment on a  $y$ -face

$B_{ij}, D_{ij}$  are stiffnesses from classical laminated plate theory

$u_0, v_0$  are midplane deflections in the length and thickness directions, respectively

Assume that the deflections  $u^0$  and  $v^0$  are identically zero, and that  $w = w(y)$ . Equation [6] reduces to

$$M_y = \frac{-M_T}{B} = -D_{22} \frac{d^2 w}{dy^2} \quad [7]$$

where  $M_T$  is the total applied moment, and  $B$  is the width of the laminate. Rewrite equation [7] as

$$\frac{d^2 w}{dy^2} = \frac{M_T}{BD_{22}} \quad [8]$$

For small inclination angle  $\phi$ , as defined in Figure 34,

$$\phi \approx \frac{dw}{dy} \quad [9]$$

combining equations [8] and [9] gives

$$\frac{d\phi}{dy} = \frac{M_T}{BD_{22}} \quad [10]$$

Consider the contour  $ABCD$  as the crack grows from  $a_0$  to  $a_1$ . The original rotations are  $\phi_0$  at  $CD$  and  $\phi_0 + \left(\frac{d\phi_0}{dy}\right) dy$  at  $AB$ . When the crack has grown from  $a_0$  to  $a_1$ ,

changes in the rotations in the upper and lower arms of the cracked beam become, respectively,

$$\left( \frac{d\phi_1}{dy} - \frac{d\phi_0}{dy} \right) \Delta y \quad \text{and} \quad \left( \frac{d\phi_2}{dy} - \frac{d\phi_0}{dy} \right) \Delta y \quad [11]$$

By equation [8],

$$\frac{d\phi_0}{dy} = \frac{M_1 + M_2}{BD_{22}^{[T]}} \quad [12]$$

$$\frac{d\phi_1}{dy} = \frac{M_1}{BD_{22}^{[1]}} \quad [13]$$

$$\frac{d\phi_2}{dy} = \frac{M_2}{BD_{22}^{[2]}} \quad [14]$$

where  $D_{22}^{[T]}$ ,  $D_{22}^{[1]}$ , and  $D_{22}^{[2]}$  are bending stiffnesses for the entire laminate, the upper arm, and the lower arm, respectively. Define the strain energy release rate  $G$  as

$$G = \frac{1}{B} \left( \frac{dU_e}{da} - \frac{dU_s}{da} \right) \quad [15]$$

where  $U_e$  is the external work performed and  $U_s$  is the strain energy in the beam. Since  $da = dy$ , equation [15] can be rewritten as

$$G = \frac{1}{B} \left( \frac{dU_e}{dy} - \frac{dU_s}{dy} \right) \quad [16]$$

We have

$$dU_e = M_1 \left( \frac{d\phi_1}{da} - \frac{d\phi_0}{da} \right) dy + M_2 \left( \frac{d\phi_2}{da} - \frac{d\phi_0}{da} \right) dy \quad [17]$$

Substituting in equations [12] through [14] gives

$$\frac{dU_e}{dy} = \frac{1}{B} \left[ \frac{M_1^2}{D_{22}^{[1]}} + \frac{M_2^2}{D_{22}^{[2]}} - \frac{(M_1 + M_2)^2}{D_{22}^{[T]}} \right] \quad [18]$$

The strain energy in the beam is given by

$$\frac{dU_s}{dy} = \frac{1}{2} \frac{M^2}{BD_{22}} \quad [19]$$

thus,

$$\frac{dU_s}{dy} = \frac{1}{2} \left[ \frac{M_1^2}{BD_{22}^{[1]}} + \frac{M_2^2}{BD_{22}^{[2]}} - \frac{(M_1 + M_2)^2}{BD_{22}^{[T]}} \right] \quad [20]$$

or,

$$\frac{dU_s}{dy} = \frac{1}{2B} \left[ \frac{M_1^2}{D_{22}^{[1]}} + \frac{M_2^2}{D_{22}^{[2]}} - \frac{(M_1 + M_2)^2}{D_{22}^{[T]}} \right] \quad [21]$$

Insert equations [18] and [21] into equation [15] and get

$$G_M = \frac{1}{2B} \left[ \frac{M_1^2}{D_{22}^{[1]}} + \frac{M_2^2}{D_{22}^{[2]}} - \frac{(M_1 + M_2)^2}{D_{22}^{[T]}} \right] \quad [22]$$

The development of  $G_P$ , the strain energy release rate due to lengthwise loads, is similar to that for  $G_M$ , and results in

$$G_P = \frac{1}{2B^2h} \left[ \frac{P_1^2}{\xi E_1} + \frac{P_2^2}{(1 - \xi) E_2} - \frac{(P_1 + P_2)^2}{E_T} \right] \quad [23]$$

To derive  $G_Q$ , the strain energy release rate due to through-thickness shears, begin with the equation found in Langhaar<sup>[49]</sup> for the strain energy of a beam due to shear:

$$\frac{dU_s}{da} = \frac{\kappa Q^2}{2GA} \quad [24]$$

where

$\kappa$  is a constant determined by the cross-sectional geometry of the beam;  $\kappa = 1.20$  for a rectangular cross-section

$Q$  is the shear force in the beam

$G$  is the shear modulus of the beam

$A$  is the cross-sectional area of the beam;  $A = Bh$

Reference 28 notes that equation [15] can be written as

$$G = \frac{1}{B} \frac{dU_c}{da} \Big|_{load\ constant} \quad [25]$$

where  $U_c$  is the complementary energy  $\int u dP$ , which is equal to  $U_s$  for the linear case. Thus,

$$G = \frac{1}{B} \frac{dU_s}{da} \Big|_{load\ constant} \quad [26]$$

so the similarity between the right-hand sides of equations [21] and [22] is not coincidental. Thus, we have

$$G_Q = \frac{dU_s}{da} = \frac{dU_s}{dy} = \frac{\kappa}{2B} \left( \frac{Q^2}{Gh} \right) \quad [27]$$

and, by a development similar to that of equation [23],

$$G = \frac{\kappa}{2B^2h} \left[ \frac{Q_1^2}{\mathcal{G}_1\xi} + \frac{Q_2^2}{\mathcal{G}_2(1-\xi)} - \frac{(Q_1 + Q_2)^2}{\mathcal{G}_T} \right] \quad [28]$$

It should be noted that the expression for  $G_Q$  developed in Reference 28 cannot be used for the inhomogeneous case, as it presumes a parabolic distribution of the shear stress through the thickness, and the shear stress distribution in a laminate is *piecewise* parabolic.

#### 4.2.2. Development of Bending Model

If the stress resultants  $N_y$ ,  $M_y$ , and  $Q_{yz}$  could be evaluated for each ply in a laminate, these quantities, multiplied by the beam width, could be summed on each side of an assumed crack to get the quantities  $M_1$ ,  $M_2$ ,  $P_1$ ,  $P_2$ ,  $Q_1$ , and  $Q_2$  for use in the strain energy release rate equations [22], [23], and [28]. From Ashton and Whitney<sup>[50]</sup>, the stresses for the  $k^{th}$  ply in a laminated beam are

$$\begin{aligned} \sigma_y^{(k)} = & Q_{12}^{(k)} u^0_{,x} + Q_{26}^{(k)} (u^0_{,y} + v^0_{,x}) + Q_{22}^{(k)} v^0_{,y} \\ & - z \left( Q_{12}^{(k)} w_{,xx} + 2Q_{26}^{(k)} w_{,xy} + Q_{22}^{(k)} w_{,yy} \right) \end{aligned} \quad [29]$$

$$\begin{aligned} \sigma_{yz}^{(k)} = & \frac{z^2}{2} \left[ Q_{16}^{(k)} w_{,xxx} + (Q_{12}^{(k)} + 2Q_{66}^{(k)}) w_{,xxy} + 3Q_{26}^{(k)} w_{,xyy} + Q_{22}^{(k)} w_{,yyy} \right] \\ & - z \\ & \times \left[ Q_{16}^{(k)} u^0_{,xx} + (Q_{12}^{(k)} + Q_{66}^{(k)}) u^0_{,xy} + Q_{26}^{(k)} u^0_{,yy} + Q_{66}^{(k)} v^0_{,xx} + 2Q_{26}^{(k)} v^0_{,xy} + Q_{22}^{(k)} v^0_{,yy} \right] \\ & + \gamma^{(k)}(x, y) \end{aligned} \quad [30]$$

where  $Q_{ij}$  are the transformed reduced stiffnesses, and  $\gamma^{(k)}(x, y)$  are functions of integration that are determined by interlaminar continuity conditions, and by the

requirement that  $\sigma_{yz}$  vanish at the upper and lower surfaces of the beam. For the beam problem, equations [29] and [30] simplify to

$$\sigma_y^{(k)} = -zQ_{22}^{(k)}w_{,yy} \quad [31]$$

and

$$\sigma_{yz}^{(k)} = \frac{z^2}{2}Q_{22}^{(k)}w_{,yyy} + \gamma^{(k)}(x, y) \quad [32]$$

From the requirement that the upper and lower beam surface tractions be zero, we find

$$\gamma^{(1)}(x, y) = -\frac{(h/2)^2}{2}Q_{22}w_{,yyy} \quad [33]$$

where the bottom ply is designated ply # 1, and where  $(h/2)$  is the half-thickness of the beam. The plies of a laminate are in series, not in parallel, as regards shear loading; thus, shear stress continuity, not shear displacement continuity, is required at the interfaces. Requiring

$$\sigma_{yz}^{(k)} = \sigma_{yz}^{(k+1)} \quad [34]$$

at the interface between the  $k^{th}$  and  $(k+1)^{th}$  plies leads to the recursion relationship

$$\gamma^{(k+1)}(x, y) = \gamma^{(k)}(x, y) + \frac{z_o^2}{2}(Q_{22}^{(k)} - Q_{22}^{(k+1)})w_{,yyy} \quad [35]$$

where  $z_0$  is the  $z$ -coordinate of the interface of the two plies. Now, recall that

$$N_y = \int_{-\frac{h}{2}}^{\frac{h}{2}} \sigma_y dz \quad [36]$$

$$M_y = \int_{-\frac{h}{2}}^{\frac{h}{2}} z \sigma_y dz \quad [37]$$

$$Q_y = \int_{-\frac{h}{2}}^{\frac{h}{2}} \sigma_{yz} dz \quad [38]$$

Substituting-in equations [31] and [32] gives

$$N_y = \frac{1}{2} w_{,yy} \sum_{k=1}^N Q_{22}^{(k)} (z_{k+1}^2 - z_k^2) \quad [39]$$

$$M_y = \frac{1}{3} w_{,yy} \sum_{k=1}^N Q_{22}^{(k)} (z_{k+1}^3 - z_k^3) \quad [40]$$

$$Q_y = \sum_{k=1}^N \left[ \gamma^{(k)}(x, y) \times (z_{k+1} - z_k) + \frac{1}{6} w_{,yyy} Q_{22}^{(k)} (z_{k+1}^3 - z_k^3) \right] \quad [41]$$

Thus, the relevant stress resultants can be found if  $w_{,yy}$  can be determined. Assuming the beam to be in pure bending, with no external lengthwise or shearing loads, the strain energy release rate can be found by determining  $M_y$  above and below the crack, and substituting these values into equation [22]. An expression for the beam deflection is therefore necessary.

In the derivation of a deflection model, the role of shear deformation is an important factor. In isotropic materials, the ratio of the extensional modulus to the



shear modulus,  $E/G$ , does not exceed about 2.6. In composite materials, however, this ratio can be as high as 60. Thus, the ratio of shear deformation to extension is much higher in composites, making it especially important to include shear in a deflection model. Such a model is derived using the sublamine analysis of Reference 19.

For plane stress in the  $y - z$  plane, equation [A - 14], from the appendix on sublamine analysis, reduces to:

$$\begin{bmatrix} A_{22} \frac{d^2}{dy^2} & 0 & B_{22} \frac{d^2}{dy^2} \\ 0 & -A_{44} \frac{d^2}{dy^2} & -A_{44} \frac{d}{dy} \\ B_{22} \frac{d^2}{dy^2} & -A_{44} \frac{d}{dy} & (D_{22} \frac{d^2}{dy^2} - A_{44}) \end{bmatrix} \begin{Bmatrix} V \\ W \\ \beta_y \end{Bmatrix} = - \begin{Bmatrix} \alpha_y \\ -q \\ m_y \end{Bmatrix} \quad [42]$$

Equation [42] can be written as

$$\begin{bmatrix} A_{22} & 0 & B_{22} \\ 0 & -A_{44} & 0 \\ B_{22} & 0 & D_{22} \end{bmatrix} \begin{Bmatrix} X'' \end{Bmatrix} + \begin{bmatrix} 0 & 0 & 0 \\ 0 & 0 & -A_{44} \\ 0 & -A_{44} & 0 \end{bmatrix} \begin{Bmatrix} X' \end{Bmatrix} + \begin{bmatrix} 0 & 0 & 0 \\ 0 & 0 & 0 \\ 0 & 0 & -A_{44} \end{bmatrix} \begin{Bmatrix} X \end{Bmatrix} = \begin{Bmatrix} f \end{Bmatrix} \quad [43]$$

Equation [43] can be written as

$$[A]\{X''\} + [B]\{X'\} + [C]\{X\} = \{f\} \quad [44]$$

where  $\{X\}$  is the column vector  $\{V \ W \ \beta_y\}^T$  and primes denote differentiation with respect to  $y$ . Use of Laplace transforms results in

$$\begin{aligned} (s^2[A] + s[B] + [C])\{X(s)\} &= \{\bar{f}(s)\} + [A](s\{X(0)\} + \{X'(0)\}) + [B]\{X(0)\} \\ &\equiv \{\bar{R}(s)\} \end{aligned} \quad [45]$$

Now define

$$[\bar{Z}(s)] = s^2[A] + s[B] + [C] \quad [46]$$

The Laplace transform of the solution vector is given by

$$\{\bar{X}(s)\} = [\bar{Z}(s)]^{-1} \{\bar{R}(s)\} \quad [47]$$

Consider one half of the short-beam specimen,  $0 < y < L$ , as a sublaminates. Note that at  $y = 0$ ,  $\beta_y = 0$ , and  $W' = 0$ . Note also that  $\alpha_y$  and  $m_y$  are zero on the boundaries. Finally, note that the function  $V(y)$  is the deflection of points along the midplane in the  $y$ -direction, which is neglected. This simplifies the system to a  $2 \times 2$  when the  $V$ - and  $V'$  terms are dropped. Significantly, it also removes the coupling stiffness  $B_{22}$  from the solution. With these simplifications, evaluation of  $\{\bar{R}(s)\}$  from equation [44] gives

$$\{\bar{R}(s)\} = \left\{ \begin{array}{c} \bar{q} - sA_{44}W_0 \\ D_{22}\beta'_{y0} - A_{44}W_0 \end{array} \right\} \quad [48]$$

where 0-subscripts denote values at  $y = 0$ . Using equation [46] gives

$$[\bar{Z}(s)] = \begin{bmatrix} -s^2 A_{44} & -s A_{44} \\ -s A_{44} & (s^2 D_{22} - A_{44}) \end{bmatrix} \quad [49]$$

which can be inverted, giving

$$[\bar{Z}(s)]^{-1} = \begin{bmatrix} \left( \frac{1}{s^4 D_{22}} - \frac{1}{s^2 A_{44}} \right) & \frac{-1}{s^3 D_{22}} \\ \frac{-1}{s^3 D_{22}} & \frac{1}{s^2 D_{22}} \end{bmatrix} \quad [50]$$

Substitute equations [48] and [50] into equation [47] and obtain expressions for the Laplace transforms of the deflection and the rotation:

$$\bar{W} = \frac{\bar{q}}{s^4 D_{22}} - \frac{\bar{q}}{s^2 A_{44}} + \frac{W_0}{s} - \frac{\beta'_{y0}}{s^3} \quad [51]$$

$$\bar{\beta}_y = -\frac{\bar{q}}{s^3 D_{22}} + \frac{\beta'_{y0}}{s^2} \quad [52]$$

Model the load using singularity functions:

$$q = -\frac{P}{2} \langle y \rangle_{-1} + \frac{P}{2} \langle y - c \rangle_{-1} \quad [53]$$

and obtain the displacement and rotation functions

$$W = \frac{P}{12D_{22}} (\langle y - c \rangle^3 - y^3) - \frac{P}{2A_{44}} (\langle y - c \rangle^1 - y) + W_0 - \frac{\beta'_{y0} y^2}{2} \quad [54]$$

$$\beta_y = -\frac{P}{4D_{22}} (\langle y - c \rangle^2 - y^2) + \beta'_{y0} y \quad [55]$$

Requiring that  $W(c) = 0$  and  $W''(L) = 0$  gives two equations that can be solved for  $W_0$  and  $\beta'_{y0}$ . The resulting solutions are

$$W_0 = -\left( \frac{Pc^3}{6D_{22}} + \frac{Pc}{2A_{44}} \right) \quad [56]$$

$$\beta'_{y0} = -\frac{Pc}{2D_{22}} \quad [57]$$

This solution incorporates shear effects through the rotations  $\beta_y$ , and through the influence of the shear stiffness  $A_{44}$  on the deflection.

Note that

$$\frac{d^2 W}{dy^2} = w_{,yy} = \frac{P}{2D_{22}}(\langle y - c \rangle^1 - y) - \frac{P}{2A_{44}}\langle y - c \rangle_{-1} - \beta'_{y0} \quad [58]$$

This deflection function can now be substituted into equations [39], [40], and [41] to find  $M_1$  and  $M_2$ . In addition, it is determined by inspection of the problem that

$$P_1 = P_2 = Q_1 = Q_2 = 0 \quad [59]$$

#### 4.2.3. Contact Stress Model

Terms for the Williams equations can also be derived using only the contact stress field due to the central load. The situation is modelled as shown in Figure 35. Consider one half of a beam subjected to a central contact load. The load creates a radial stress field that has some resultant force in the chordwise direction. This resultant can be found by integrating the tractions predicted from the stress field along the boundary ABC. This solution is only approximate, since the presence of free surfaces will alter the stress field produced by the contact load.

A similar analysis may be applied to one half of a beam with a centered flaw beneath the load. Assuming that the surfaces of the crack are free to slide, those surfaces are free of tractions in the chordwise direction. It can be assumed, therefore, that the plane of the crack forms a barrier to chordwise forces generated by the contact stress field, and that a chordwise force resultant exists above the crack, but not below it. Considering the region above the crack as analogous with the half-beam of Figure 35(a), the tractions may again be integrated along the boundary ABC. However, only the upper crack surface, defined by the line BC, is stress-free in this case. Thus, the resultant chordwise force above the crack may be approximated

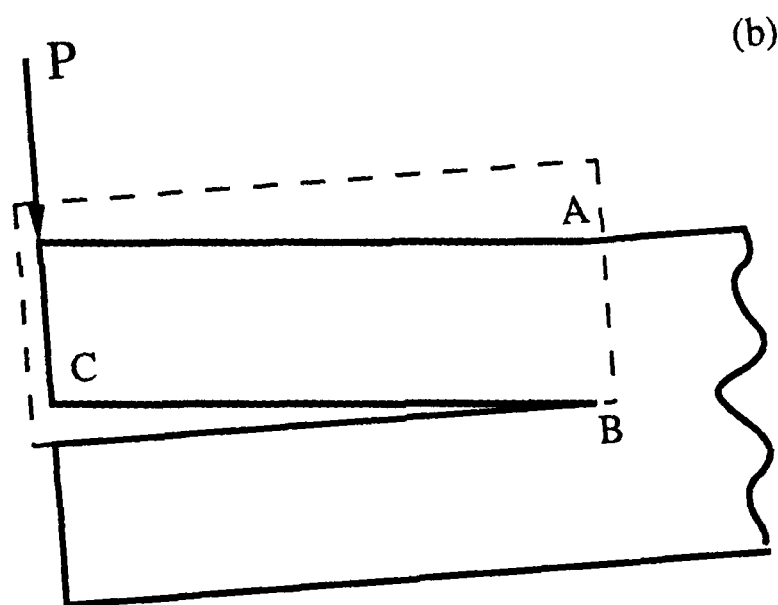
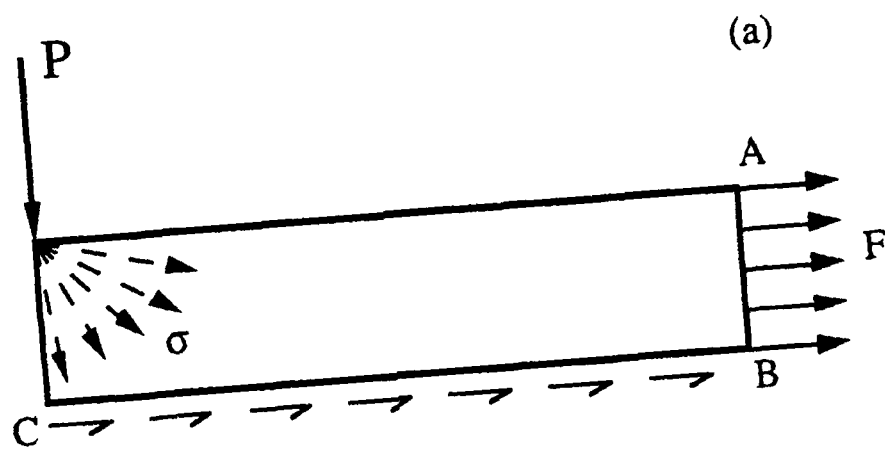


Figure 35. (a) Half-beam with contact stress field  
 (b) Same beam with centered flaw

by integrating the shear tractions across the upper crack surface, and by substituting this resultant force,  $F_{total}$ , in as  $P_1$  in equation [23].

It is seen that

$$F_{total} = B \int_0^a \sigma_{yz} dz \quad [60]$$

The contact stress in an anisotropic half-plane subjected to a concentrated load is given by Lekhnitskii<sup>[51]</sup>:

$$\sigma_{rr} = -\frac{P(\lambda_1 + \lambda_2)}{B} \sqrt{S_{11}S_{22}} \frac{\cos \theta}{\pi r L(\theta)} \quad [61]$$

$$\sigma_{\theta\theta} = \sigma_{r\theta} = 0 \quad [62]$$

where

$\lambda_1, \lambda_2$  are roots of the characteristic equation  $S_{11}\lambda^4 - (2S_{12} + S_{66})\lambda^2 + S_{22} = 0$   
 $S_{11}, S_{22}$  are composite compliances

$$L(\theta) = S_{11} \sin^4 \theta + (2S_{12} + S_{66}) \sin^2 \theta \cos^2 \theta + S_{22} \cos^4 \theta$$

Changing to the  $y - z$  coordinate system, as shown in Figure 36, the shear stress is found to be:

$$\sigma_{yz} = -\sigma_{rr} \sin \theta \cos \theta \quad [63]$$

$$= -P(\lambda_1 + \lambda_2) \sqrt{S_{11}S_{22}} \frac{\cos^2 \theta \sin \theta}{\pi r L(\theta)} \quad [64]$$

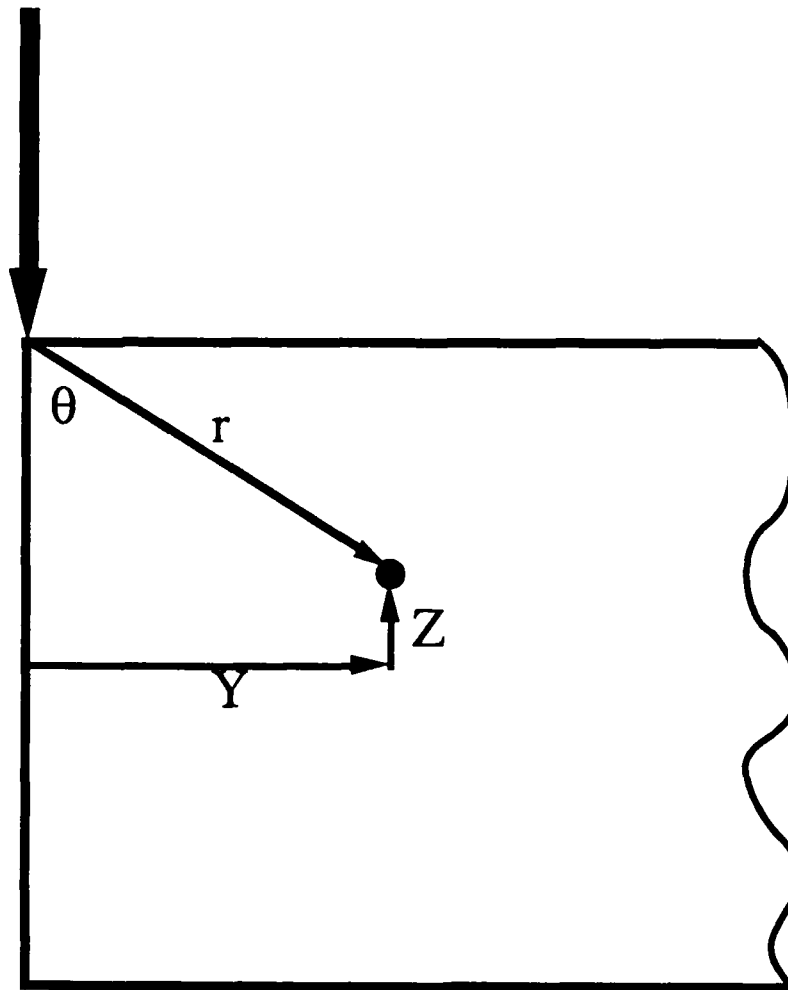


Figure 36. The  $r - \theta$  coordinate system.

Define

$$C_0 = \frac{1}{\frac{h}{2} - z} \quad [65]$$

$$K_0 = \frac{P(\lambda_1 + \lambda_2)\sqrt{S_{11}S_{22}}}{\pi B} \quad [66]$$

It is seen that

$$\sin \theta = \frac{C_0 y}{\sqrt{1 + C_0^2 y^2}} \quad \text{and} \quad \cos \theta = \frac{1}{\sqrt{C_0^2 y^2}} \quad [67]$$

and thus,

$$\sigma_{yz} = K_0 \left( \frac{1}{\pi r} \right) \left( \frac{1}{\sqrt{1 + C_0^2 y^2}} \right) \left( \frac{C_0 y}{1 + C_0^2 y^2} \right) \left( \frac{1}{L(\theta)} \right) \quad [68]$$

$$= \frac{K_0 C_0^2 y}{S_{11} C_0^4 y^4 + (2S_{12} + S_{66}) C_0^2 y^2 + S_{22}} \quad [69]$$

The resultant force along the crack surface is

$$F_{total} = B \int_0^a \sigma_{yz} dy \quad [70]$$

$$= B K_0 C_0^2 \int_0^a \frac{y dy}{S_{11} C_0^4 y^4 + (2S_{12} + S_{66}) C_0^2 y^2 + S_{22}} \quad [71]$$

The integration is performed by partial fractions expansion. The denominator of equation [71] is seen to have two pairs of complex conjugate roots, and the result



of the integration is

$$F_{total} = \frac{\Gamma B K_0}{S_{11} C_0^2} \int_0^a \left( \frac{y}{y^2 + \eta_1} - \frac{y}{y^2 + \eta_2} \right) dy \quad [72]$$

where

$$\eta_1 = \left( \frac{(2S_{12} + S_{66}) - \sqrt{(2S_{12} + S_{66})^2 - 4S_{11}S_{22}}}{2S_{11}C_0^2} \right) \quad [73]$$

$$\eta_2 = \left( \frac{(2S_{12} + S_{66}) + \sqrt{(2S_{12} + S_{66})^2 - 4S_{11}S_{22}}}{2S_{11}C_0^2} \right) \quad [74]$$

$$\Gamma = \frac{-1}{\eta_1 - \eta_2} \quad [75]$$

Completing the integration from equation [72],

$$F_{total} = P_1 = \frac{\Gamma B K_0}{S_{11} C_0^2} \left[ \frac{1}{2} \ln \left( \frac{y^2 + \eta_1}{y^2 + \eta_2} \right) \right]_0^a \quad [76]$$

$$= \frac{\Gamma B K_0}{2S_{11} C_0^2} \ln \left( \frac{\eta_2(a^2 + \eta_1)}{\eta_1(a^2 + \eta_2)} \right) \quad [77]$$

$$= \frac{-BK_0}{2\sqrt{(2S_{12} + S_{66})^2 - 4S_{11}S_{22}}} \ln \left( \frac{\eta_2(a^2 + \eta_1)}{\eta_1(a^2 + \eta_2)} \right) \quad [78]$$

and, by inspection,

$$P_2 = M_1 = M_2 = Q_1 = Q_2 = 0 \quad [79]$$

The finite element method was used to obtain strain energy release rate data with which to compare the results of these models. Since geometrically nonlinear effects are negligible for the short beam shear configuration considered, the finite element code used was EAL, employing four-node, isoparametric elements. A flaw of length 0.7 inches, centered beneath the load nose, was assumed. This placed the tips of the crack in a region where, according to the results of section 3.3.3.1, the stress state is well described by beam theory. This assumed flaw was placed at various depths in the specimen, in order to consider the effect of vertical location on the associated strain energy release rate.

Although there are high compressive peel stresses in the vicinity of the load, all assumed cracks were sufficiently far from the load nose that peel stresses could be considered negligible. The strength of materials and contact stress analyses both assumed pure mode II cracking, the former because the rotation angle  $\phi$  was assumed to be the same for the regions above and below the crack, the latter because  $G_P$  is necessarily mode II. Thus, for the finite element model and the analytical models,  $G = G_{II}$ .

It should be noted that this analysis assumes that friction between the upper and lower crack surfaces is negligible. This reduces the complexity of the model. A delamination analysis that includes the influence of friction was presented in Reference 49 for a quasi-isotropic double cracked lap shear specimen subjected to compression loading. A coulomb friction was assumed, and the cracked portion was subjected to compressive peel stress and friction shear. A range of friction coefficients was considered. It was found that the dominant factor was the suppression of the opening mode (mode I) behavior associated with the compressive loading, rather than the intensity of the friction coefficient between the crack surfaces.

Two layups were considered: a unidirectional layup, with all fibers in the graphite/epoxy running along the length of the specimen, and; a quasi-isotropic [ $\mp 45/0/$

90]<sub>6s</sub> layup.

### 4.3. Results and Discussion

Results showed significant differences between strain energy release rates calculated by the shear deformation model and those obtained from finite element results. Comparisons are shown in Figure 37, for the quasi-isotropic configuration, and Figure 38, for the unidirectional configuration. The pattern is the same in both cases: the model over-predicts near the bottom surface, and under predicts near the load nose. More importantly, the results from this model do not explain the trend in the finite element data, which increases sharply near the load nose. Rather, this model predicts that the strain energy release rate will be symmetric about the specimen midplane, and will decline near either free surface. This indicates that the assumption of a pure bending stress field, made when deriving equations 9 through 12, is inaccurate.

A detailed examination of the stress field for the cracked configuration is informative. While the tip of the crack under consideration is well removed from the region of influence of contact stresses in the uncracked configuration, it passes through that region, resulting in a shear stress concentration above the crack. This is illustrated in Figures 39 and 40, which show shear stress distributions through the thickness, near the crack tip. Figure 39 is for a configuration cracked 14 interfaces below the midplane, and Figure 40 is for a configuration cracked 14 interfaces above the midplane. Figures 41 and 42 show that a crack closer to the load nose also has a much greater effect on the distribution of chordwise stresses than does a crack below the midplane. Figures 39 through 42 also show strength of materials stress solutions for a beam with smeared properties in bending, as a check for the reasonableness of the finite element results. Since the finite element analysis includes ply-by-ply elastic properties, some jaggedness is introduced into its stress curves. The strength of materials solutions in Figures 39 through 42 are derived

# QUASI-ISOTROPIC SHORT BEAM, 1 KIP

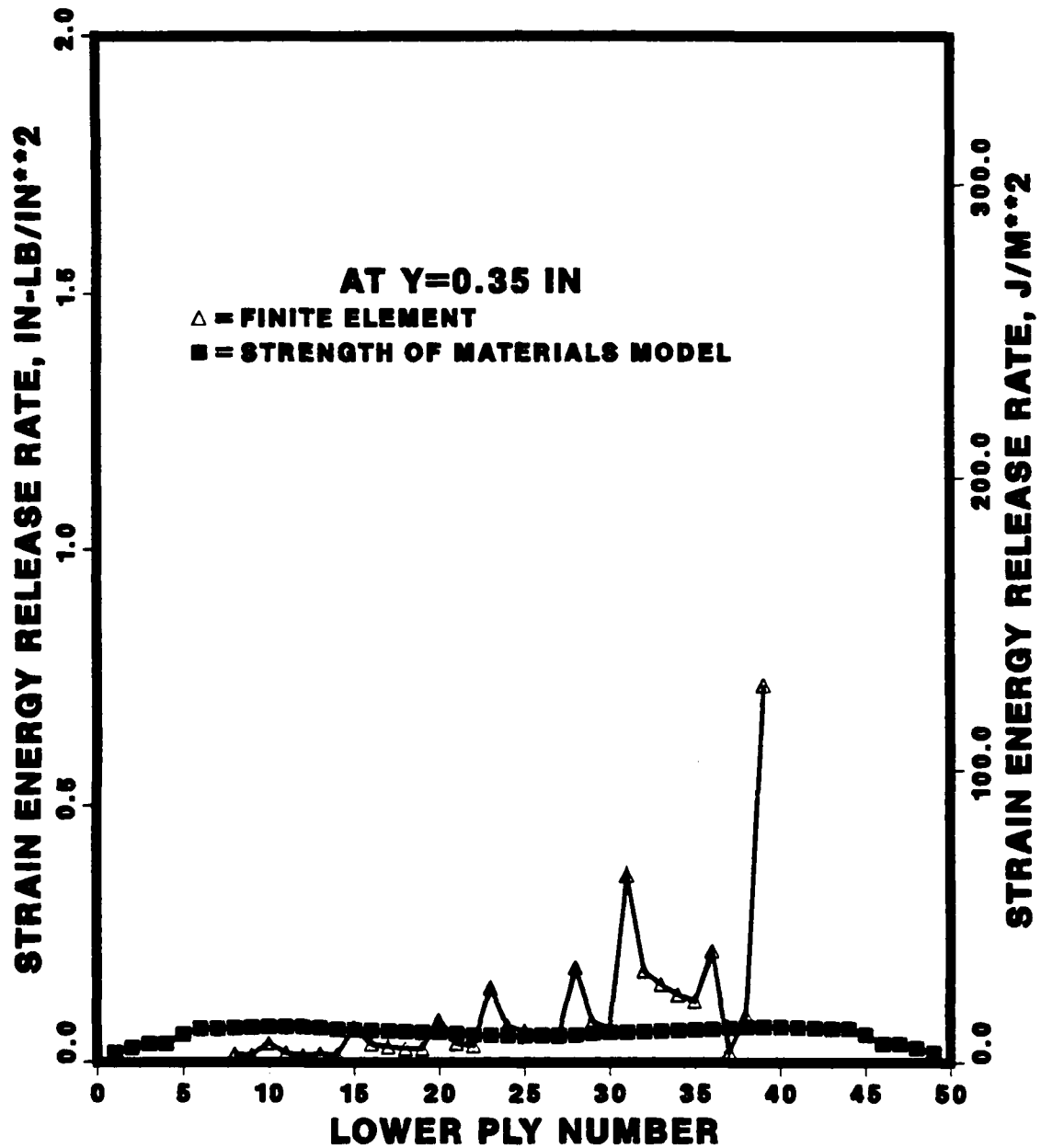


Figure 37. Strain energy release rate comparison for a quasi-isotropic beam, using strength of materials model

# UNIDIRECTIONAL SHORT BEAM, 1 KIP

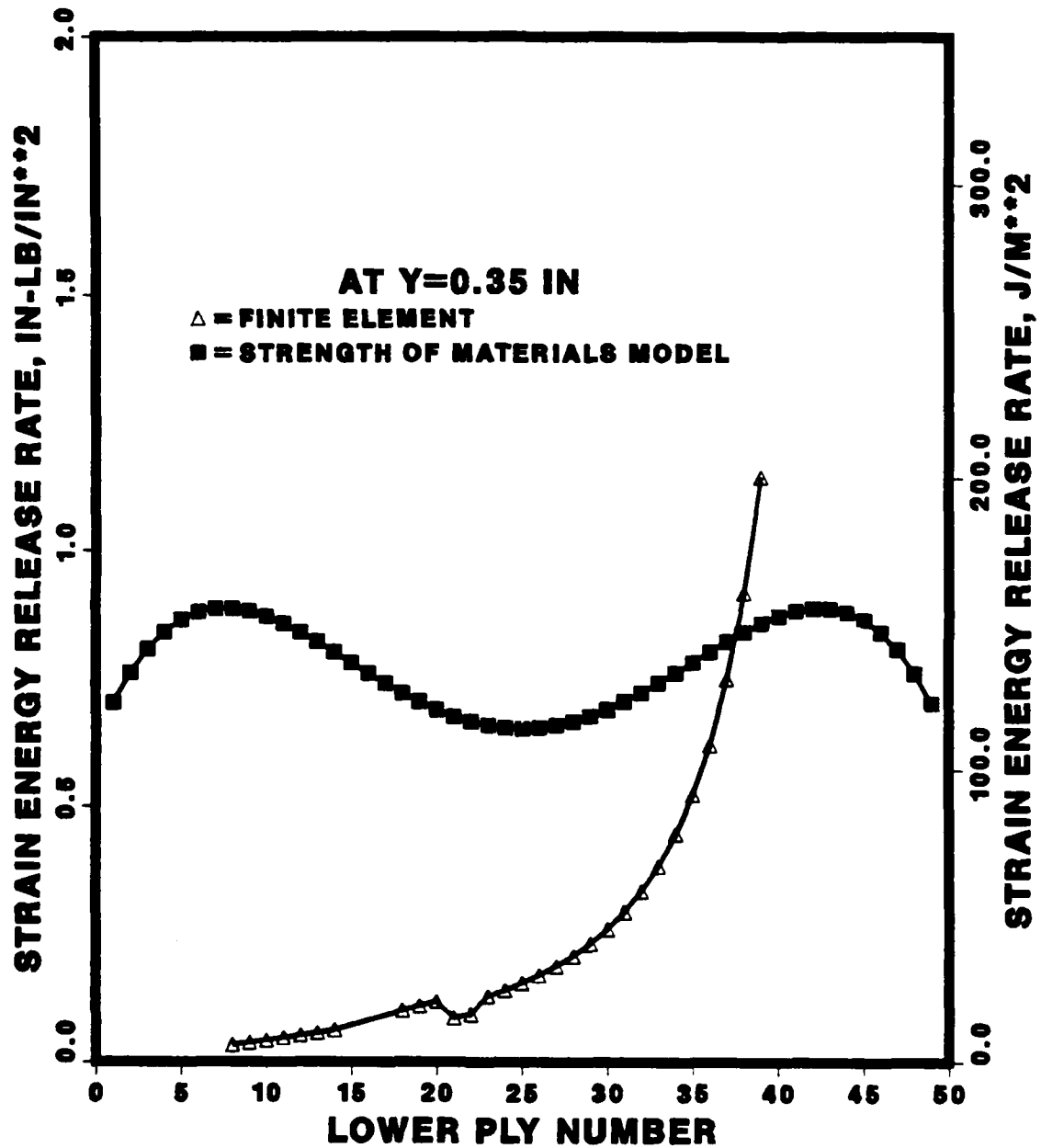


Figure 38. Strain energy release rate comparison for a unidirectional beam, using strength of materials model

using classical beam theory.

Figures 17, 18 and 19, along with Figures 43, 44 and 45, emphasize the degree to which the flaw changes the stress state in the beam. In Figures 43, 44 and 45, a crack has been added 14 interfaces above the midplane. The crack is located at approximately  $z = 0.07$  inches, and runs from  $-0.35$  inches  $\leq y \leq 0.35$  inches. A large discrepancy in the stress field near the crack tip would be expected. As Figure 44 shows, this is the case for the peel stress. However, Figures 43 and 45 show a greatly increased level of stress exists in a much larger region above the crack ( $z \geq 0.07$  inches,  $-0.35$  inches  $\leq y \leq 0.35$  inches). Stresses in the remainder of the beam are much smaller than in this region. Figure 43 even shows some tensile chordwise stresses above the midplane of the beam. In view of this radical change in the stress state, the applicability of a beam theory solution is called into question. Modelling the effect of the contact stress field is a logical next step.

Figures 46 and 47 show the examples of Figures 37 and 38, using only the contact stress contribution. While the steepness of the curve near the load nose causes significant errors in  $G$  at a given lower ply number, the trend is captured.

Figure 48 shows a comparison of finite element data and contact stress method data for a quasi-isotropic beam with a centered flaw of length 0.14 inches. This places the crack tips near the load nose stress concentration, for assumed flaws above the midplane. The model predicts the strain energy release rate values well. In view of the model's assumption of a flaw that dramatically alters the stress state throughout the specimen, its effectiveness for a smaller flaw is surprising.

The accuracy of this model is remarkable, given the simplifying assumptions behind it. The model neglects bending stresses entirely, assumes that all chordwise stresses below the crack are negligible, and applies the contact stress solution for a semi-infinite medium to sections with depth to span ratio of 0.22. This indicates that there is considerable room for refinement of the model, although the tradeoff between increased accuracy and increased complexity is difficult to judge.

It should be noted that neither model reproduces the jaggedness of the strain

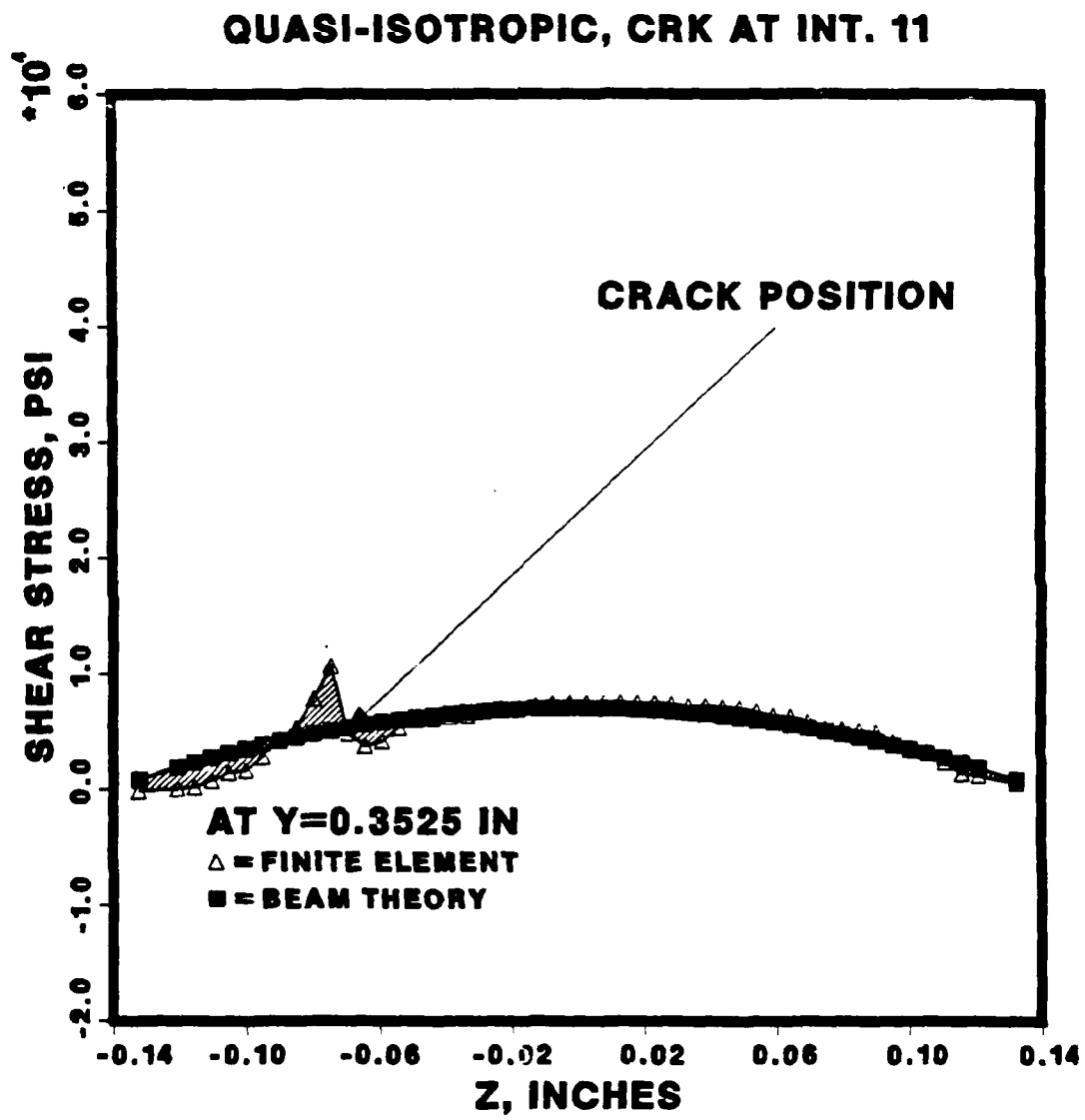


Figure 39. Shear stress distribution near crack tip,  
crack located 14 interfaces below midplane

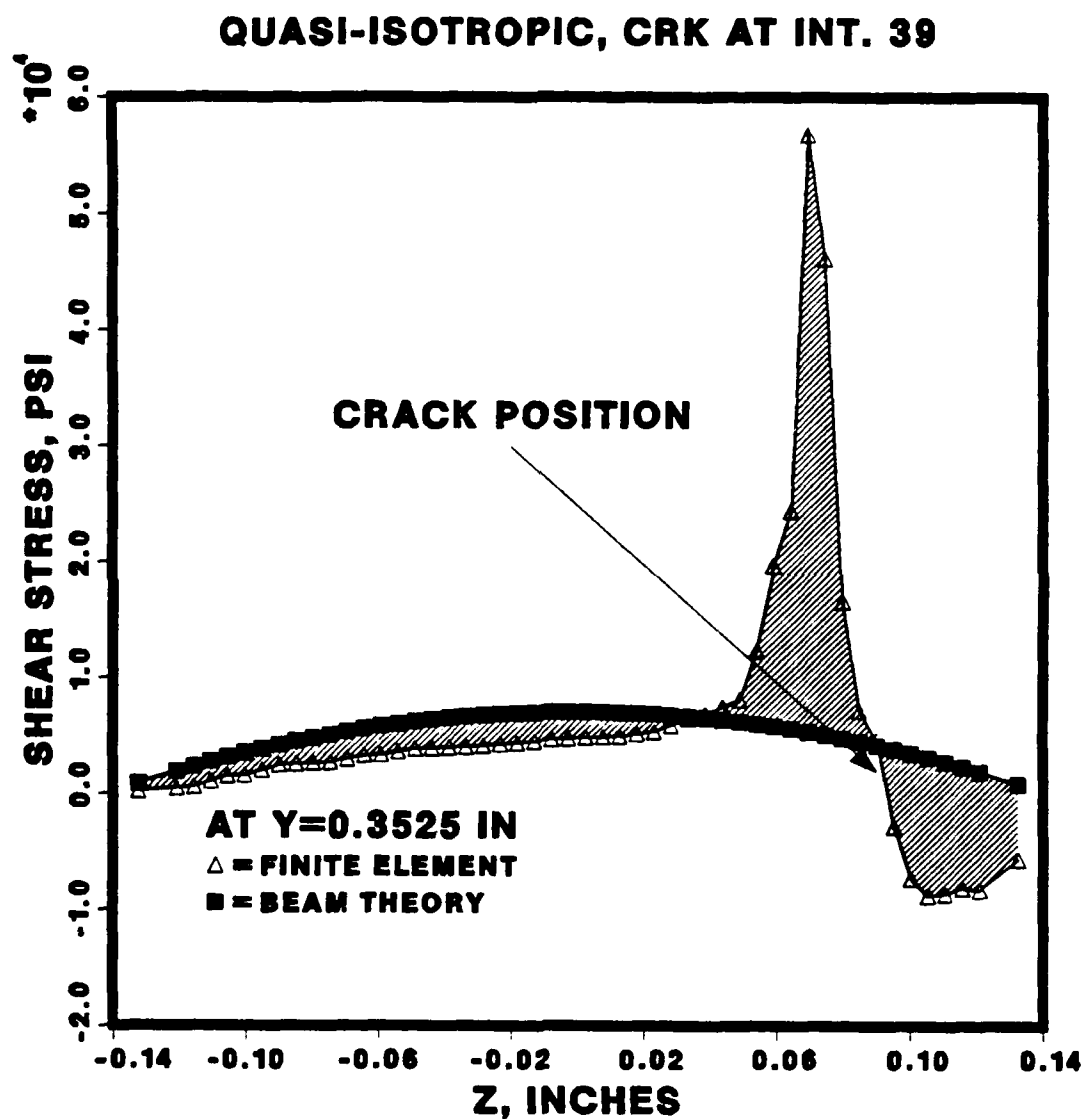


Figure 40. Shear stress distribution near crack tip,  
crack located 14 interfaces above midplane



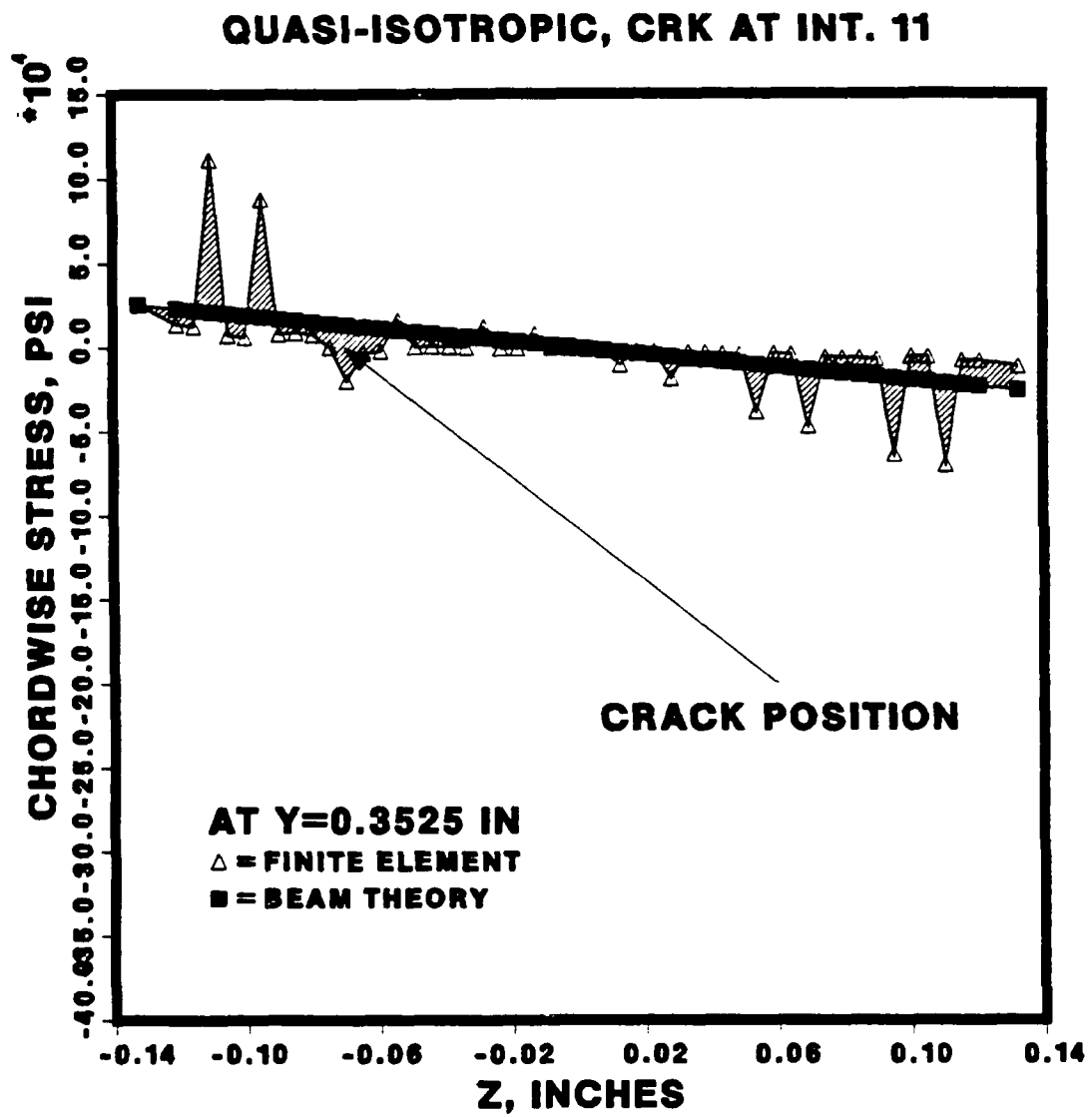


Figure 41. Chordwise stress distribution near crack tip,  
crack located 14 interfaces below midplane

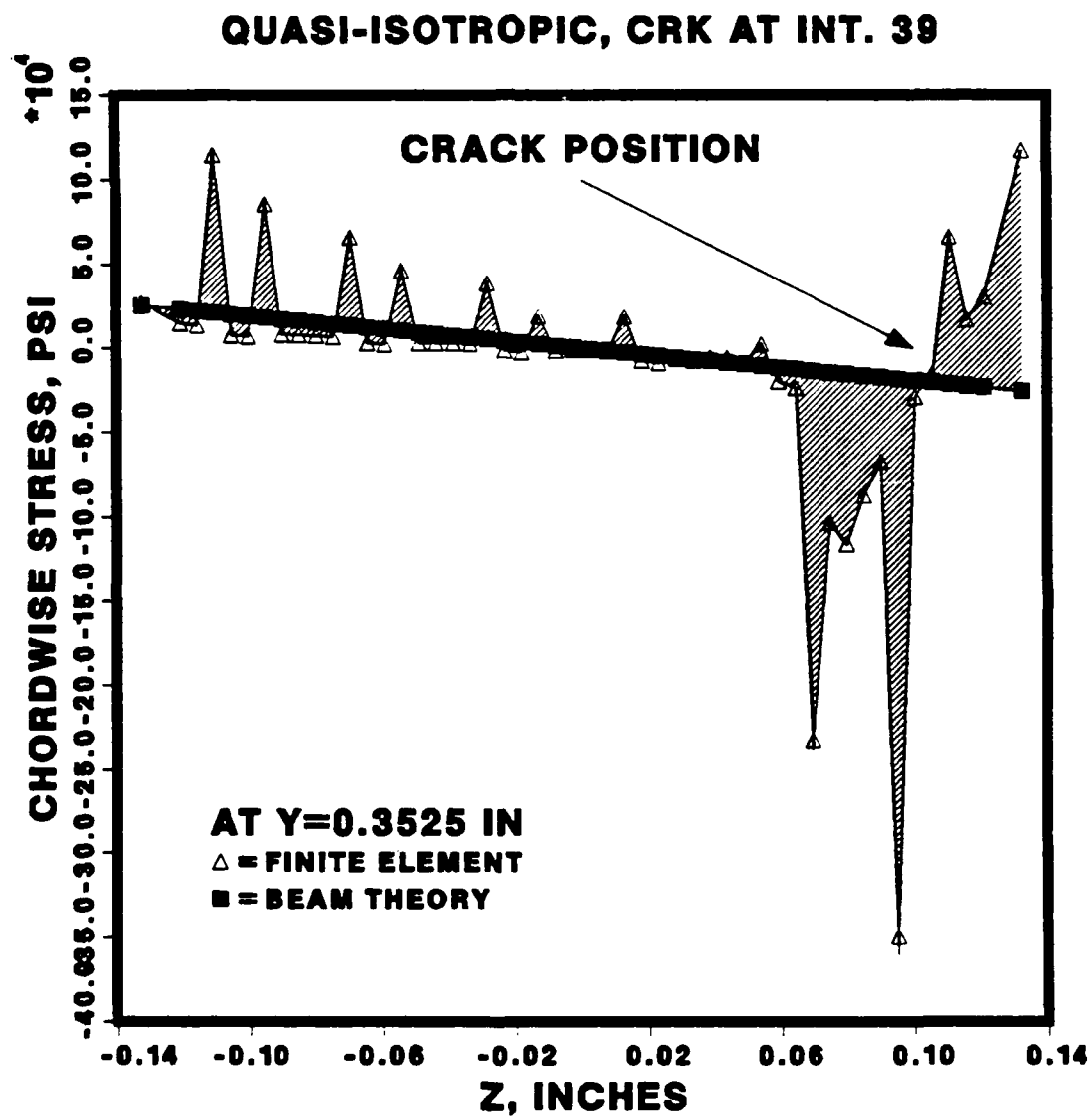


Figure 42. Chordwise stress distribution near crack tip,  
crack located 14 interfaces above midplane

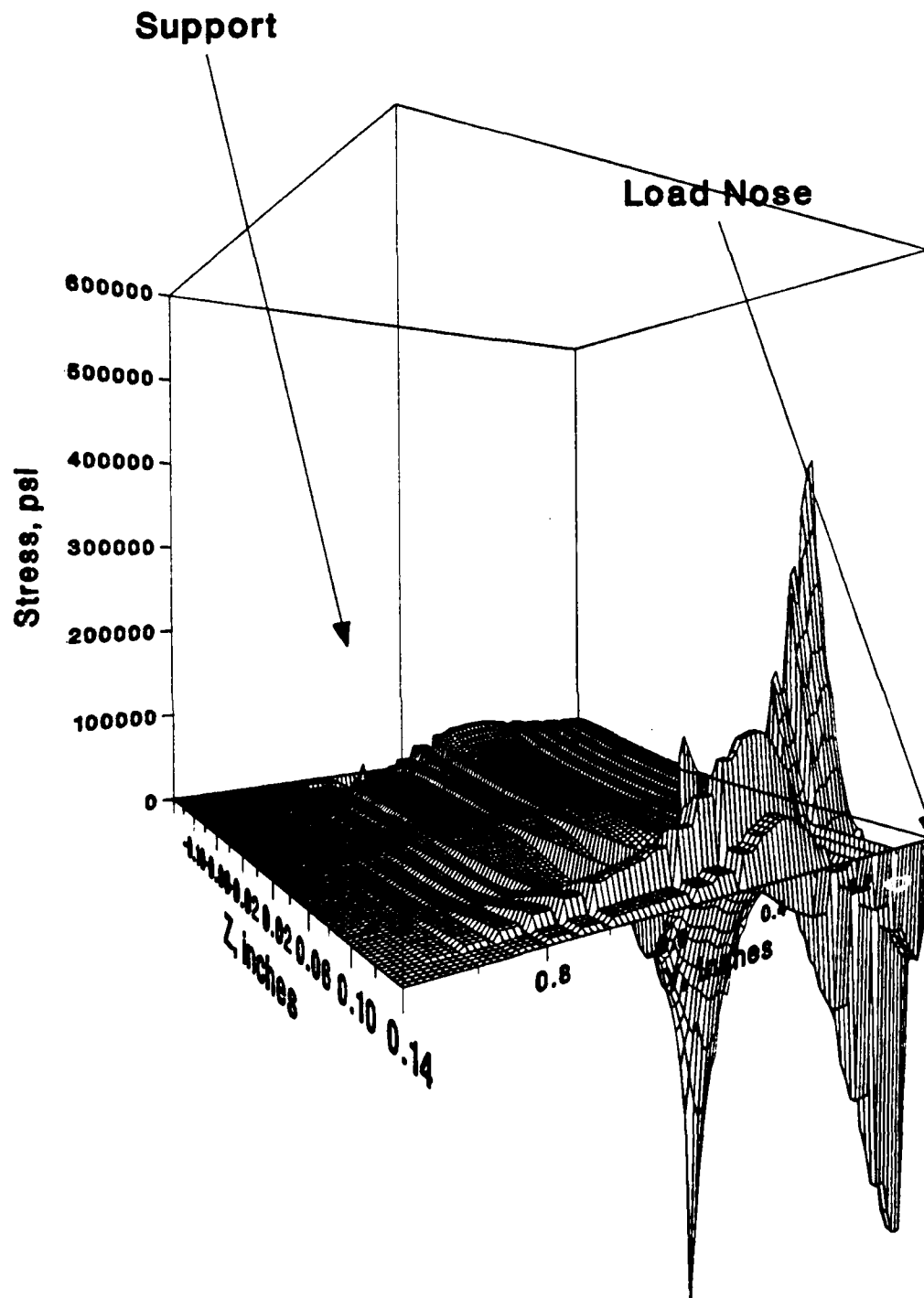


Figure 43. Chordwise stress map of cracked specimen

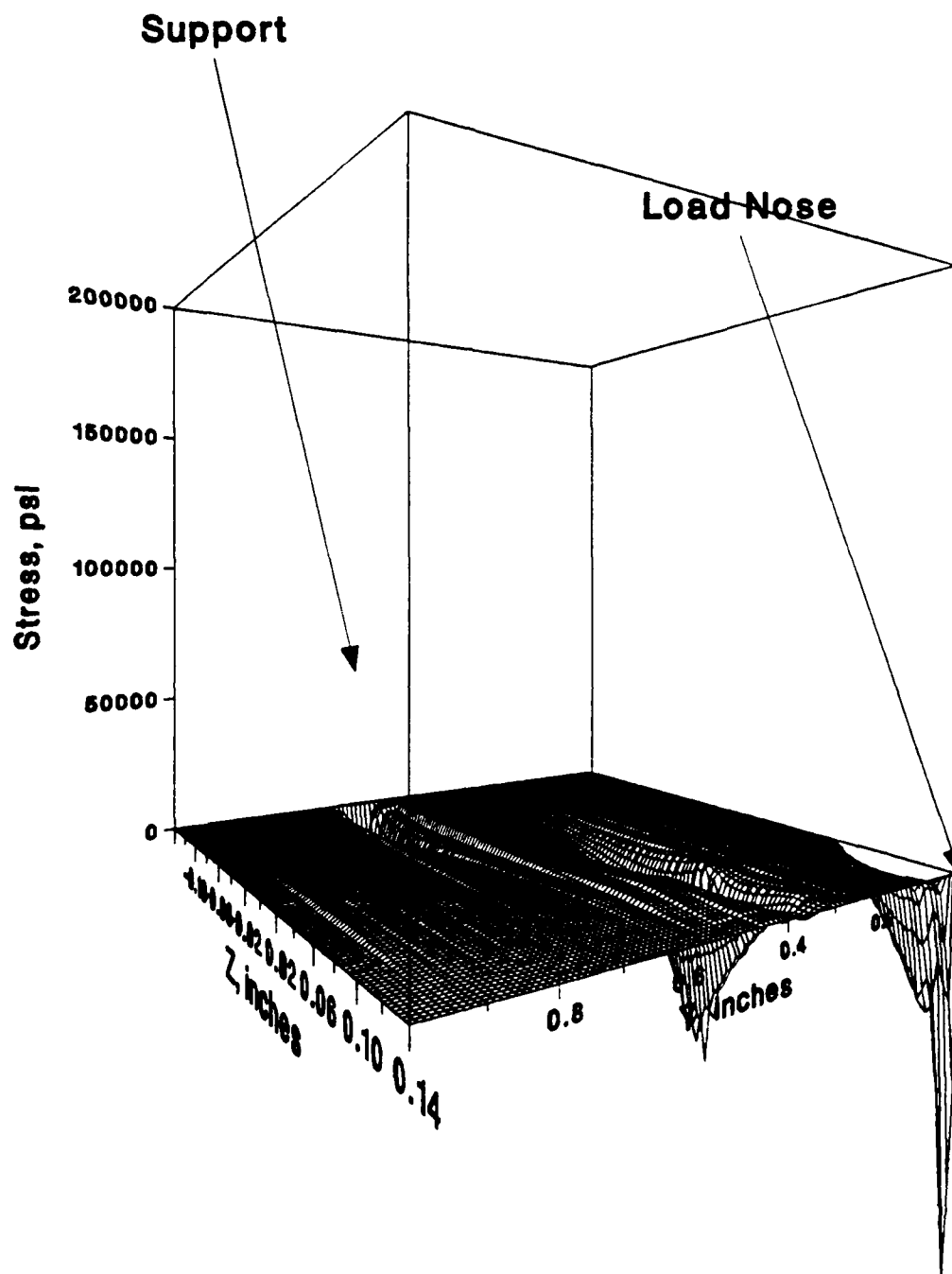


Figure 44. Peel stress map of cracked specimen

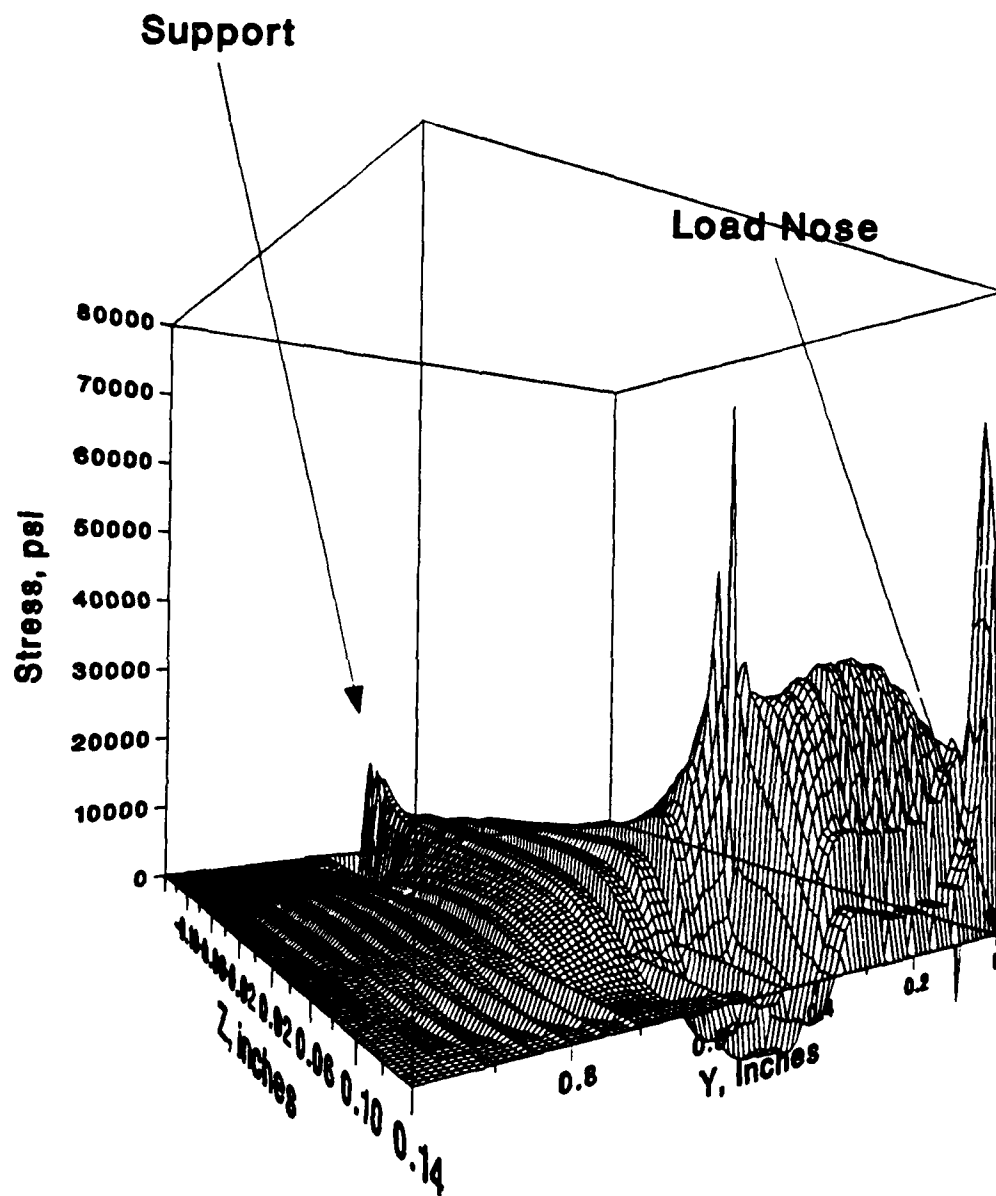


Figure 45. Shear stress map of cracked specimen

# QUASI-ISOTROPIC SHORT BEAM, 1 KIP

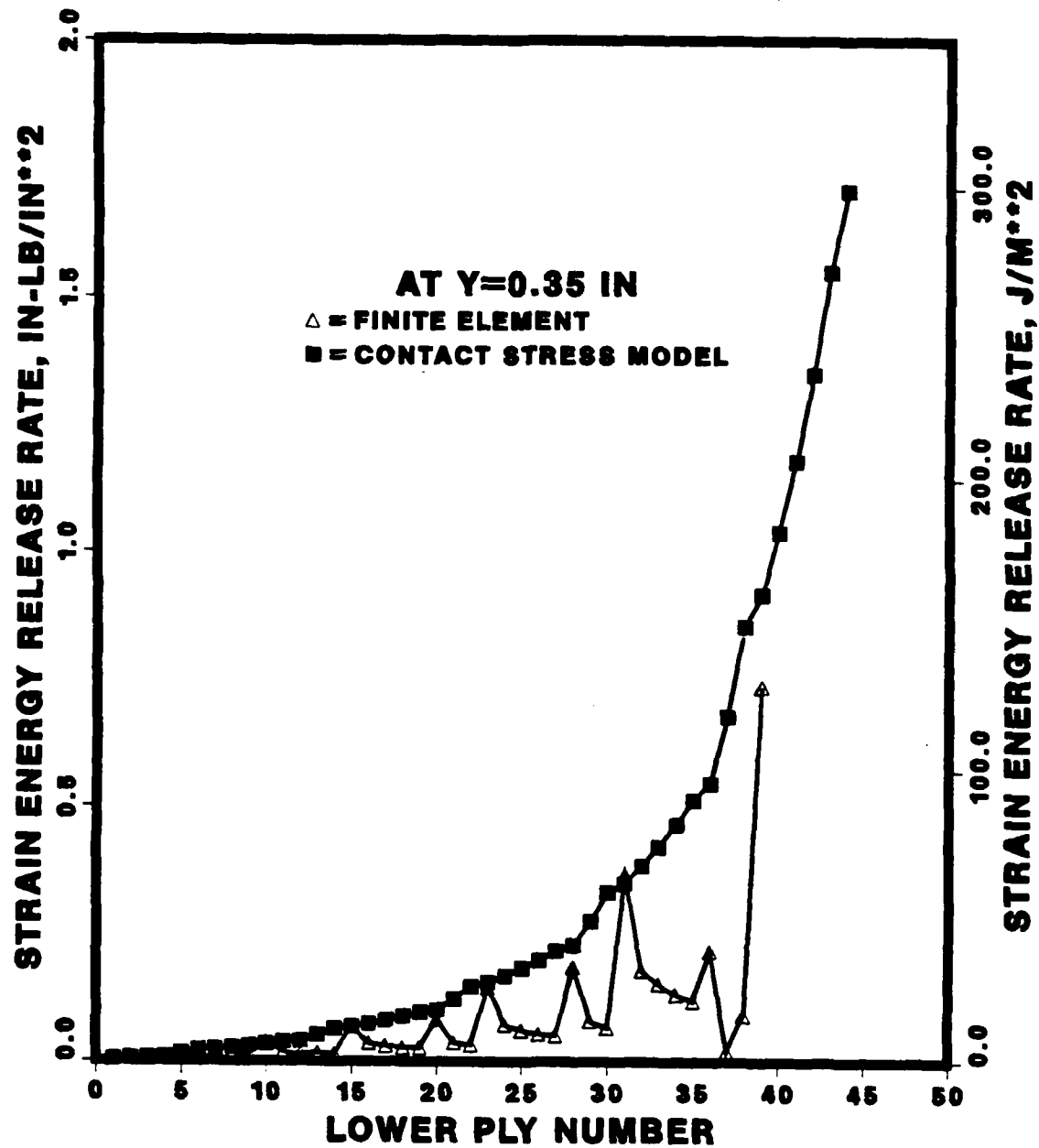


Figure 46. Strain energy release rate comparison for a quasi-isotropic beam, using contact stress model

# UNIDIRECTIONAL SHORT BEAM, 1 KIP

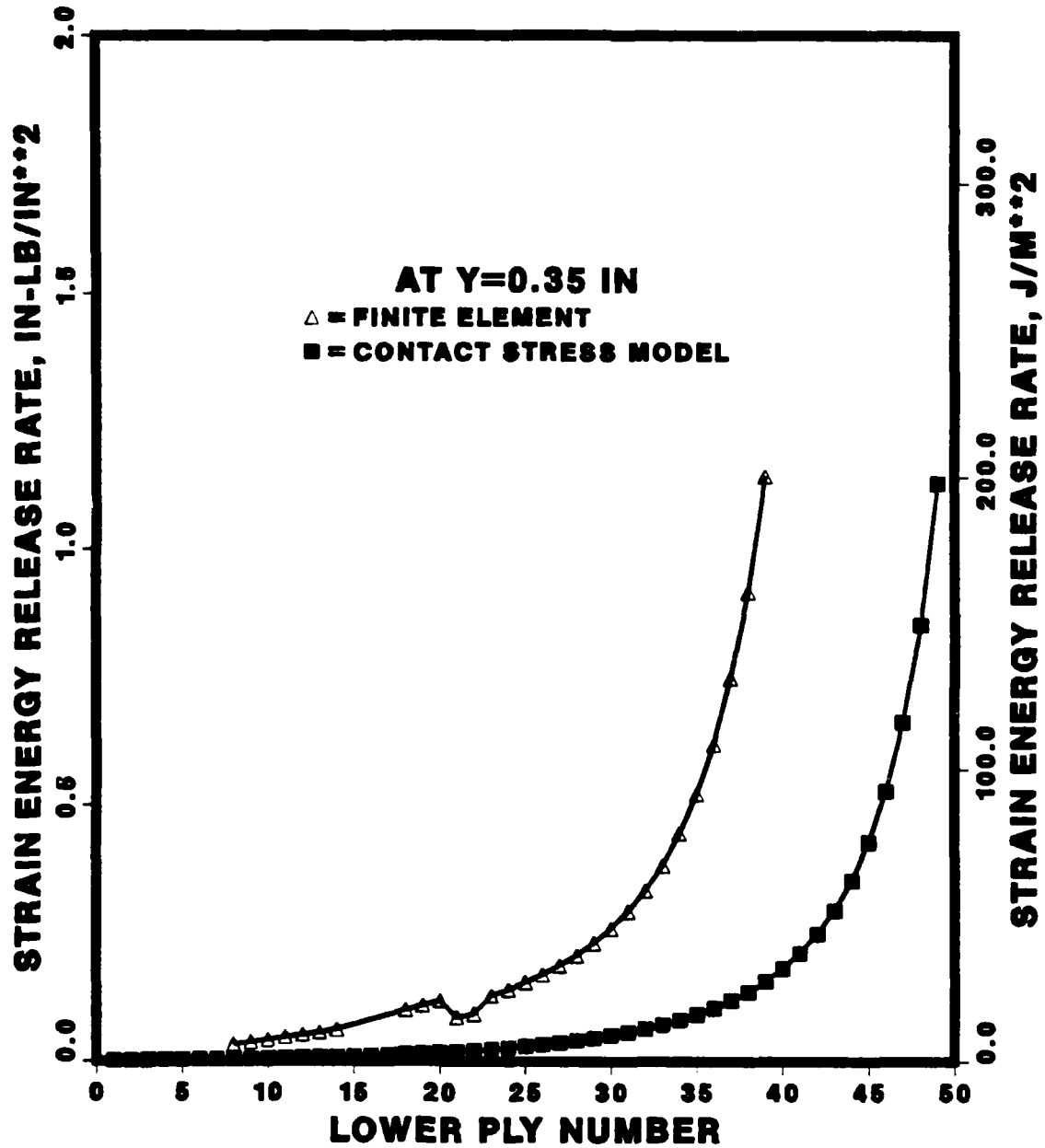


Figure 47. Strain energy release rate comparison for a unidirectional beam, using contact stress model

# QUASI-ISOTROPIC SHORT BEAM, 1 KIP

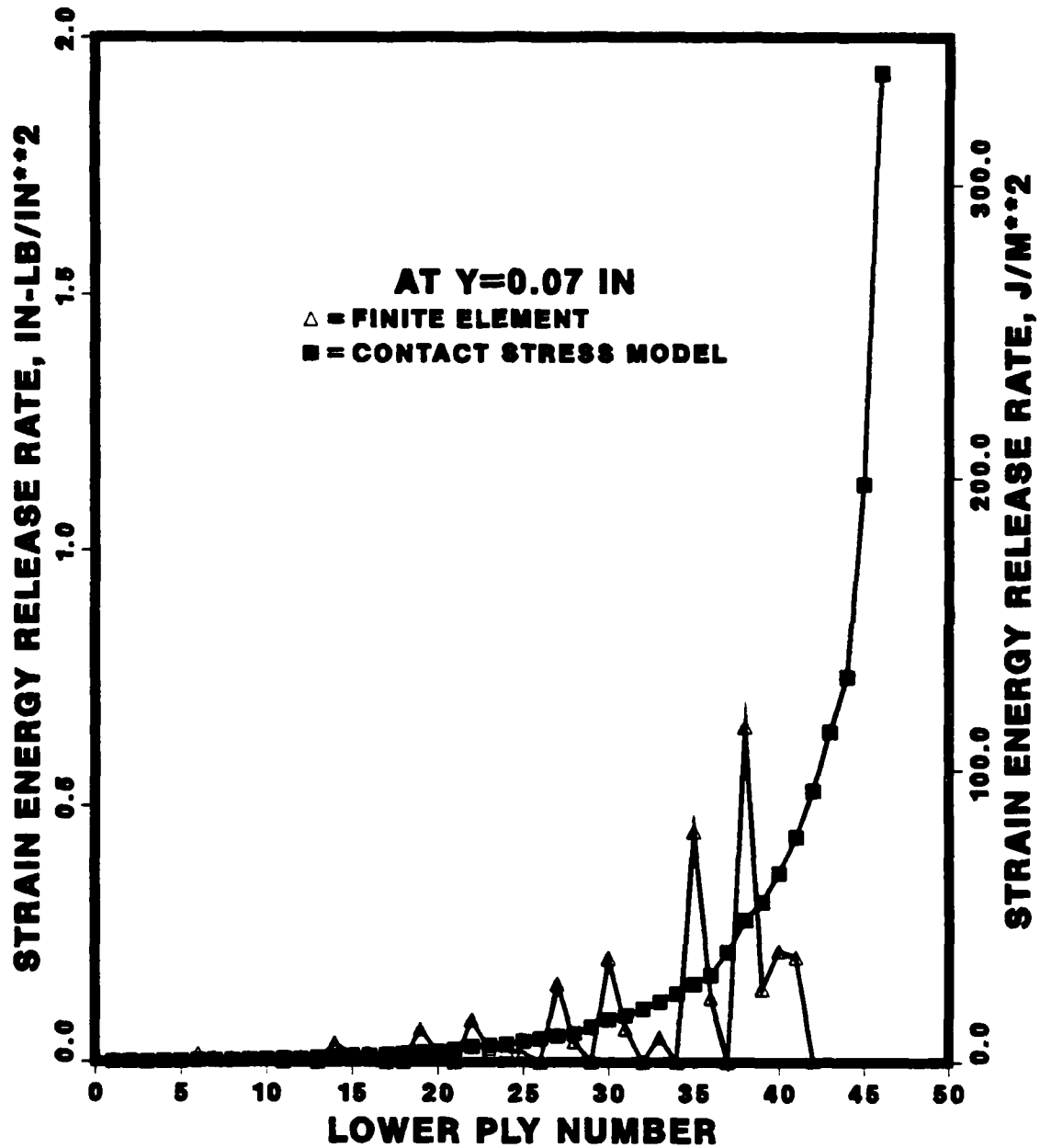


Figure 48. Strain energy release rate comparison for a quasi-isotropic beam, using contact stress model



energy release rate curves. This is due to the smearing of the laminate properties above and below the crack. This smearing leads to a distortion of the conditions along the plane of the crack, where the properties of the two plies being separated are distinct. The finite element analysis, which models the beam properties on a ply-by-ply basis, would be more accurate.

An important consideration in judging this method is its ease and economy of use. As an illustration, consider the plot shown in Figure 48. To obtain the finite element data for this plot, input data files totalling over 300 kilobytes of information had to be constructed, and approximately 28,000 CPU seconds of computation, on a Control Data Corporation Cyber 180-990 computer, was required to obtain the strain energy release rate information. By comparison, the data from the analytical model was computed using less than 9 CPU seconds for computation. One input file, containing less than one kilobyte of information, was required. The value of this method for obtaining quick, approximate solutions is clear.

#### **4.4. Conclusions**

Two strain energy release rate models for laminated composite beams under three-point loading have been developed. The first assumes that bending stresses provide the crack driving force, while the second assumes that contact stresses drive crack growth. The second model is seen to correlate more closely with the predictions of the finite element analysis. The contact stress model explains the tendency of the strain energy release rate to increase as the crack is moved closer to the top surface of the laminate, a tendency incompatible with a strength of materials model. The model is accurate enough to provide the designer with an estimate of the magnitude and trend of the strain energy release rates in a beam, quickly and easily, which ideally suits a preliminary design calculation. While additional testing on other variations of the three-point bend configuration is necessary, this method has promise for providing simple strain energy release rate models for other similar

configurations.

#### 4.5 Closing Remarks

The purpose of the work in this chapter has been to provide better understanding of the fracture behavior of a quasi-isotropic short-beam three-point bend configuration by constructing an appropriate strain energy release rate model, in light of the results of Chapter III. Two basic facts have been established by this work. First, the specimen is, from a fracture mechanics point of view, not a bending specimen at all. Rather, it is a contact stress specimen. This is established by the variation of the strain energy release rate parameter with the position of an assumed centered crack in the specimen. The second and more important finding is that the fracture behavior of the specimen is best described by a strain-to-failure approach. This is demonstrated by the more accurate predictions of the modes and locations of failure. Furthermore, the strain to failure approach provides information as to the causes of failure at each location on the specimen.

**CHAPTER V:**

**FRACTOGRAPHY OF THE CRACKED LAP SHEAR  
CONFIGURATION**

**5.1 INTRODUCTION**

In-depth description of composite failure requires knowledge of the material behavior near the tip of the propagating crack. Because of the high stress gradients and influence of plasticity in this region, in addition to its small size, analytical and numerical descriptions of crack-tip behavior can be intractable and unreliable. Qualitative and sometimes quantitative knowledge can be gained by examination of the fracture surfaces of failed specimens. Microscopy permits examination of extremely small regions of the fracture surface in isolation from the rest of the specimen, permitting close study of the crack tip region, as well as other features that may provide links between material properties and mechanical behavior.

The fractographic component of this research can be divided into the qualitative and the quantitative. In the former, the fracture surface is examined to determine the various damage modes that contributed to crack propagation. If the

significance of each of these morphologies is appreciated, the fracture surface provides a guide to the various fracture events that occurred during testing. In the latter, quantifiable characteristics of the fracture surface are identified, and their values tracked throughout the growth of the crack, in order to define the state of the crack tip as a function of crack length. This is necessary if observed fracture morphology is to be linked to periods of stable crack growth, unstable crack growth, and crack arrest observed during testing.

## **5.2 SPECIMEN CONFIGURATIONS AND TESTING**

Failed CLS specimens were provided from an ASTM round robin on this configuration. Three material systems were represented: the brittle-matrix systems AS4/B501-6 and AS4/BP907 graphite/epoxy, and the toughened-matrix system AS4/PEEK graphite/polyetheretherketone. Table 5 provides the dimensions for these specimens. All specimens were unidirectional, with the fibers running in the loading direction. All specimens were loaded in tension, with unloading and reloading as shown previously in Figure 7.

Testing of AS4/B501-6 specimens was performed in-house, as part of the ASTM round-robin. Testing was performed on an MTS machine operated in displacement-control mode, using hydraulic wedge grips to hold the specimen. Specimens were ramp-loaded at a crosshead speed of 0.05 inches per minute, until crack propagation and arrest was observed. This propagation was detected visually and by the resulting drop in the load. Crack propagation was monitored by painting the edges of the specimen with typewriter correction fluid. Two travelling microscopes were used to monitor crack length, one microscope for each edge. The length of the crack at each edge was recorded after each propagation and arrest. Use of two microscopes was especially important, because, as Armanios and Rehfield<sup>[40]</sup> have documented, the crack front generally is not straight, due to the existence of a triaxial stress

**TABLE 5: TYPICAL DATA FOR CLS SPECIMENS**

	AS4/B501-6	AS4/BP907	AS4/PEEK
WIDTH, INCHES	1.00	1.00	1.00
STRAP THICKNESS, INCHES	0.039	0.065	0.140
LAP THICKNESS, INCHES	0.020	0.035	0.070
$E_{11}$ , psi	$20.2 \times 10^6$	$17.59 \times 10^6$	$18.71 \times 10^6$

state near the edges of the specimen. In fact, as shown in Figure 49, the crack front tends to curve forward near the edges. The figure illustrates the fringes on a layer of photoelastic material laid over a DCLS specimen with a quasi-isotropic layup.

Three AS4/PEEK specimens were also tested in-house. These specimens were known as P5, P11, and P13. Because PEEK is a tough resin, it was necessary to precrack these specimens prior to tensile testing. The precracking was begun on an MTS machine operating in haversine mode under load control, with a maximum load of 3000 pounds, a minimum load of 300 pounds ( $R = 0.1$ ), and a pressure of 1500 pounds in the hydraulic grips. Photoelastic material was attached to the face of the lap region of each specimen, in hopes of monitoring the shape of the crack during testing, but no fringes were observed in the photoelastic layer. Some experimentation was required before the cracks propagated to sufficient lengths; Table 6 documents the load history of each specimen during precracking.

With the precracking complete, the specimens were tested in tension on an Instron machine, using Instron wedge grips. Grip slippage was retarded by placing coarse (AA-80) sandpaper between the specimen and the grips. Crack growth was measured using typewriter correction fluid and travelling microscopes, as with the AS4/B501-6 specimens.

The remaining specimens were tested by other agencies as part of the ASTM round-robin. A total of six additional AS4/PEEK specimens and 6 additional AS4/BP907 specimens were tested. The failed specimens and their test data were supplied by W.S. Johnson<sup>[52,53]</sup>.

A total of four AS4 B501-6 specimens were tested; they shall be known as specimens A, B, C, and D. All of the AS4 B501-6 specimens failed by delamination, except for specimen B. This specimen failed by splitting along a line parallel to the loading axis, because it was approximately 1 mm wider than the hydraulic grips. The difference in deflection of the loaded portion of the specimen and the unloaded region outside the grips produced splitting failure at a low load level. Table 7 shows the maximum loads and the mean crack lengths for each crack arrest observed in

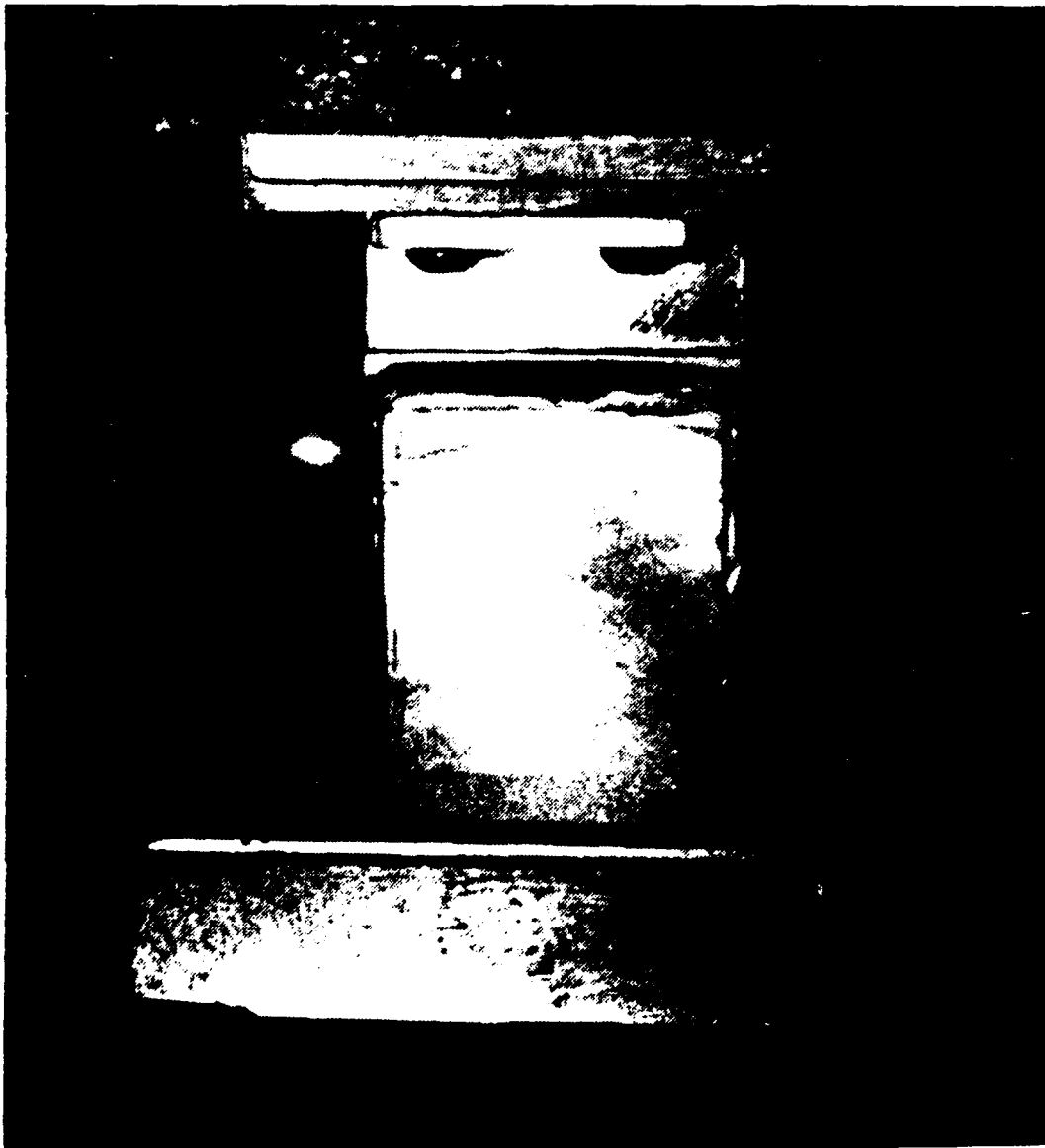


Figure 49: Non-straight crack front in the  
double cracked lap shear specimen<sup>[40]</sup>

**TABLE 6: PRECRACKING HISTORIES OF  
PEEK SPECIMENS, IN CHRONOLOGICAL ORDER**

SPECIMEN #	MAX LOAD, LBS	MIN LOAD, LBS	GRIP LOAD,LBS	FREQ, HERTZ	CYCLES
5	3000	300	1500	not recorded	102,630
	3000	1500	1500	10	10,000
	4000	2000	1500	10	2200
	4000	2000	1800	10	1200
	4000	2000	2500	10	212,600
	4000	400	2500	10	27,600
11	4000	2000	2500	10	163,000
	4000	400	2500	10	64,900
13	4000	400	2500	10	18,600



these specimens.

The PEEK specimens tested in-house cracked and failed in the expected manner. Maximum load values and mean crack lengths for these specimens are given in Table 8.

Maximum load and mean crack length data from the remaining specimens, as provided by W.S. Johnson<sup>[52,53]</sup>, are shown in Tables 9 and 10. The prefix *GD* denotes specimens tested by General Dynamics, and the prefix *L* denotes specimens tested by Lockheed.

### 5.3 QUANTITATIVE FRACTOGRAPHY

#### AND STATISTICAL ANALYSIS

##### 5.3.1 Point Counting

One common way of quantifying a surface viewed through a microscope is known as *point counting*. Figure 50 illustrates this concept. The experimenter considers a surface as being made up of a number of different regions (*e.g.*, fracture morphologies, metallurgical phases, or various materials), each of which can be identified by sight. The task is to determine the fraction of the surface that is made up of each of these regions. The surface is viewed through the microscope, and a grid is superimposed upon the image; this is done by the use of a special objective lens on an optical microscope, or by the placing of a transparency on the viewing screen of a scanning electron microscope (SEM). The nodes of the grid shown in Figure 50 define 16 points. The experimenter determines how many of these 16 points lie in each of the different regions. If  $N$  points are seen to lie within a given type of region, the area fraction of that region is  $N/16$ . The microscope's field of view is then moved randomly, if the task is to obtain area fractions for the overall

**TABLE 7: LOCATIONS AND LOADS  
OF CRACK ARRESTS, AS4 B501-6 SPECIMENS**

	LOAD, KG	MEAN CRACK LENGTH, CM
SPECIMEN A	452	1.83
	814	2.44
	848	3.87
SPECIMEN B	402	1.72
	824	2.00

**TABLE 8: LOCATIONS AND LOADS  
OF CRACK ARRESTS, IN-HOUSE PEEK SPECIMENS**

	LOAD, LBS	MEAN CRACK LENGTH, INCHES
SPECIMEN 5	6400	1.288
	7500	1.331
	7600	1.437
	7600	1.510
	7400	3.475
	7600	3.870
	7600	4.395
	7800	5.189
SPECIMEN 11	7600	5.592
	6600	1.171
	8000	1.220
SPECIMEN 13	9200	1.265
	6600	1.233
	9000	1.293

**TABLE 9: LOCATIONS AND LOADS  
OF CRACK ARRESTS, AS4/BP907 SPECIMENS**

	LOAD, LBS	MEAN CRACK LENGTH, INCHES
SPECIMEN GD-7	3725	2.98
	3950	3.55
	3955	3.76
	3990	3.92
	4125	4.07
SPECIMEN GD-8	3505	1.95
	3560	2.40
	3800	3.01
	3860	3.60
	3990	4.42
	4100	5.33
SPECIMEN GD-9	2985	1.99
	3040	2.09
	3300	2.28
	3340	2.59
	3400	3.30
	3725	3.58
	3650	4.06
	3750	5.23
SPECIMEN L-4	4080	0.06
	3910	1.12
	3725	1.41
	3800	1.72
	3900	1.90
SPECIMEN L-5	3825	2.15
	3850	2.38
	3975	2.61
	3800	3.61
	3850	3.90
SPECIMEN L-6	failed immediately	4.57

**TABLE 10: LOCATIONS AND LOADS  
OF CRACK ARRESTS, AS4/PEEK SPECIMENS**

	LOAD, LBS	MEAN CRACK LENGTH, INCHES
SPECIMEN GD-1	failed immediately	
SPECIMEN GD-2	9170 8950 9000 8800	2.22 2.45 2.76 3.00
SPECIMEN GD-3	failed immediately	
SPECIMEN L-8	failed during precracking	
SPECIMEN L-9	9150 9100 8900 failure	0.02 0.18 0.68 5.68
SPECIMEN L-10	8750 8700 8600	0.26 0.86 1.70

surface, or in a predetermined pattern, if the task is to determine area fraction as a function of position. After enough fields of view have been examined, the resulting average area fractions can be considered as representative of the entire surface.

Figure 51 illustrates the approach taken in this effort. Holding the position of the field of view constant in the direction of crack propagation, several non-overlapping fields of view are examined across the width of the fracture surface. The average values of the area fractions of various fracture morphologies from the fields of view are considered to describe the fracture surface at this particular crack length. The position in the crack growth direction is then incremented, and the procedure repeated until the entire fracture surface has been characterized.

### 5.3.2 Statistical Approach

For each given fracture morphology, the fields of view at each crack length can be used in statistical comparisons of adjacent crack positions. Hypothesis testing can be used objectively to accept or reject such statements as, "There is significantly more interface fracture at 2mm of crack growth than at 4mm of crack growth." The appropriate hypothesis test is the Mann-Whitney U-test, a non-parametric rank sum test described in Reference 54. Each number in the two data sets is assigned an integer rank  $R$ , the largest number having rank 1. These ranks can then be used to calculate a normally-distributed  $Z$ -statistic:

$$Z = \frac{1}{\sigma_U} \left[ n_1 n_2 + \frac{n_1 (n_1 + 1)}{2} - R_1 - \mu_U \right] \quad (80)$$

where

$n_1, n_2$  are the numbers of fields of view in the two samples, each sample being associated with a particular crack length

$R_1$  is the sum of the ranks in the first sample

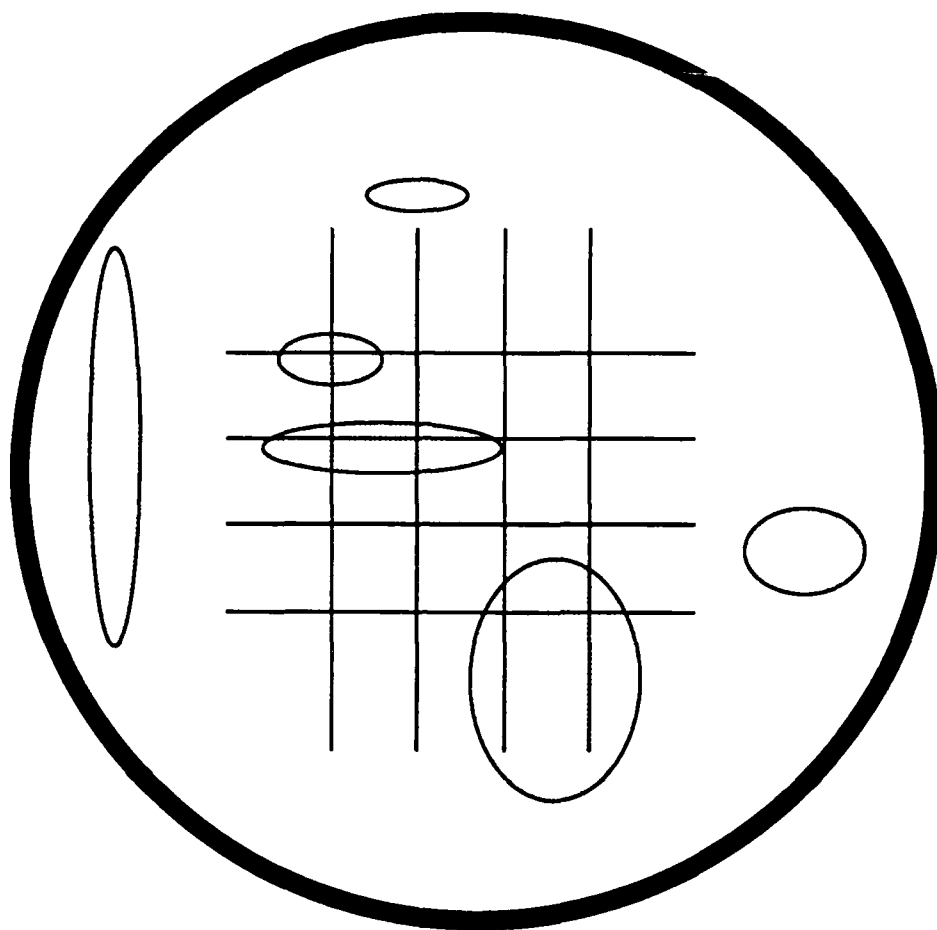


Figure 50: Schematic of point counting

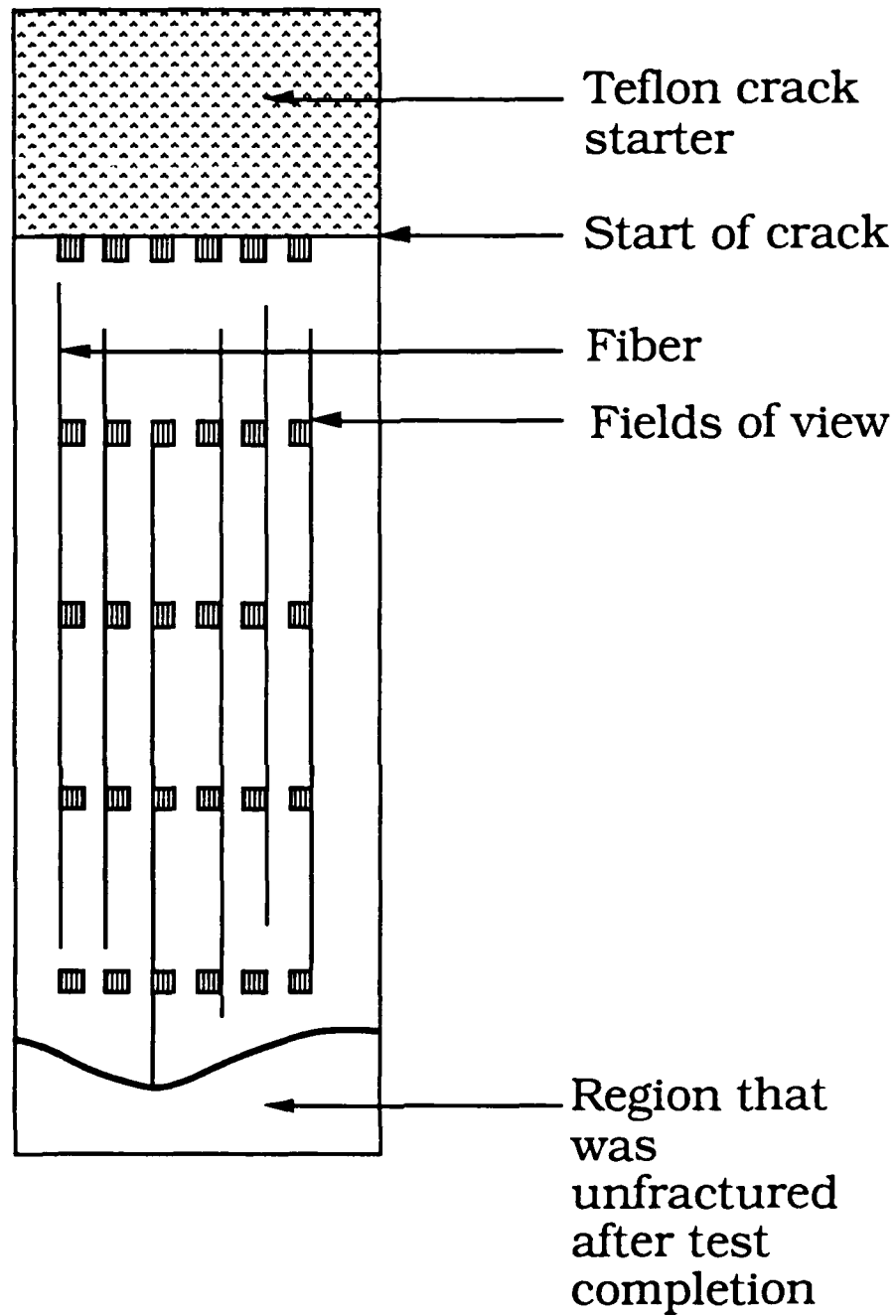


Figure 51: Point-count marching

$\mu_U$  is the mean of the  $Z$ -statistic

$\sigma_U$  is the standard deviation of the  $Z$ -statistic

The mean and the standard deviation of the  $Z$ -statistic are given by

$$\mu_U = \frac{n_1 n_2}{2} \quad (81)$$

$$\sigma_U = \sqrt{\frac{n_1 n_2 (n_1 + n_2 + 1)}{12}} \quad (82)$$

The Mann-Whitney U-test can be applied to samples of population greater than eight; while it was not always possible to find 50 acceptable fields of view at a given crack length, the number never went below 30, and this is still well within the acceptable range. Furthermore, the Mann-Whitney U-test requires no assumptions about the distribution of the data. This is important because the data to be compared in the current effort were, by inspection, not normally distributed.

However, the U-test, as described above, does not explain what to do if some numbers in the first data set are equal to some numbers in the second data set. Since there are only 17 numbers (including zero) that can appear in each 50-point data set, this situation can be expected to occur often. Reference 54 suggests "averaging out" the ties. For example, if there is a five-way tie for the fifth-largest number, each of the tied numbers would be assigned the same rank, calculated as:

$$\text{rank} = \frac{5 + 6 + 7 + 8 + 9}{5} = 7 \quad (83)$$

However, this is offered as an approximation for a relatively small number of ties, which cannot be assumed here. Gibbons<sup>[55]</sup> offers another method of calculating the  $Z$ -statistic, one that lends itself to more straightforward computer programming while dealing more accurately with ties. Let the first data set be represented as  $\{X_1, X_2, \dots, X_{n_1}\}$ , and let the second be  $\{Y_1, Y_2, \dots, Y_{n_2}\}$ . Then define



$$U_T = \sum_{i=1}^{n_1} \sum_{j=1}^{n_2} \mathcal{D}_{ij} \quad (84)$$

where

$$\mathcal{D}_{ij} = \begin{cases} 1 & \text{if } X_i > Y_j \\ 0 & \text{if } X_i = Y_j \\ -1 & \text{if } X_i < Y_j \end{cases} \quad (85)$$

Furthermore, let

$$\sigma_T = \sigma_U \sqrt{1 - \frac{\sum (t^3 - t)}{(n_1 + n_2)^3 - n_1 - n_2}} \quad (86)$$

$$\mu_T = 0 \quad (87)$$

where  $\sigma_U$  is as defined in equation (82),  $t$  is the multiplicity of a given tie, and the summation is taken over all sets of tied numbers. Then

$$\mathcal{Z} = \frac{(U_T - \mu_T)}{\sigma_T} = \left( \frac{U_T}{\sigma_T} \right) \quad (88)$$

Hypothesis tests were conducted at a 90% confidence level ( $|\mathcal{Z}| \geq 1.65$ ), a typical standard for comparisons of subjectively-evaluated data in which a large amount of variation is expected.

### **5.3.3 Specimen Preparation**

Specimen preparation for fractography was in accordance with usual procedures for composites. The failed specimens were not completely split, so it was necessary

to cut them open with a razor blade, after which they could be sectioned. Figure 52 shows how this sectioning was done, using a silicon carbide blade of width 0.015 inches. When calculating the distance from the crack starter, each cut was assumed to have removed 0.015 inches of material. One edge of each section of the specimen was marked with typewriter correction fluid, to permit later identification of the crack-growth direction. After sectioning and marking, the sections were attached to SEM stubs with silver paint, and the stubs were stored in boxes marked to indicate the location on the fracture surface from which each specimen was taken. The specimens were sputter-coated with a mixture of gold and palladium. Experimentation established that 11 minutes of coating led to good SEM images, without specimen charging or blurring of small features. It should be noted that the operating current on the sputter coater was well below the recommended 40 mA, even when the unit was being operated at the maximum recommended voltage of 1.2 kV. The total thickness of the coating can be estimated by the formula<sup>[56]</sup>

$$d = MA \times KV \times t_c \times k \quad (89)$$

where

$d$  is the coating thickness, in Angstroms

$MA$  is the current, in milliamperes

$KV$  is the voltage, in kilovolts

$t_c$  is the coating time, in minutes

$k$  is a constant with a value of 5 if the coating is done in an argon environment, and 2 if nitrogen or air is used

From this formula, the coating thickness was between 1100 Å and 1600 Å. The coating thickness recommended by Reference 56 for most materials is 300-500 Å, but specimens coated for shorter periods frequently exhibited charging in the microscope.

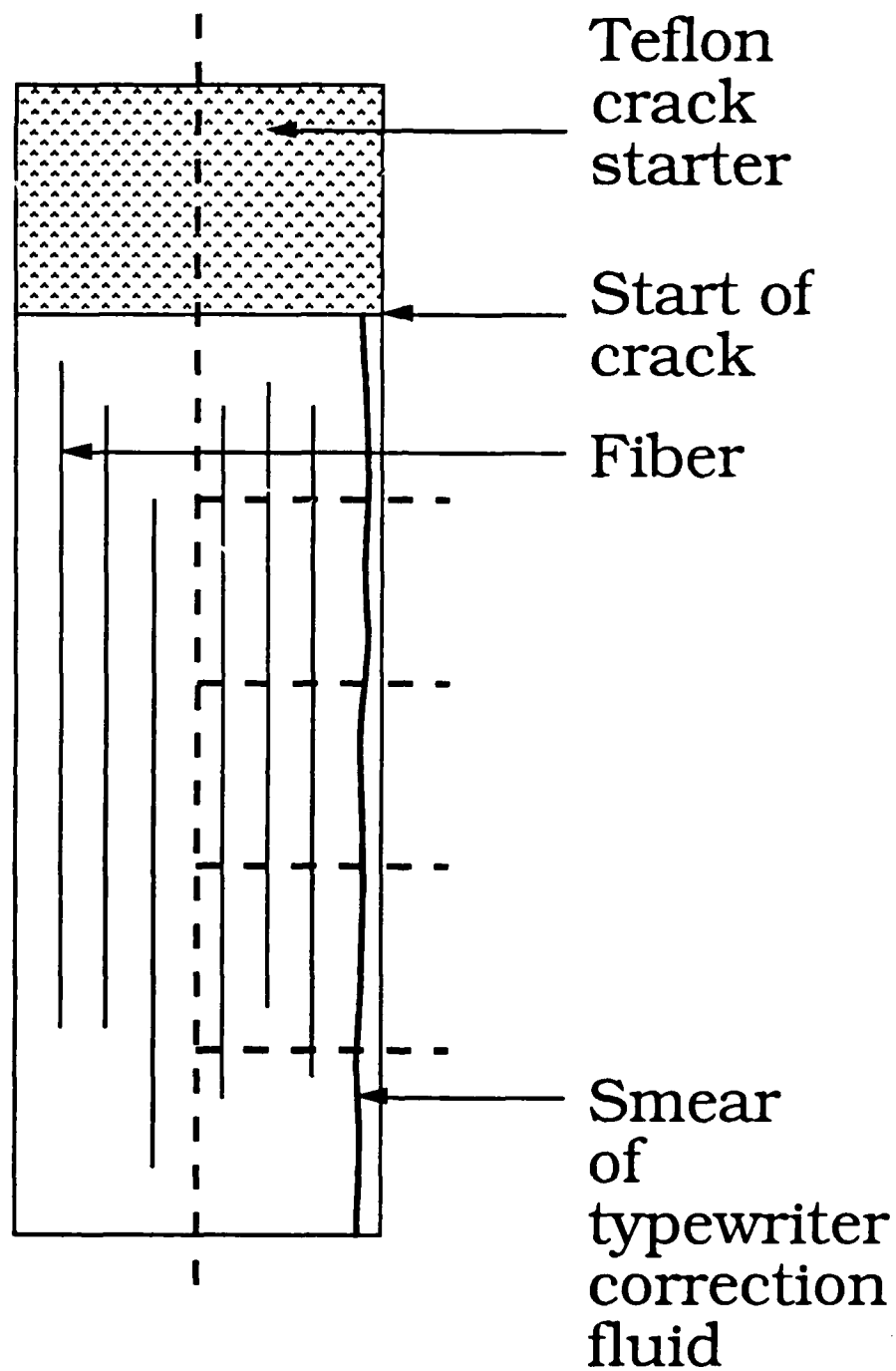


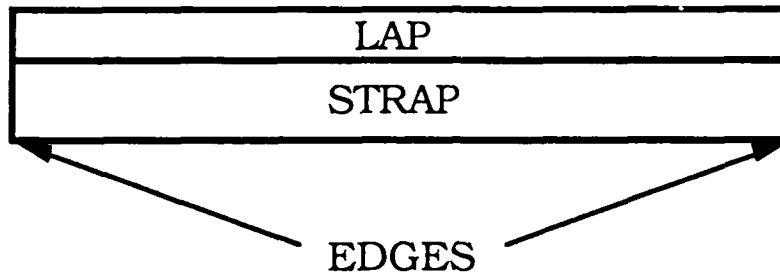
Figure 52: Specimen sectioning plan

The white-out that identified the crack growth direction also identified the edge of the specimen, where a triaxial state of stress predominates. Figure 53 shows why this difference in stress state arises. Due to Poisson effects, one section recedes more than the other at the edges, introducing a stress directed normal to the loading axis and in the plane of crack propagation. In the figure, the strap section is shown as undergoing the greater deformation. In the interior of the specimen, this stress is less significant, and the state of stress is approximately two-dimensional. In order to remove the need for three-dimensional analyses, data is best taken away from the specimen edges. Thus, all fields of view were taken at least 2 mm away from the edge. The fields of view were examined at magnifications that permitted the taking of at least 50 fields of view, including unsuccessful ones, at each location, while including in each field of view an area that was large enough to be varied, but small enough to be accurately point-counted. The field of view was marched parallel to the crack starter by steps that produced tightly-spaced but non-overlapping fields of view.

#### **5.3.4 Fractographic Approach**

The fracture surfaces of the failed specimens were divided into four morphologies: interface failure, shearing failure, matrix microcracking, and processing defects. Figure 54 shows examples of each of these morphologies. Interface failure was defined as separation of the matrix from the fiber surface. Shearing failure was a broadly-defined morphology, incorporating hackling and other shear-induced matrix failure. Matrix microcracking was a highly subjective category. Reference 40 indicates that microcracking in CLS and DCLS specimens is increased by the presence of off-angle plies, because the matrix bears a larger portion of the load in such plies. Thus, matrix microcracks are less likely in unidirectional laminates. Nonetheless, cracks normal to the loading axis were occasionally found, and their presence was noted in this category. Processing defects included all areas of the fail-

**(a)**



**(b)**

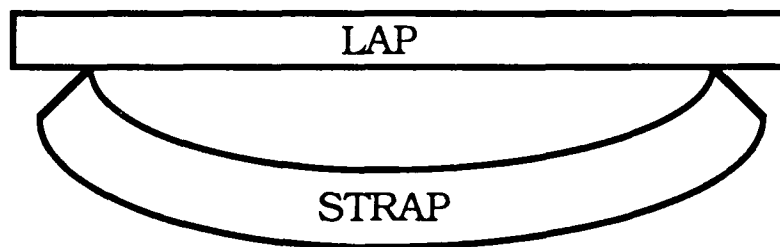


Figure 53: Triaxial stress state near edges of CLS specimens

(a) Undeformed (b) Under load

ure surface that included anomalies, such as processing voids and regions of excess matrix. Also in this category were areas where debris had fallen on the fracture surface during preparation.

Table 11 shows a typical data set, obtained from one specimen at a distance of 3.846 mm from the starter notch. The coordinate normal to the crack growth direction is  $Y$ . The number of grid points that lie on regions of interface failure is  $PPI$ ,  $PPS$  is the number on shearing failure regions,  $PPM$  is the number on or near matrix microcracks, and  $PPD$  is the number on defected regions. Note that

$$PPI + PPS + PPM + PPD = 16 \quad (90)$$

A brief FORTRAN program, called QSTATS, was written to perform statistical analyses on the data from each specimen. Data sets of the form of Table 11 were assembled in order of increasing distance from the crack starter notch. The QSTATS program calculated the means and the standard deviations of  $PPI$ ,  $PPS$ ,  $PPM$ , and  $PPD$  for each data set, and performed  $\chi^2$  tests, as described in Reference 57, to determine whether the data were normally distributed. Mann-Whitney U-tests were run on all adjacent data sets, and the values of  $Z$  calculated for each of the four damage modes.

Another choice of damage modes is possible. Yamashita, Hua, and Stumpff<sup>[57]</sup> have noted that Mode I failure of brittle matrix composites leads to smooth, glassy fracture surfaces and river patterns, as shown in Figure 55, while Mode II failure leads to the hackling and scalloping found in Figure 56. Tracking these two damage modes through the specimen offers the possibility of qualitative insights about

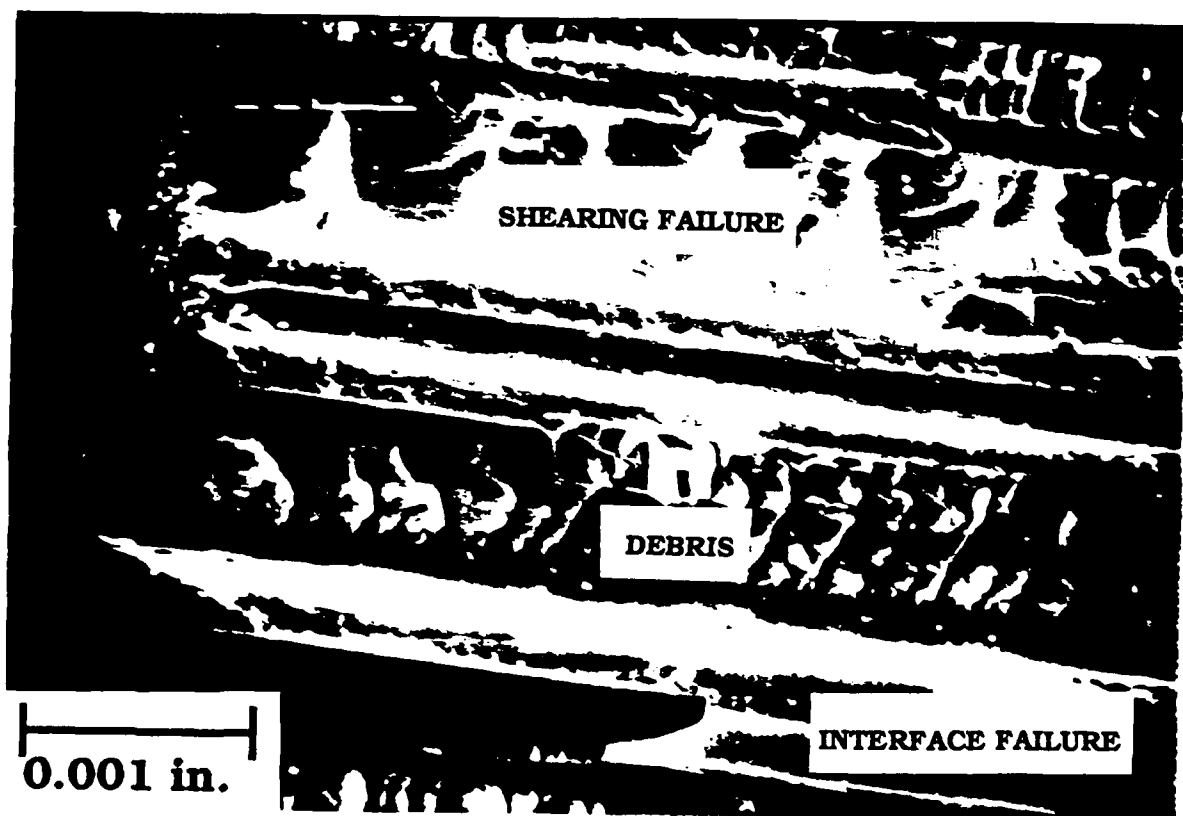


Figure 54: The four fracture modes

TABLE 11: SAMPLE POINT COUNT DATA SET, X=3.846 mm

Y, mm	PPI	PPS	PPM	PPD
13.100	5	9	2	0
12.950	11	5	0	0
12.800	10	6	0	0
12.650	9	5	2	0
12.500	8	6	2	0
12.350	8	8	0	0
12.200	11	5	0	0
12.050	6	6	4	0
11.900	5	11	0	0
11.750	8	8	0	0
11.600	8	3	5	0
11.450	9	7	0	0
11.300	11	5	0	0
11.150	10	6	0	0
11.000	11	5	0	0
10.850	7	9	0	0
10.700	8	6	1	1
10.550	7	8	1	0
10.400	7	6	3	0
10.250	9	4	2	1
10.100	8	6	2	0
9.950	13	1	2	0
9.800	9	7	0	0
9.650	4	7	5	0
9.500	12	2	2	0
9.350	13	3	0	0
9.200	4	12	0	0
9.050	4	12	0	0
8.900	9	7	0	0
8.750	3	13	0	0
8.600	9	7	0	0
8.450	10	6	0	0
8.300	3	13	0	0
8.150	6	10	0	0
8.000	3	13	0	0
7.850	8	8	0	0
7.700	4	12	0	0
7.550	8	8	0	0
7.400	3	11	1	1
7.250	4	6	6	0
7.100	5	9	2	0
6.950	9	7	0	0
6.800	7	8	1	0
6.650	8	8	0	0
6.500	5	11	0	0
6.350	9	7	0	0
6.200	8	7	1	0
6.050	5	8	3	0
5.900	7	6	3	0
5.750	12	3	1	0
5.600	10	6	0	0
5.450	9	7	0	0
5.300	6	10	0	0
5.150	4	12	0	0
5.000	6	10	0	0
4.850	9	7	0	0
4.700	8	8	0	0
4.550	14	2	0	0
4.400	6	10	0	0
4.250	12	4	0	0



mode split variations during crack growth.

## 5.4 RESULTS AND DISCUSSION

### 5.4.1 Quantitative Fractography Results

The results from the FORTRAN program QSTATS established that the point-counting data were not normally distributed. The QSTATS program ran  $\chi^2$  tests with 13 degrees of freedom, meaning that the assumption of a normal distribution could be rejected with 95% confidence when  $\chi^2 > 22.362$ . The  $\chi^2$ -values for the point-counted data sets were always well over 100. This established that hypothesis tests based upon the assumption of normality could not be used, and that it was necessary to use a nonparametric approach such as the Mann-Whitney U-test.

The first point-counting was performed on the AS4-B501-6 specimens tested in-house. Point counting was performed with the SEM set at a nominal magnification of 500X and an actual magnification of approximately 650X. Point-counting was done every 2 mm of crack growth, accounting for the 0.015 inches consumed by each saw cut. Fifty fields of view were attempted for each point-count; sometimes as few as 40 were successful, due to large defected areas or other infrequent anomalies. Fields of view were examined 0.015 mm apart.

Table 12 shows the results of the initial point-counting. A statistically significant morphology change was defined as a location at which  $|Z| \geq 1.65$ .

Consider the locations at which statistically-significant morphology changes occur simultaneously for the first three damage modes. For specimen A, such locations are found at 15.65 mm from the starter notch, and at 26.24 mm from the starter notch. Because of the method of comparing adjacent data sets, these locations indicate changes in fracture morphology between 15.65 mm and 17.65 mm, and between 26.24 mm and 28.24 mm. These regions are close to the observed arrests



Figure 55: Mode I failure of brittle matrix composite<sup>[58]</sup>



Figure 56: Mode II failure of brittle matrix composite<sup>[58]</sup>

**TABLE 12: LOCATIONS OF STATISTICALLY  
SIGNIFICANT MORPHOLOGY CHANGES, mm,  
IN AS4/B501-6 SPECIMENS**

	INTERFACE FAILURE	SHEARING FAILURE	MATRIX MICROCR'K'G	PROCESSING DEFECTS
SPECIMEN		2.00	2.00	NONE
A	15.65	15.65	15.65	OBSERVED
	17.05		17.05	
		17.50		
			19.50	
	26.24	26.24	26.24	
	79.16	79.16		
SPECIMEN		3.00	NONE	3.00
B	5.00	5.00	OBSERVED	
		7.00		
	11.00	11.00		
	15.50			
		19.50		

at 18.3 mm and 24.4 mm. For specimen B, there is no correlation observed between the observed arrests and the statistically-significant locations. Equally significantly, there were no locations of statistically-significant variation in matrix microcracking in this specimen.

Figures 57 and 58 present these results in a graphic manner, comparing the results presented in Tables 7 and 12. The data are represented in two columns, one representing the locations of observed crack arrest, and the other representing the regions of statistically-significant morphology change. The left-hand column changes from light to dark, or vice versa, at each location of crack arrest. The right-hand column is shaded in the ranges over which statistically-significant morphology changes are found. Figure 57, illustrating specimen A, shows good correlation between arrests and statistically-significant morphology changes: the bands in the right-hand column are near the transitions in the left-hand column, and there are as many bands as transitions. In Figure 58, the bands are in the wrong places, and the correlation is poor.

Recall that the crack fronts of CLS specimens are usually nonlinear, and that the mean crack lengths recorded in the mechanical testing data are but approximations of the arrested crack length in the interior of the specimen. Furthermore, the data for the statistical analysis were taken at points well removed from the specimen edges, while the observed arrest data are based upon measurements taken at the specimen edges. Reference 40 notes that there can be a considerable discrepancy between edge measurements and interior measurements of crack growth, so much so that the edge measurements for that work were discarded when the data were analyzed. This makes the discrepancies between measured crack arrests and observed morphology changes less significant for specimen A.

For specimen B, however, this explanation is inadequate. While these data clearly do not support the effectiveness of this statistical approach, there were circumstances that might explain the poor results. Most significant is the contribution of the area fraction of defective material in this specimen. Compared to specimen

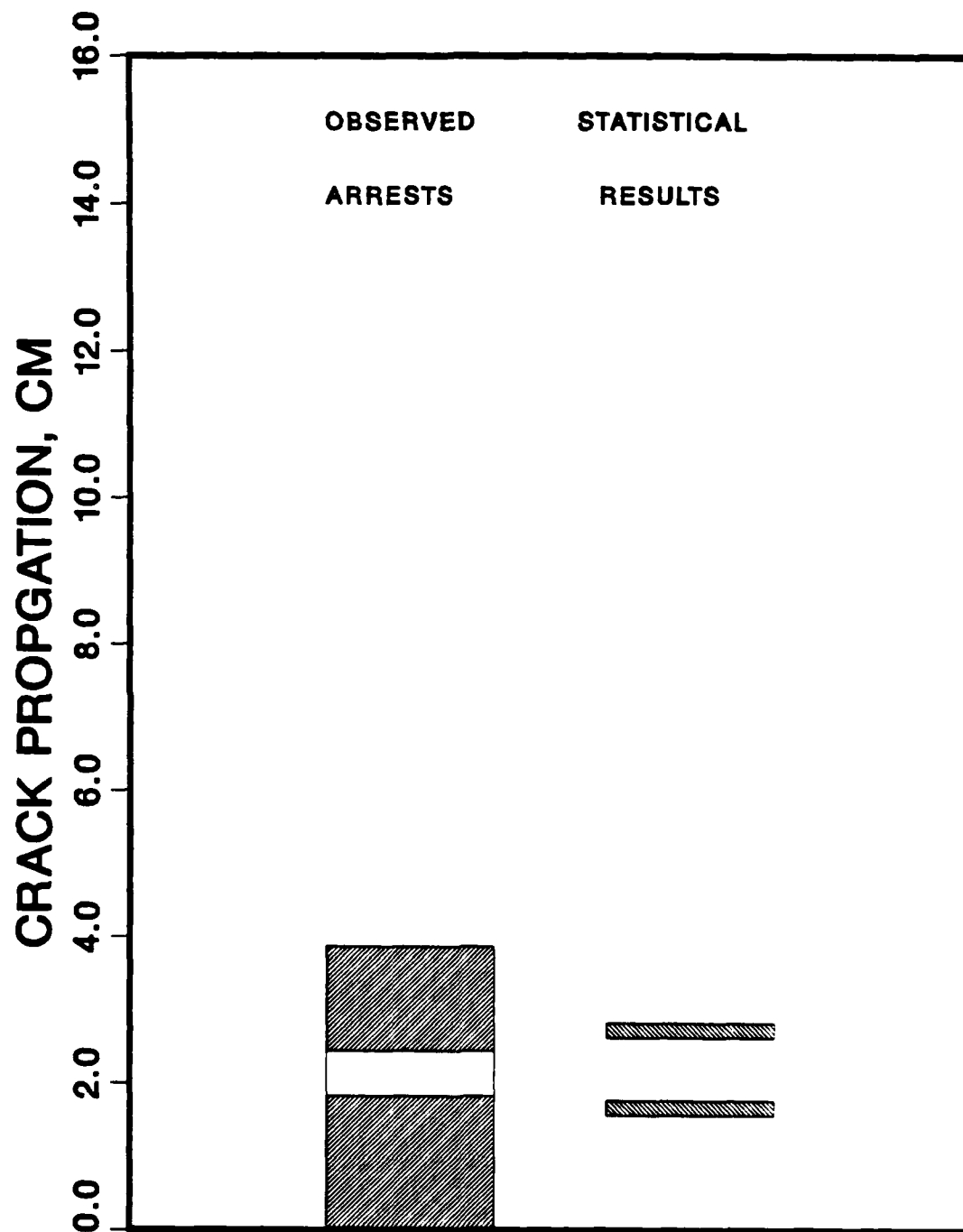


Figure 57. Comparison of crack arrests and morphology changes for specimen A

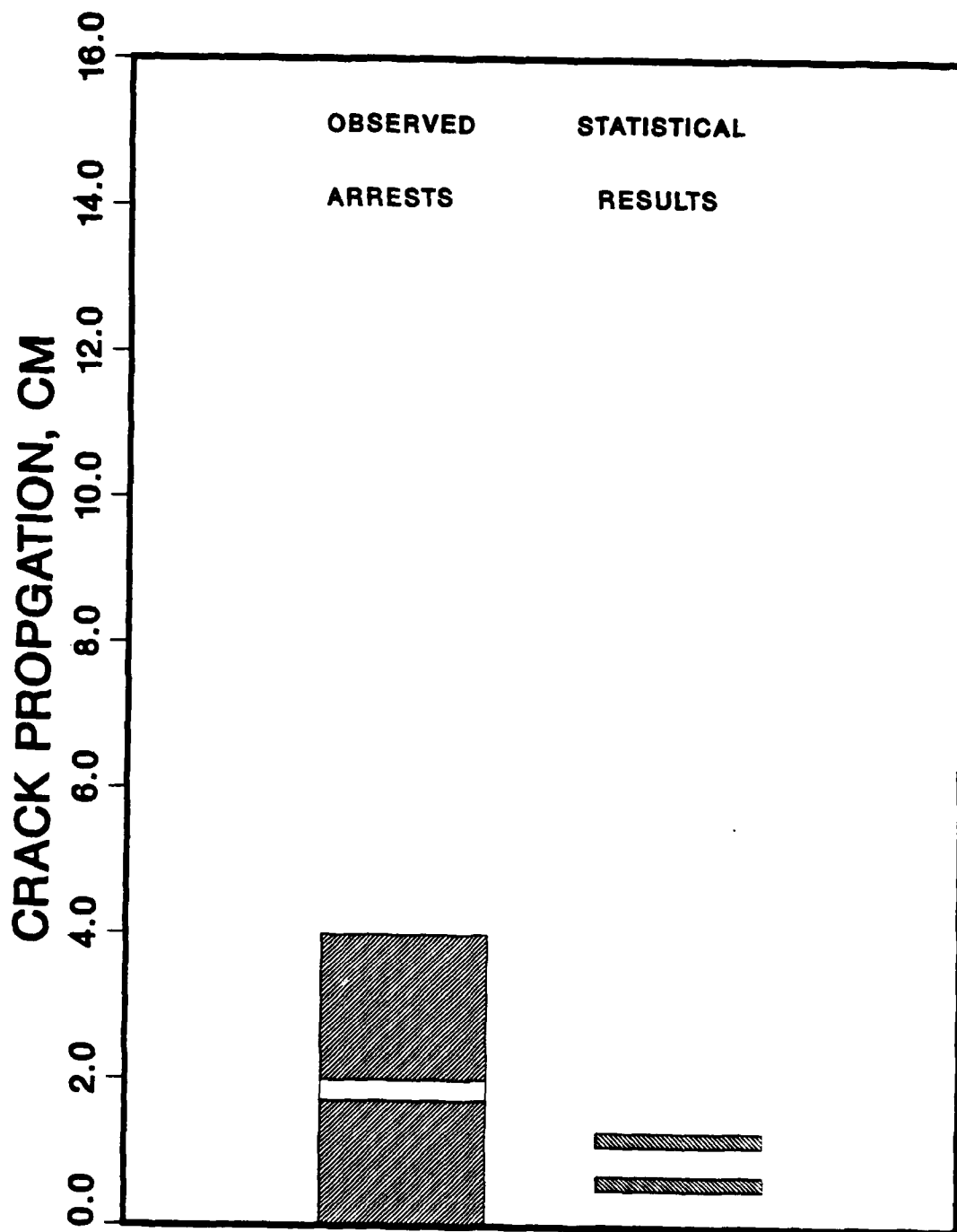


Figure 58. Comparison of crack arrests and morphology changes for specimen B

A, specimen B has both a larger area fraction of defects (14% to 8% ) and more variability in the area fraction of defects from location to location. Another factor that could have affected the behavior of specimen B was its splitting failure. Since the progress of the splitting was not measured, its contribution to the load-drop phenomenon cannot be determined.

A further look at the data from specimen A shows another noteworthy phenomenon. These data can be summarized as follows: between 15.65 mm and 17.65 mm of crack growth, the area fraction of interface failure increases, that of matrix failure decreases, and that of matrix microcracking increases. Between 26.24 mm and 28.24 mm of crack growth, the area fraction of interface failure decreases, that of matrix failure increases, and that of matrix microcracking decreases. This suggests a phenomenon that occurs between 15.65 mm and 17.65 mm, and then reverses itself between 26.24 mm and 28.24 mm. Furthermore, if all of the data taken between the two observed morphology changes are combined, and are then compared with the remainder of the data, it is seen that *PPI* and *PPM* are significantly greater between the morphology changes than elsewhere, *PPS* is significantly lower between the arrests than elsewhere, and *PPD* is not significantly different in the two zones. It is interesting to note that several of the CLS specimens exhibited bands of different shades across the fracture surface, as shown in Figure 59. This would also be consistent with the concept of a phenomenon that occurs and then reverses itself.

It should be noted that this point counting technique is not designed to detect morphology changes in a very small area near the arrest location. If, for example, some phenomenon occurs in a band of width 0.1 mm near each arrest, then this approach, which samples only every 2.0 mm, will not detect it. Thus, one cannot associate a given morphology with events very near the arrest region, based upon these results.

Adjustments in the point-counting process were made when the process was applied to the specimens not tested in-house. The sample size at each distance

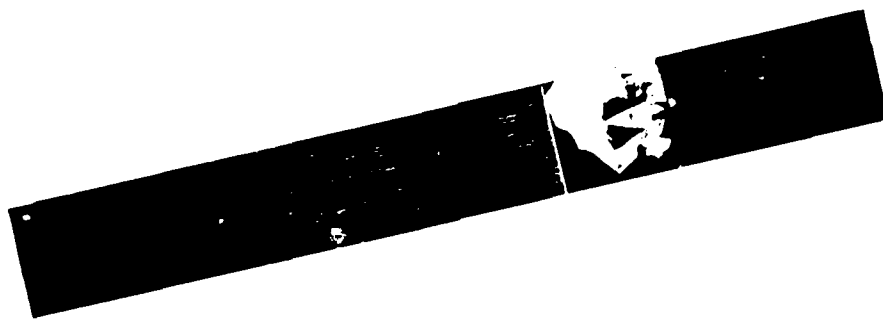


Figure 59. CLS specimen, showing bands of  
different shades on fracture surface



from the crack starter was decreased from a target of 50 successful fields of view to a mandatory 20 successful fields of view. Also, measurements were taken every 5 mm of crack growth, rather than every 2 mm of crack growth. These adjustments were made because the former methods could be argued to be too labor-intensive to be practical. The new method required one-sixth the number of fields of view per specimen, without significant loss of information. The effectiveness of the new method is demonstrated by the fact that the sample size is still 2.5 times the minimum sample size from the Mann-Whitney U-test, and by the fact that, in view of the data contained in Tables 9 and 10, few events would be missed using the increased crack growth increment.

Two other minor changes were made. The magnification for the point counting was increased from 500X nominal, 650X actual, to 1000X nominal, 1100X-1200X actual. This seemed to give better fields of view on the AS4/BP907 and AS4/PEEK specimens. Also, the spacing between fields of view was increased from 0.015 mm to 0.02 mm, so that the smaller sample size would not be distributed over too small an area of the fracture surface.

The results for those remaining specimens that were point-counted were far less encouraging than those for the AS4/B501-6 specimens. The data for the AS4/BP907 specimens is presented in Table 13, and two typical comparison bar graphs, of the type of Figures 57 and 58, are presented as Figures 60 and 61. These graphs compare data found in Tables 9 and 13. It is readily seen that correlation between observed crack growth arrests and statistically significant morphology changes is not good. This is the case even though the requirement that  $|Z| \geq 1.65$  for *PPM* was not imposed for these specimens, due to the infrequency with which it was satisfied. In some cases, the statistically-significant morphology changes are clustered at such low values of crack growth that they cannot even be seen on the chart.

Data from point-counting of the AS4/PEEK specimens is shown in Table 14. The comparison bar charts given as Figures 62 and 63, which compare the data from Table 14 with that from Table 10, show that the correlation between arrest

**TABLE 13: LOCATIONS OF STATISTICALLY SIGNIFICANT  
MORPHOLOGY CHANGES IN AS4/BP907 SPECIMENS, mm**

SPECIMEN	LOCATIONS
GD-7	0.0-0.5
	5.0-5.5
	5.5-6.0
GD-8	1.0-1.5
	3.5-4.0
GD-9	0.0-0.5
	0.5-1.0
	2.5-3.0
	6.5-7.0
L-4	0.0-0.5
	1.0-1.5
	2.5-3.0
	6.5-7.0
L-5	9.0-9.5
L-6	0.0-0.5
	4.0-4.5
	4.5-5.0
	8.5-9.0

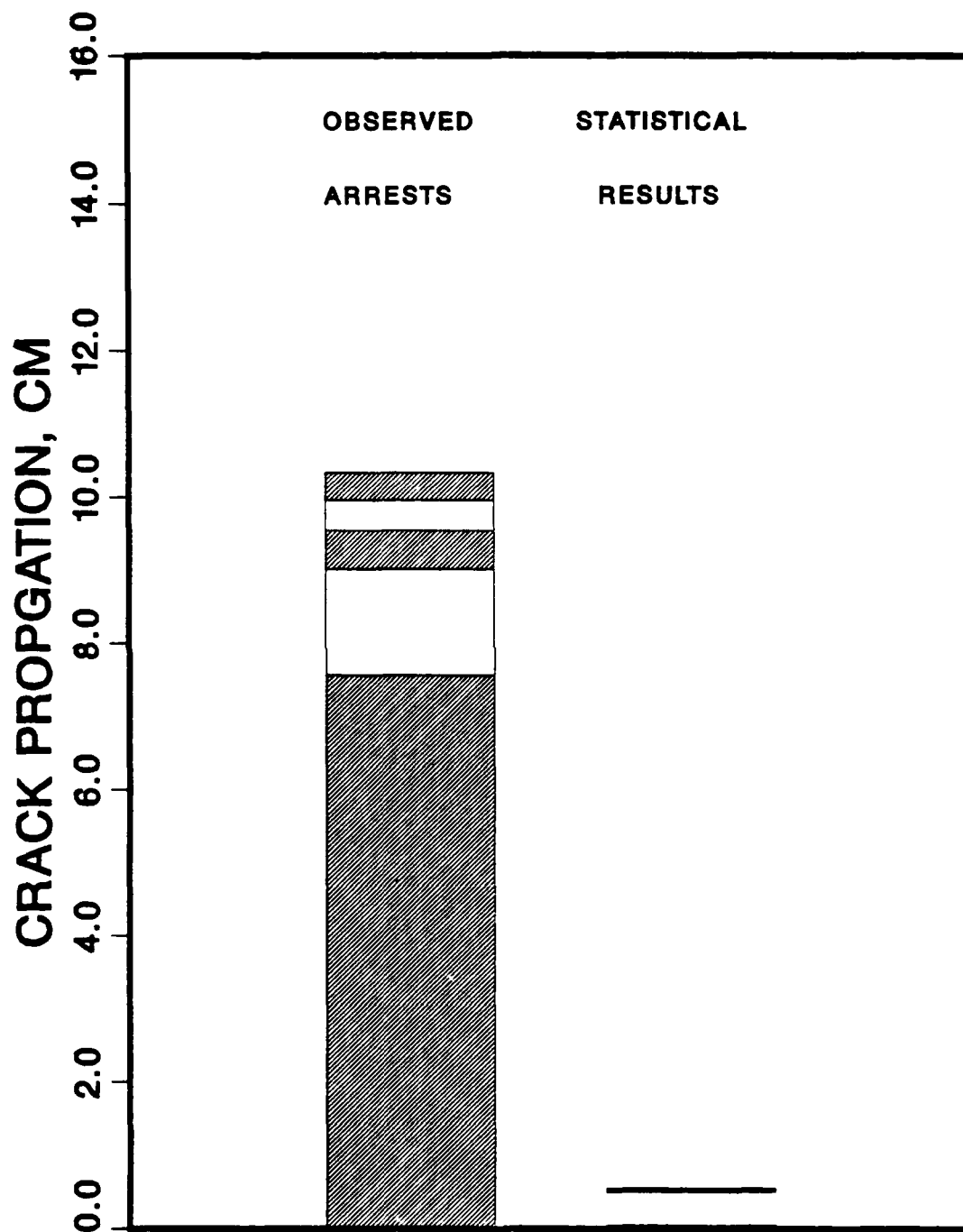


Figure 60. Comparison of arrests and morphology changes  
for specimen GD-7

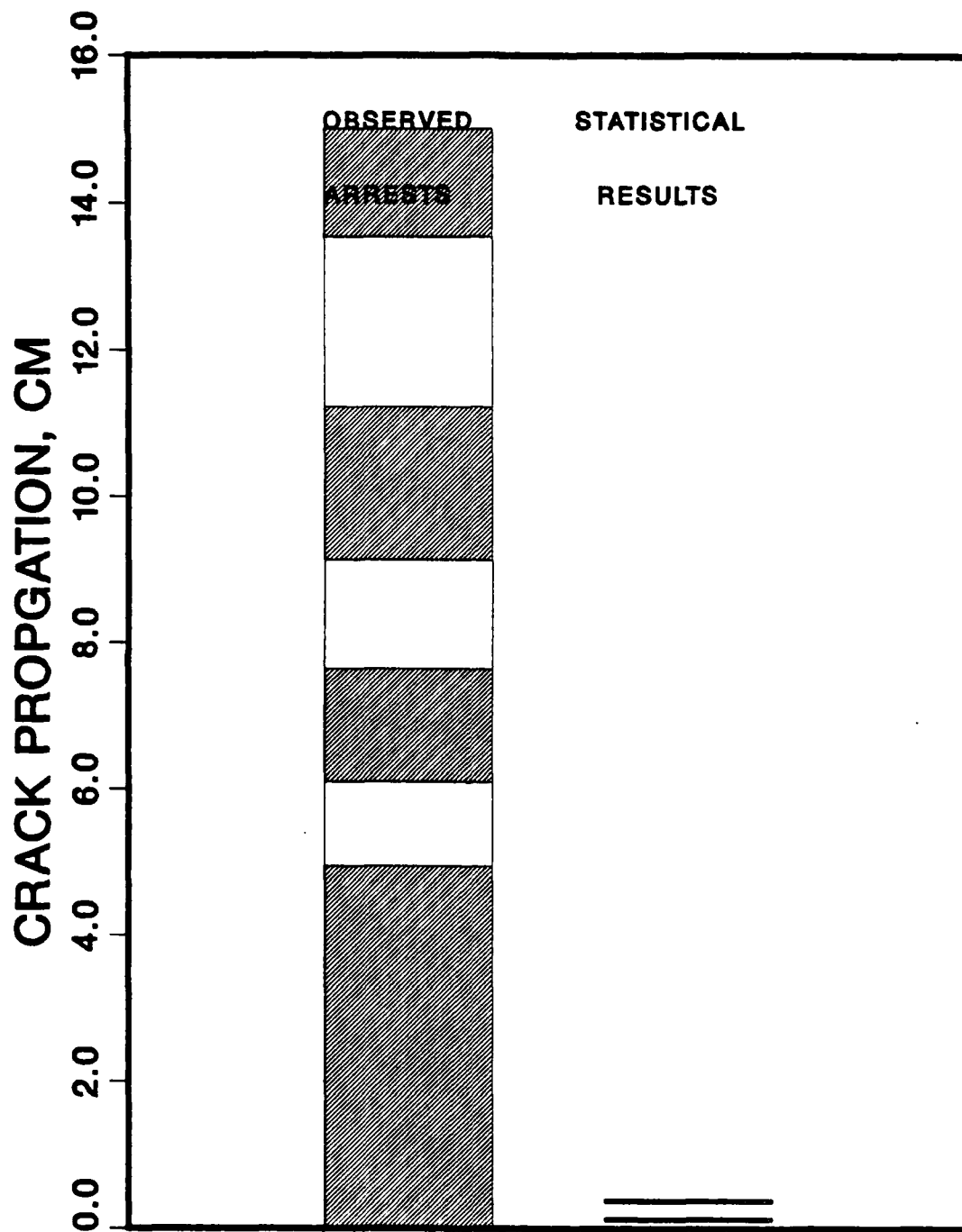


Figure 61. Comparison of arrests and morphology changes  
for specimen GD-8

and morphology change is again poor, with the statistically-significant morphology changes occurring so early during crack propagation that they cannot be seen on the charts. Only three specimens were point-counted, as a predictable pattern was seen in the fracture surfaces of these specimens. Figures 64, 65, and 66 illustrate this pattern. Near the crack starter notch, a narrow region of interface failure is found. This region is less than 1 mm in length. Following this region is one in which highly ductile matrix failure takes place. This region is typically less than 10 mm long. The third fracture morphology observed shows less ductile matrix failure, in which much smaller fibrils can be seen. This third morphology covers the remainder of the specimen, without significant variation.

Figure 67 suggests a reason for this variation. The presence of the teflon crack starter creates an increased spacing between the plies on either side of the crack plane, which would lead to a matrix-rich region. A thicker layer of matrix would lead to longer fibrils if ductile failure took place. Thus, long fibrils would be seen as the crack grew through the matrix-rich region, and shorter fibrils would be seen beyond this region.

If this explanation is correct, there is no reason why a similar effect should not be seen in the brittle-matrix specimens. Consider the results shown in Table 13. Four of the six specimens showed statistically significant morphology changes between 0.0 mm and 0.5 mm of crack growth. Consultation of the QSTATS output for these specimens showed that all four of these early morphology changes denoted an increase in interface failure and a decrease in matrix failure. This would be consistent with a reduction in the thickness of the matrix layer along the crack plane. In view of these results, it seems likely that the variation of interface and matrix failure along the fracture surface is driven largely by matrix layer thickness, and that point counting by this criterion merely detects variations in this matrix layer thickness. This observation is critical, since the CLS test is a proposed ASTM standard for measuring mixed-mode fracture toughness in laminated composite materials. The results of the quantitative fractography suggest that crack starter geometry may

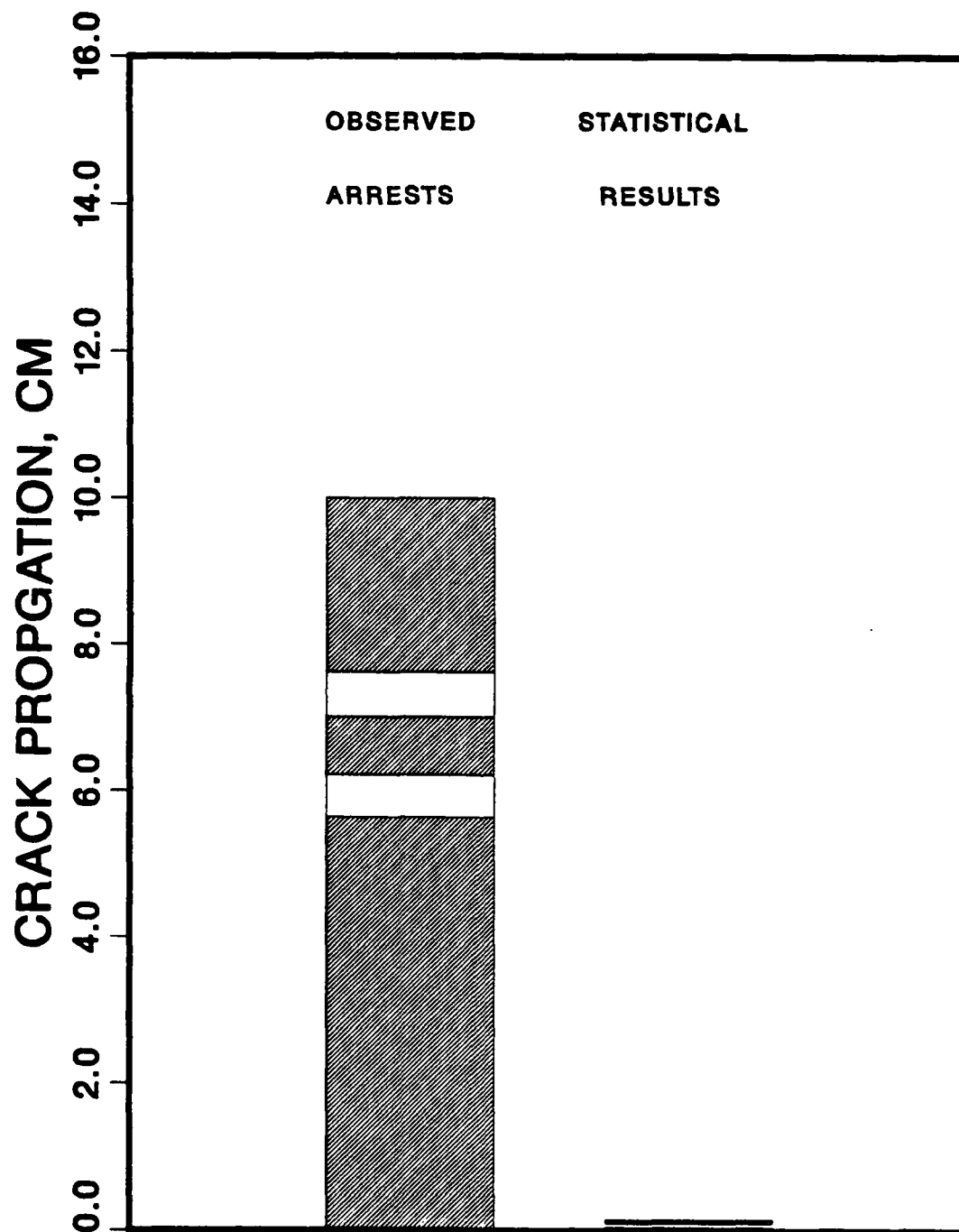


Figure 62. Comparison of arrests and morphology changes  
for specimen GD-2

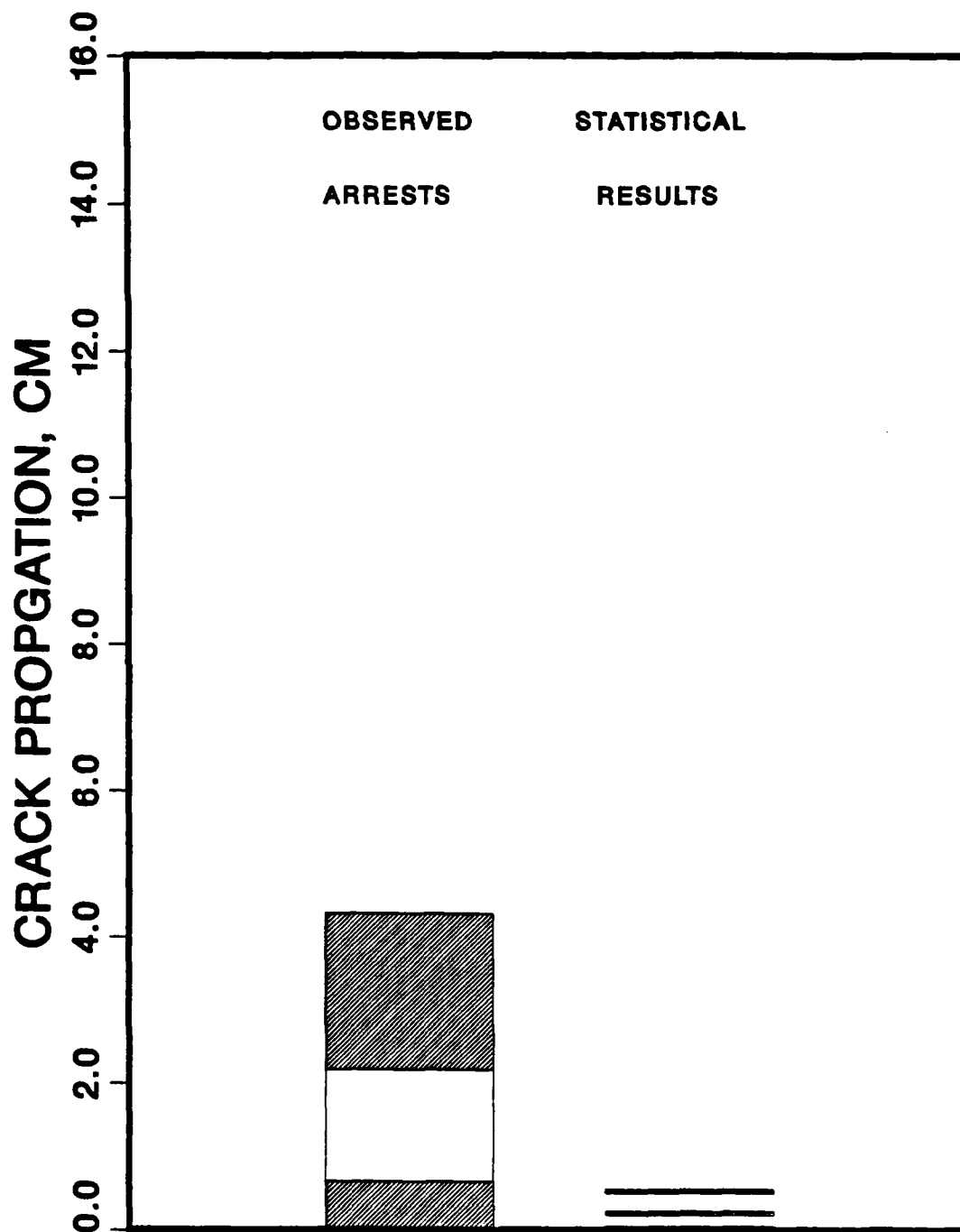


Figure 63. Comparison of arrests and morphology changes  
for specimen L-10

**TABLE 14: LOCATIONS OF STATISTICALLY SIGNIFICANT  
MORPHOLOGY CHANGES IN AS4/PEEK SPECIMENS, mm**

SPECIMEN	LOCATIONS
GD-1	0.0-0.5
	0.5-1.0
	1.0-1.5
GD-2	0.0-0.5
	1.0-1.5
L-10	0.0-0.5
	2.0-2.5
	5.0-5.5



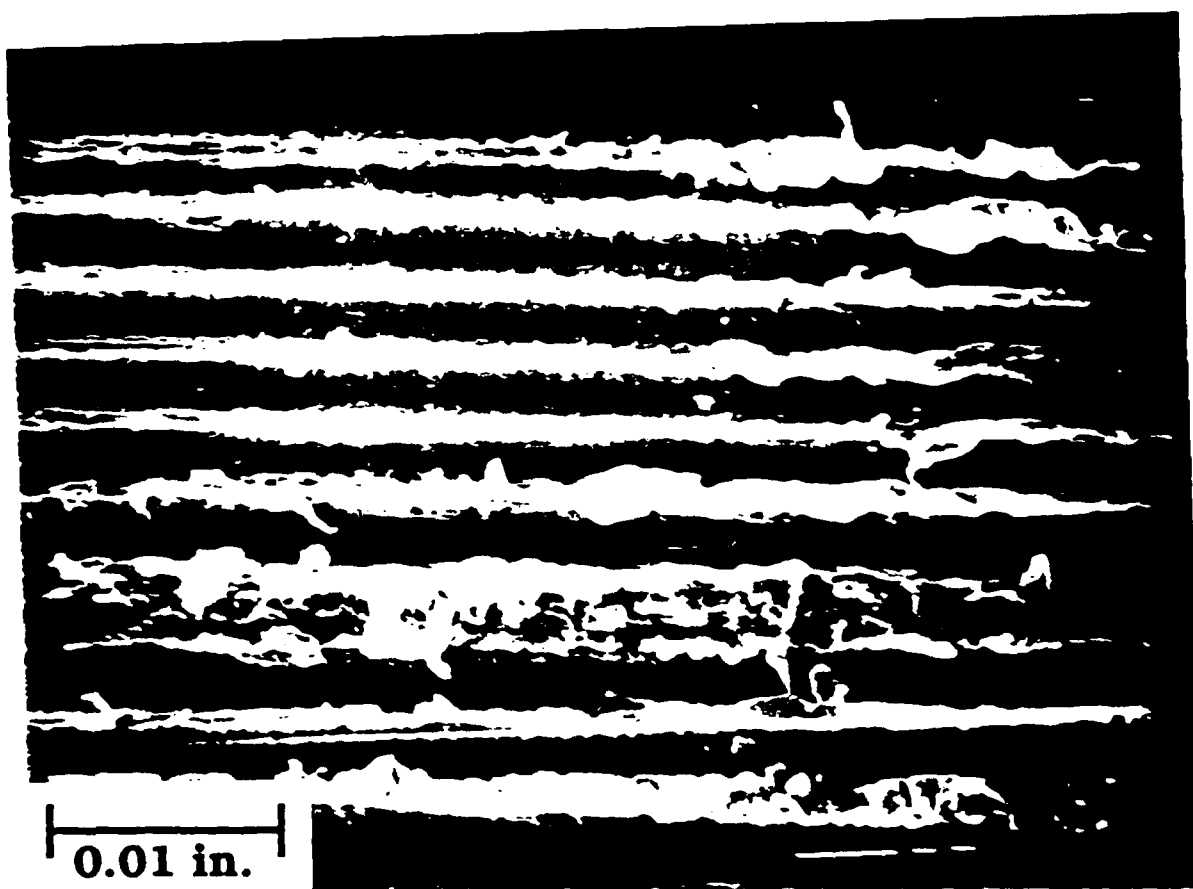


Figure 64: Interface failure near crack starter  
in AS4/PEEK CLS specimen

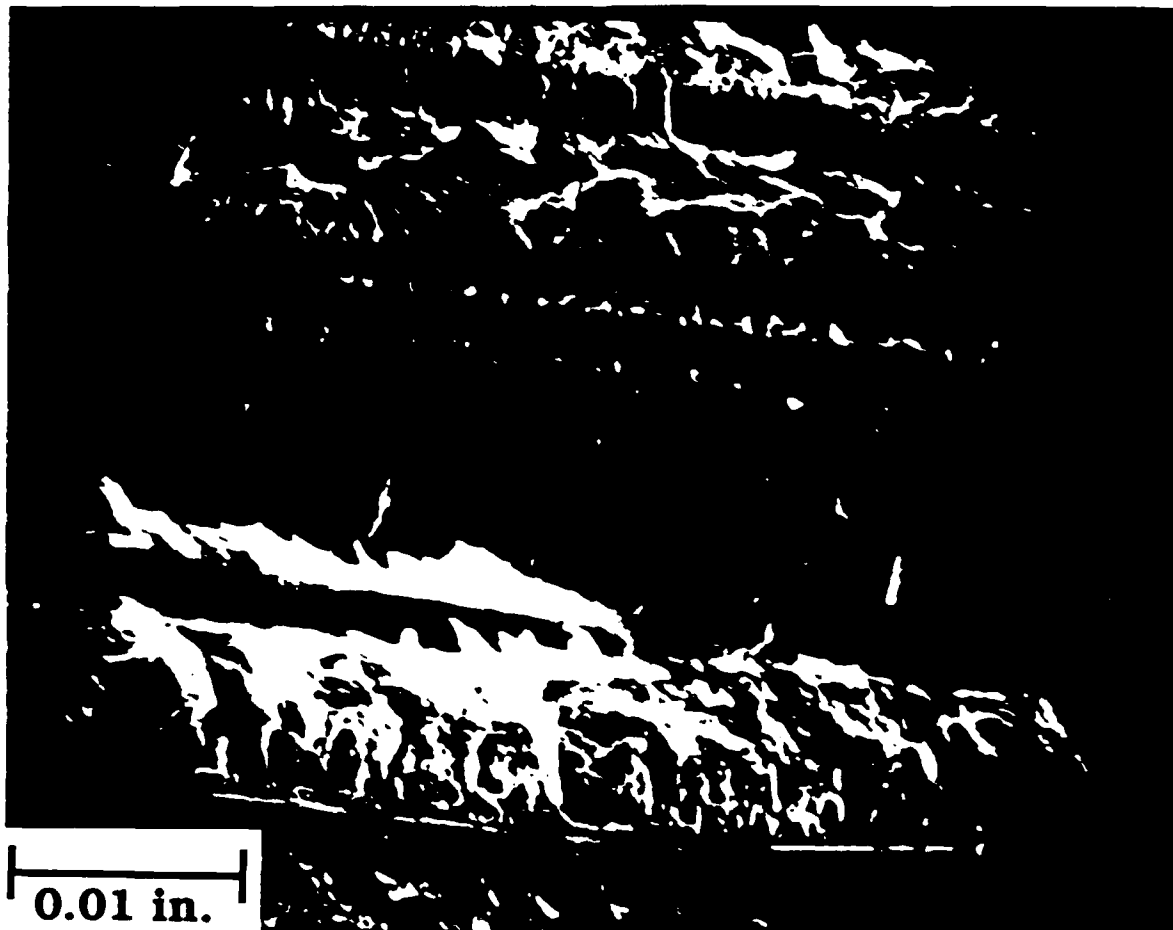


Figure 65: Highly ductile failure in AS4/PEEK CLS specimen

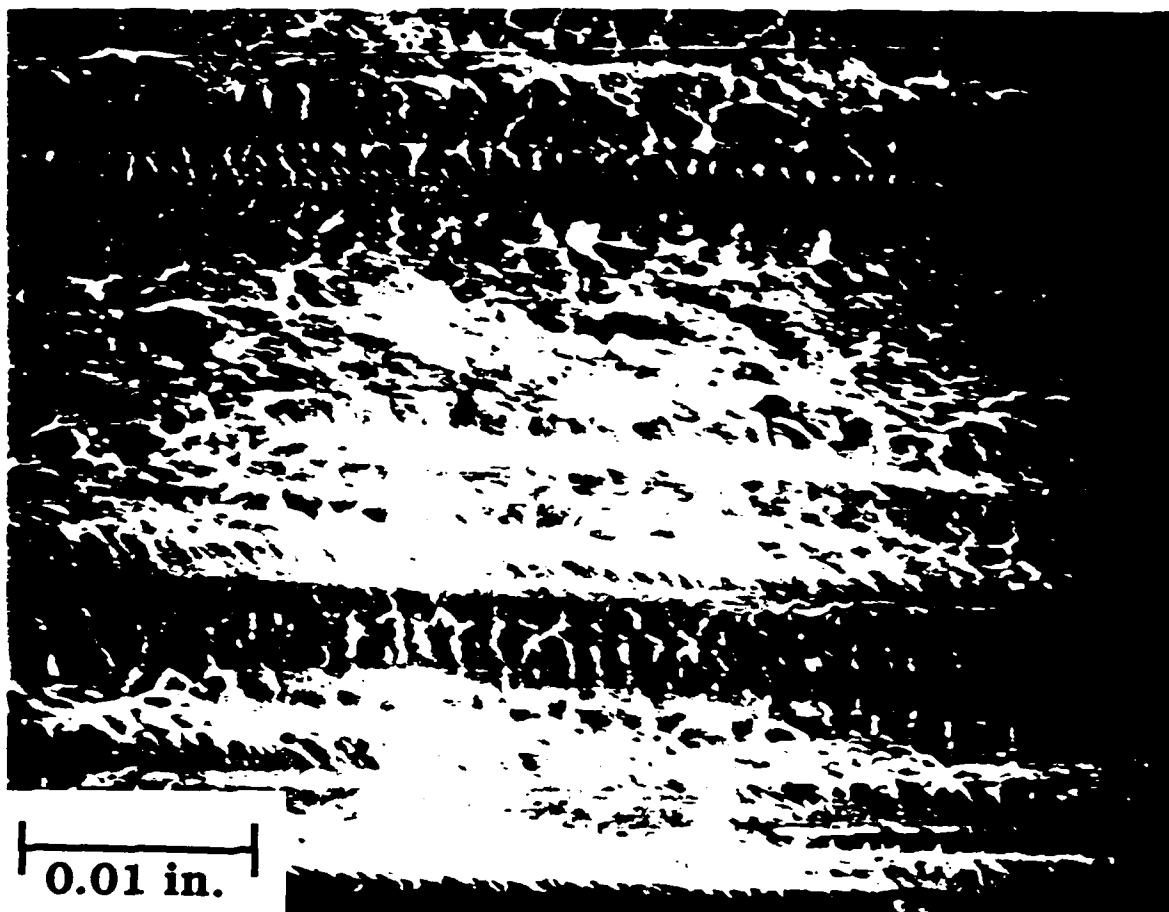


Figure 66: Ductile failure in AS4/PEEK CLS specimen,  
showing shorter fibrils

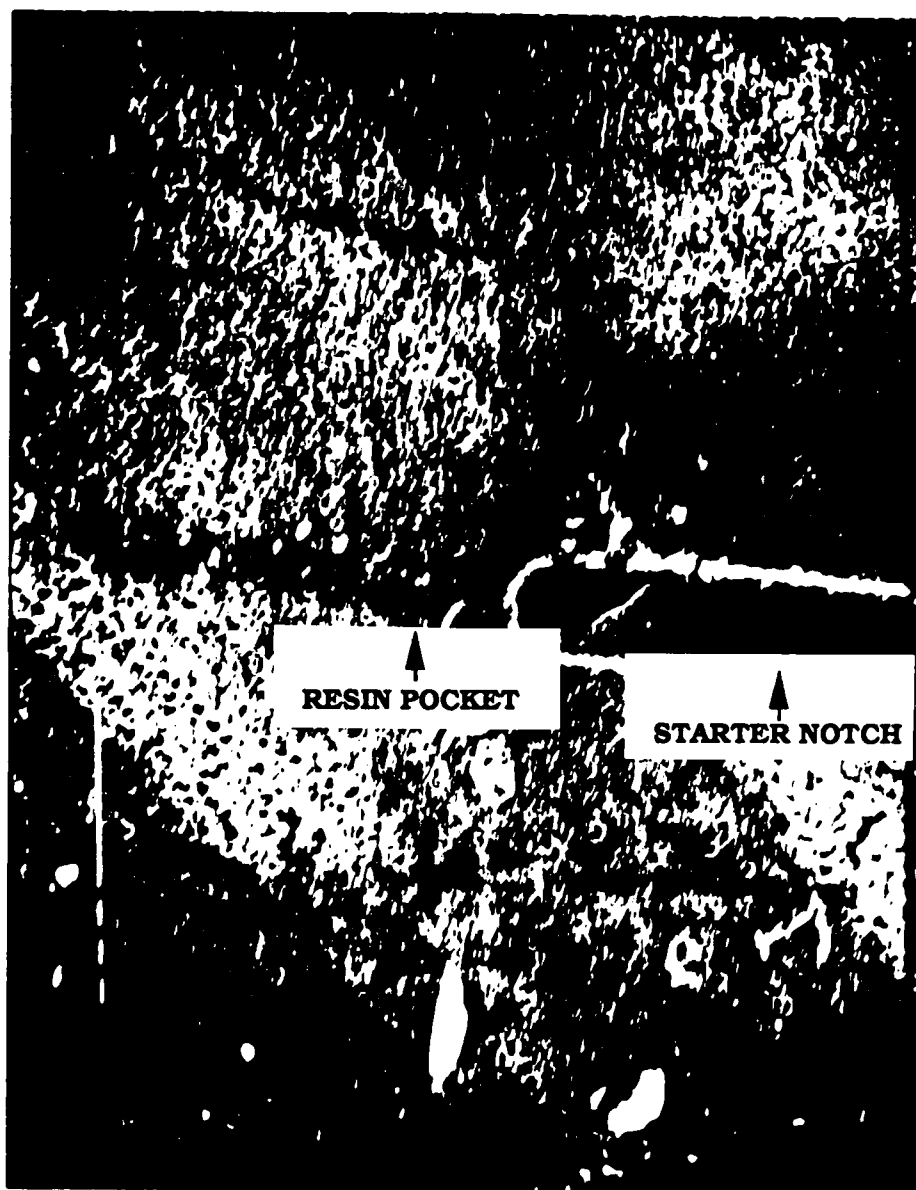


Figure 67: Variation of matrix layer thickness  
along crack plane of CLS specimen, near crack starter

play an important role in the performance of CLS specimens. This is corroborated by the work of OBrien<sup>[59]</sup>, whose experiments with CLS specimens showed a correlation between observed fracture toughness and the thickness of the crack starter. This would not prejudice the data from CLS tests if the composite fracture toughness was determined solely by matrix properties; however, this is not the case.

At this point, however, it would be reasonable to question whether the point counting measures anything at all. A simple probabilistic analysis sheds some light on this issue. Consider again the data given in Tables 13 and 14. For these two tables, a total of 149 statistical comparisons were performed, of which 27 resulted in simultaneous, statistically-significant variations in *PPI* and *PPS*. Assume, for the sake of conservatism, that *PPI* and *PPS* are related, and that therefore a statistically-significant change in one implies a statistically-significant change in the other. Thus, since the hypothesis tests were conducted at a 90% confidence level, there is a 10% probability that a given hypothesis test will show a statistically-significant morphology change, if *PPI* and *PPS* are in fact random. (If *PPI* and *PPS* are assumed to be independent, this probability decreases to 1% .) Thus, approximately 15 statistically-significant variations out of 149 tests would be expected. The difference between the mathematically-expected number of such variations and the observed number is  $27 - 15 = 12$ . It remains to calculate the probability of this difference being 12 or more; that is, of the observed number of statistically-significant variations being less than or equal to three, or greater than or equal to 27.

From Reference 60, the number of statistically-significant morphology changes observed, assuming that the data is actually random, is seen to have a binomial distribution. The desired probability  $P$  can be calculated exactly as:

$$P = \sum_{\substack{0 \leq x_0 \leq 3 \\ 27 \leq x_0 \leq 149}} \frac{n_0!}{x_0!(n_0 - x_0)!} p_0^{x_0} (1 - p_0)^{n_0 - x_0} \quad (91)$$

where

$x_0$  is the number of statistically-significant morphology changes observed

$n_0$  is the total number of trials

$p_0$  is the probability of a successful trial

For the current example,  $n_0 = 149$  and  $p_0 = 0.1$ . Therefore, from equation (91),  $P = 0.00188$ . In other words, there is less than one chance in 500 that the actual number of statistically-significant variations would be so different from the mathematical expectation, if the data was actually random. Figure 68 illustrates the probability distribution for the number of statistically significant variations observed in random data, showing how unlikely it is to have 27 such occurrences. It is likely, therefore, that something is being measured by the point counting procedure. It is most probable that what is being measured is variations in the matrix thickness along the crack plane.

The results of the quantitative fractography experiments suggest that the arrest phenomenon cannot be attributed to local characteristics of the unidirectional CLS specimen. This, in turn, implies that arrest can be described from a purely mechanical viewpoint.

#### **5.4.2 Mechanical Crack Propagation Model**

The behavior of the CLS specimen can be modelled by investigating the variation of the specimen compliance with crack growth. The load drop exhibited during crack propagation is caused by an increase in the compliance of the specimen as the crack grows; thus, a model is needed to relate crack growth to the compliance of the CLS specimen, and thus to the load on the specimen.

Consider the simple illustration of the CLS specimen shown in Figure 69. Assume that the shaded portion of the lap, the region above the crack, is fully un-

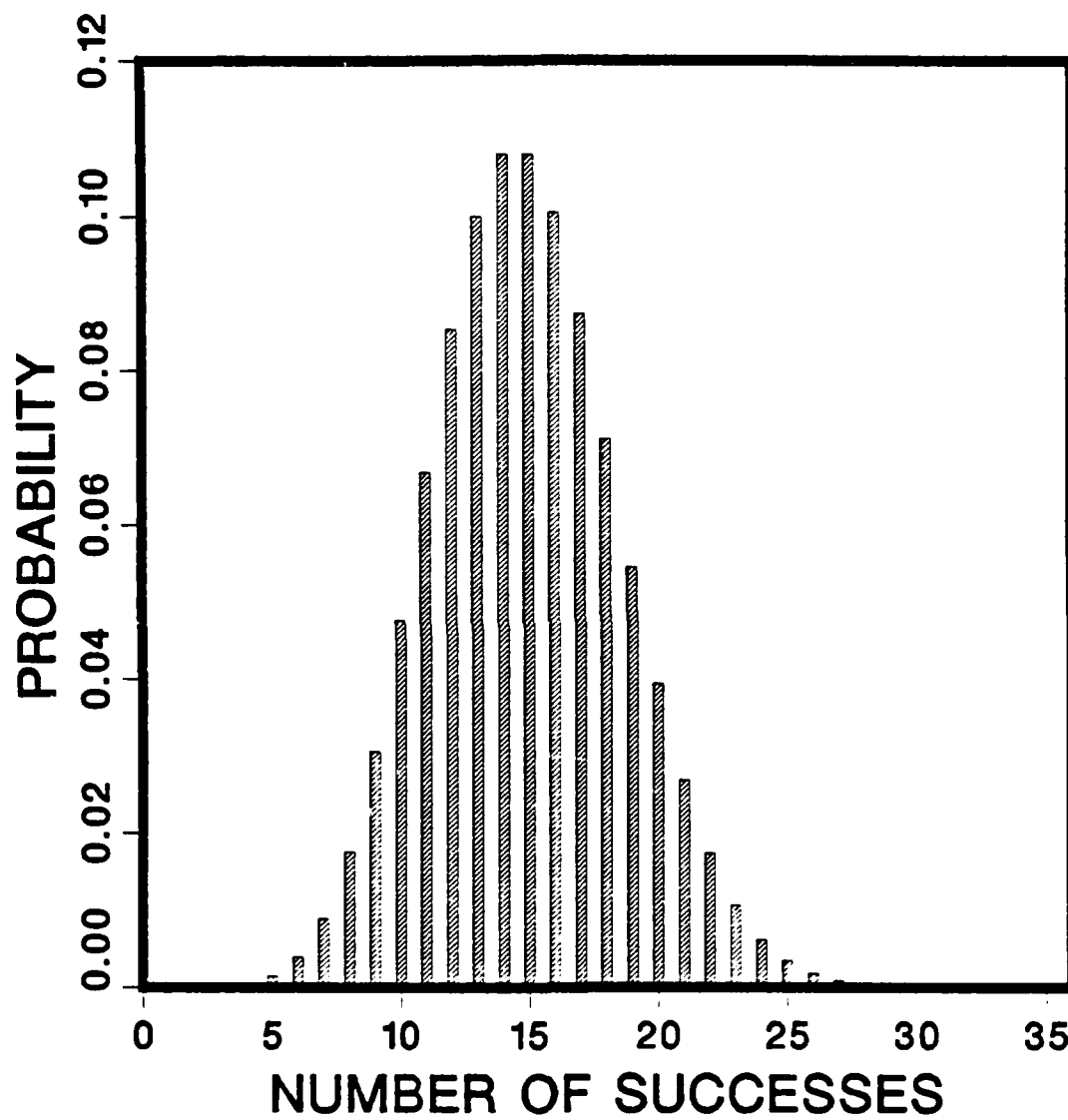


Figure 68. Probability distribution for the number of statistically significant variations, assuming random data

loaded, and that the specimen can be considered as two rectangular cross-section bars, one of thickness  $t_1$  and length  $L_1$ , and one of thickness  $t_2$  and length  $L_2$ . Assume, further, that the crack remains planar and parallel to the loading direction. This is essentially a one-dimensional model; however, it is noted in Reference 40 that such simple models compare well with more refined approaches. When a crosshead deflection  $\bar{\delta}$  is imposed, a load  $P$  arises, and the two bars are loaded in series. It is seen that, for this case,

$$P = \frac{EBt_1t_2}{t_2L_1 + t_1L_2 + (t_2 - t_1)a} \times \bar{\delta} \quad (92)$$

Where  $E$  is the effective modulus of the two bars (assumed the same for this analysis, since the specimen is unidirectional), and  $B$  is the width of the specimen. Thus, the compliance,  $C$ , of the specimen is

$$C = \frac{t_2L_1 + t_1L_2 + (t_2 - t_1)a}{EBt_1t_2} \quad (93)$$

It should be noted that this development assumes an infinitely stiff testing machine.

With this compliance expression, it is possible to model the strain energy release rate behavior of a CLS specimen as a crack propagates. During the propagation event, two phenomena affect the strain energy release rate. First, the crack is propagating at the speed of sound, causing the load to drop and reducing the strain energy release rate. Second, the crosshead is continuing to progress, causing the load and the strain energy release rate to increase. Both of these events can be incorporated into a model that will allow the tracking of strain energy release rate versus crack extension.

The Williams equation for in-plane extension, given in equation 23, can be used to develop a simple expression for the total strain energy release rate in terms of the load. It is seen that  $P_1 = P$  and  $P_2 = 0$  for the CLS specimen, resulting in the



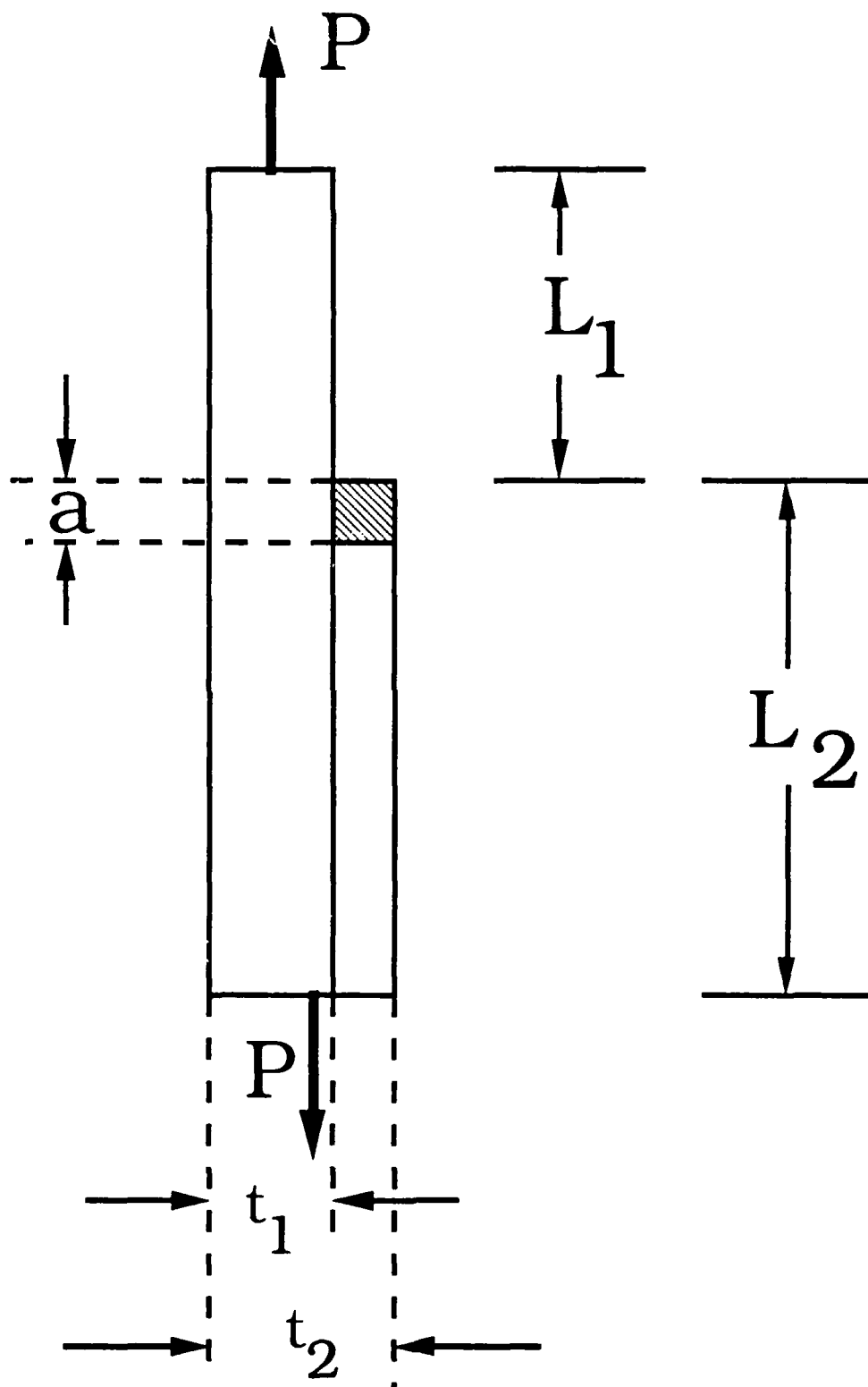


Figure 69: Schematic side view of CLS specimen

expression

$$G = G_P = \frac{P^2}{2B^2hE} \left( \frac{1}{\xi} - 1 \right) \quad (94)$$

This is very similar to the expression<sup>[61]</sup>

$$G = \frac{P^2}{2b} \frac{dC}{da} \quad (95)$$

which is derived from the Griffith-Irwin fracture theory. If  $G_c$  is the fracture toughness of the material of which the specimen is made, then, from Equation 94,

$$P_c = \sqrt{\frac{2B^2hEG_c\xi}{1-\xi}} \quad (96)$$

where  $P_c$  is the load at which crack growth begins. Equation 96 is derived assuming the Griffith fracture criterion

$$G = G_c \quad (97)$$

Consider a situation in which crack growth is incipient. The crosshead displacement is  $\bar{\delta}_0$  and the crack length before propagation is  $a_0$ . Equation 92 gives the crosshead displacement in terms of the initial crack length:

$$\bar{\delta}_0 = \frac{P_c(t_2L_1 + t_1L_2 + (t_2 - t_1)a_0)}{EBt_1t_2} \quad (98)$$

Now consider the situation where the crosshead begins to travel at speed  $\dot{\delta}$ . The crack propagation speed,  $\dot{a}$ , will be approximately the speed of sound, which is

dependent upon the medium; for purposes of discussion,  $\dot{a}$  will be approximated here by the speed of sound in dry air. At this point, the initial crosshead location, initial crack length, crosshead speed and crack propagation speed are all known, allowing the calculation of  $G$  at a function of the time  $\tau$ :

$$a = a_0 + \dot{a}\tau \quad (99)$$

$$\bar{\delta} = \bar{\delta}_0 + \dot{\bar{\delta}}\tau \quad (100)$$

$$= \dot{\bar{\delta}} + \frac{P_c\tau(t_2L_1 + t_1L_2 + (t_2 - t_1)a_0)}{EBt_1t_2} \quad (101)$$

The values for  $a$  and  $\bar{\delta}$  given by equations 99 and 101 can now be substituted into equation 92 to find  $P$ , and  $P$  can then be substituted into equation 94 to find  $G$ . The resulting equation is

$$G = \left( \frac{\dot{\bar{\delta}}\tau EBt_1t_2 + P_c\tau(t_2L_1 + t_1L_2 + (t_2 - t_1)a_0)}{t_2L_1 + t_1L_2 + (t_2 - t_1)(a_0 + \dot{a}\tau)} \right)^2 \left( \frac{1 - \xi}{2\xi B^2 h E} \right) \quad (102)$$

Since equation 99 allows the determination of  $a$  as a function of time,  $G$  can be plotted as a function of  $a$ , using the time  $\tau$  as a parameter.

As an illustration, consider the example of a CLS specimen test, as described in Table 15. This configuration is typical of an AS4/BP907 specimen from the ASTM round robin. Figure 70 shows plots of the available strain energy release rate  $G$  versus increment of crack length for cracks of varying initial lengths. Three conclusions can be drawn from this plot. First, the strain energy release rate of a crack growing in a CLS specimen decreases with increasing increment of crack length. Second, the decrease is approximately linear for most practical configurations, and, for the

values of crack growth likely to be encountered, only small decreases in  $G$  are seen. Finally, the magnitude of the slope decreases with increasing initial crack length.

One phenomenon shown in Figure 70 is worthy of explanation. Consider a crack of initial length 1.0 inches, with no subsequent growth. Call this case 1. According to Figure 70, the available strain energy release rate associated with this crack is 4 in-lb/in<sup>2</sup>. But case 2, a crack of initial length 0.0 inches, which propagates 1.0 inches, has an available  $G$  of about 3.6 in-lb/in<sup>2</sup>, although it has the same length of 2.0 inches. This apparent contradiction arises because of the way the specimen model is approached; the loads will be different in these two cases. From equation 96,  $P_c$  is not a function of crack length, as long as  $G_c$  is not a function of crack length. Thus, cases 1 and 2 begin at the same load, but, in case 2, the load drops as the crack propagates.

Several comments can be made on the basis of this simple analysis. First note that, from the point of view of the Williams analysis in Reference 28, the length of a crack in a CLS specimen is irrelevant to the strain energy release rate associated with that crack, under load-controlled testing. Thus, for initiation purposes, the initial crack length is a non-factor. Initial crack length only becomes important during propagation, when the displacement-controlled nature of the test becomes significant, and its effect then is a function of the finite length of the specimen. Finally, the limitations of using the Griffith fracture law must be discussed. This approach neglects the effect of mode split, which may be important in characterizing the behavior of this specimen.

Since the strain energy release rate associated with a flaw in a CLS specimen decreases immediately as the crack length increases, there is some question as to why the crack propagates at all. One possibility is the existence of an initial resistance to the growth of a flaw, causing the flaw to require a higher strain energy release rate to begin growth than to sustain it. In view of figure 70, with its flatter curves associated with larger initial crack sizes, this would lead to an increase in the incremental crack growth  $\Delta a$  with increasing crack length. The reason for this may be demonstrated

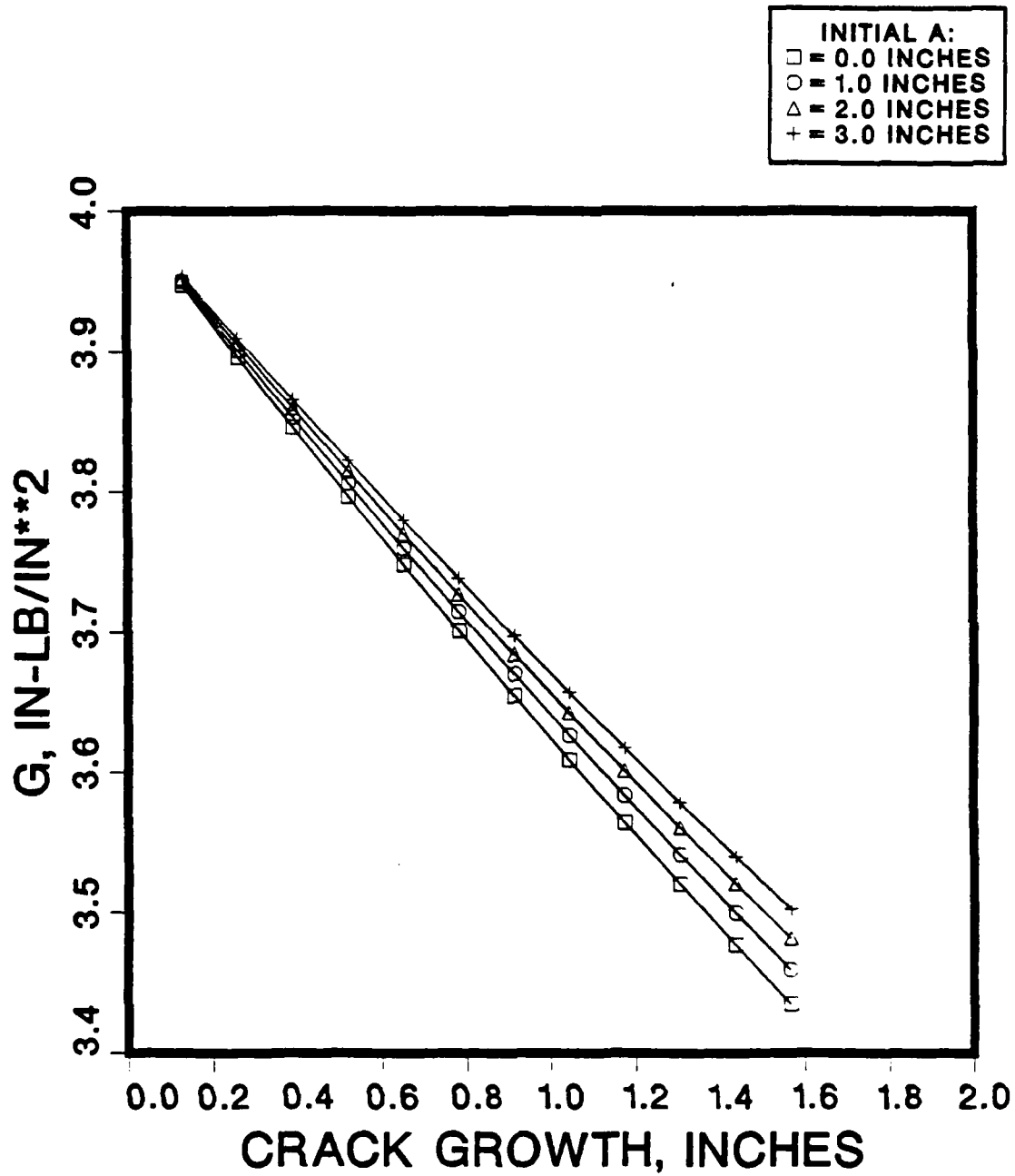


Figure 70:  $G$  versus  $\Delta a$  for CLS specimen  
at several initial crack lengths

**TABLE 15: SPECIFICATIONS OF SPECIMEN IN  
MECHANICAL CRACK PROPAGATION MODEL**

---

MATERIAL	AS4/BP907
LAYUP	UNIDIRECTIONAL
LAP LENGTH, INCHES	6.0
STRAP LENGTH, INCHES	9.0
WIDTH, INCHES	1.0
$t_1$ , INCHES	0.065
$t_2$ , INCHES	0.100
$\dot{\delta}$ , inches/minute	0.05
$E$ , psi	$17.65 \times 10^6$
$G_c$ , in-lb/in <sup>2</sup>	4.00

by a hypothetical example based upon the data of Figure 70. Assume that, for example, a strain energy release rate of 4 in-lb/in<sup>2</sup> is required for initiation of a flaw, but only 3.6 in-lb/in<sup>2</sup> is required to continue propagation once it has begun. From Figure 70, a crack of initial size 0.0 inches would propagate approximately 1.0 inches before the available  $G$  dropped below the threshold of 3.6 in-lb/in<sup>2</sup>, while a crack of initial length 3.0 inches would propagate more than 1.2 inches.

The drop in the available  $G$  may seem counterintuitive. It is helpful to note that, since the crack growth rate is so much larger than the crosshead speed, the situation is very similar to a constant-displacement test.

The ASTM round robin AS4/BP907 specimens tested by General Dynamics show approximately constant initiation loads, in accordance with the predictions of this model; consequently, it might be expected that the relationship between  $a$  and  $\Delta a$  predicted by the model might also be seen. A plot of  $\Delta a$  versus  $a$  for these specimens is given as Figure 71.

The hypothetical example given in Table 16 helps to explain what is plotted in Figure 71. The data points are derived from the arrest locations for each specimen.

Clearly, the data shows a great deal of scatter; however, it is possible to determine whether or not it can be said, from this data, that  $\Delta a$  increases with increasing  $a$ . Fit a straight line to the data:

$$\Delta a = ma + b \quad (103)$$

it is possible to test the hypothesis  $m = 0$  against the alternative  $m > 0$ . There are not enough data points to assume a normal distribution, and from Reference 62, the appropriate  $t$ -statistic for testing this hypothesis is

$$t = \frac{m}{s_e} \sqrt{\frac{S_{xx}}{n}} \quad (104)$$

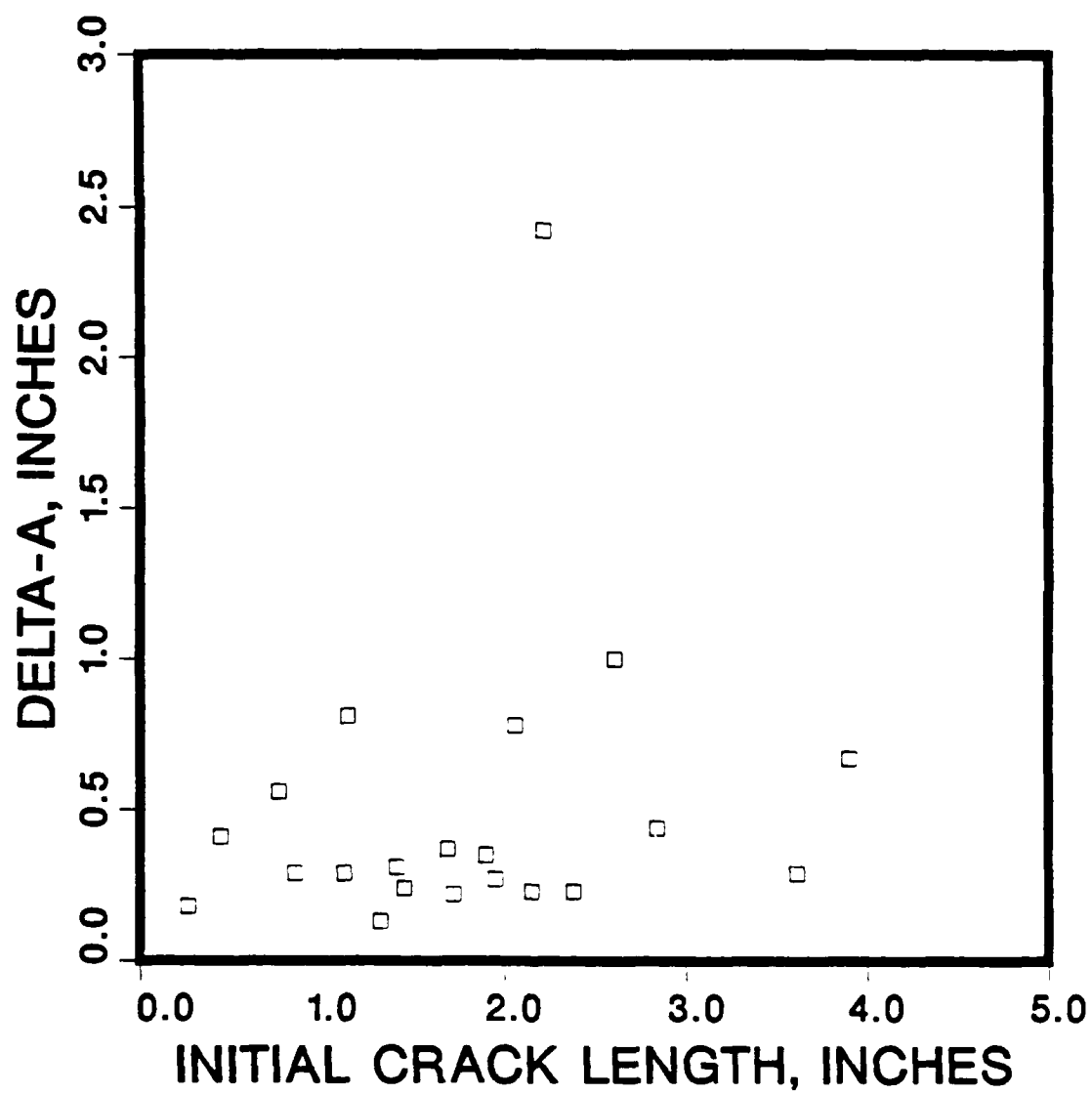


Figure 71:  $\Delta a$  vs.  $a$  for AS4/BP907 specimens  
tested by General Dynamics



**TABLE 16: HYPOTHETICAL DATA ILLUSTRATING DERIVATION  
OF  $\Delta a$  vs.  $a$  CURVE**

INITIAL CRACK LENGTH $a$ , CM	$\Delta a = a_i - a_{i-1}$	DATA POINT PLOTTED
0.00	-----	-----
0.10	0.10	(0.00, 0.10)
0.30	0.20	(0.10, 0.20)
1.10	0.80	(0.30, 0.80)
2.10	1.00	(1.10, 1.00)
3.80	1.70	(2.10, 1.70)

where the statistics terms are defined as follows:

$$s_e = \frac{S_{xx}S_{yy} - (S_{xy})^2}{n(n-2)S_{xx}} \quad (105)$$

$$S_{xx} = n \sum_{i=1}^n x_i^2 - \left( \sum_{i=1}^n x_i \right)^2 \quad (106)$$

$$S_{yy} = n \sum_{i=1}^n y_i^2 - \left( \sum_{i=1}^n y_i \right)^2 \quad (107)$$

$$S_{xy} = n \sum_{i=1}^n x_i y_i - \left( \sum_{i=1}^n x_i \right) \left( \sum_{i=1}^n y_i \right) \quad (108)$$

and where  $n$  is the number of data points. For the data shown in Figure 71, the hypothesis  $m = 0$  can be rejected in favor of the alternative hypothesis  $m > 0$  at the 95% confidence level. While hardly conclusive proof that the current model is correct, this does provide some supporting evidence.

## 5.5 CLOSURE

A fractographic analysis of several failed unidirectional CLS specimens has been performed, using probabilistic techniques to locate changes in the morphology of the fracture surface. This analysis has been applied to both brittle-matrix and tough-matrix material systems. In both cases, the changes in fracture morphology observed do not generally correlate with the locations of crack arrest, although one example of correlation has been found in a brittle matrix specimen. Rather, it is likely that the morphology changes are indicative of variations in the thickness of the matrix layer along the crack plane. This indicates that, if any changes in the

fracture surface are caused by crack arrests, they are too highly localized to be found by the point-counting technique.

The significance of these results is that they support the validity of the cracked lap shear configuration as a test specimen. If local variations in the damage mechanism do not play a part in determining the locations of crack arrest, it is likely that arrest is determined purely by the mechanics of the situation. However, it must be noted that the fractographic work was done away from the edges of the specimen, while the crack arrest data was obtained at the edges, and that it is difficult to ascertain how much of an effect this had upon the results. A similar series of experiments, using photoelastic material to measure arrest lengths away from the edges, would be helpful in this regard.

A simple mechanical model has been proposed, which explains the phenomenon of crack arrest in purely mechanical terms, postulating an initial barrier to crack growth. Some supporting evidence for this model has been offered, but further study is necessary for substantiation of its assumptions.

## CHAPTER VI:

### CONCLUSIONS AND RECOMMENDATIONS

#### 6.1 The Short Beam Configuration

The analysis of the short beam configuration is fairly complete. The technique of mapping the fraction of strain to failure has been shown to predict both the modes and locations of failure in this configuration, and it has been shown that interlaminar shear failure is only one of many damage mechanisms at work. Indeed, interlaminar shear has been shown to play a minor role in precipitating final failure; the major damage modes are crushing and shear near the load nose and support, and chordwise tension beneath the load nose and below the midplane. Additional in-depth fractographic analysis is possible, to track the damage process from initiation to final failure. Interlaminar cracks are seen in these specimens, occurring both above and below the midplane, with their exact location varying from specimen to specimen, and the precise manner in which these crack develop is not understood. All that can be said with confidence is that initial damage is caused by the failure modes described, resulting finally in the production of visible interlaminar flaws

that proceed to the specimen ends. However, such in-depth analysis would be of questionable value. The purpose of this research has been to examine whether or not the three-point short beam bend test can be used to measure the interlaminar shear strength of composites, and that question has been answered: it does not, at least for specimens with quasi-isotropic layups. Thus, the test configuration is not applicable to its purpose, and there seems to be little to gain from analyzing it further.

By the same logic, the strain energy release rate analysis for the short beam configuration is of interest primarily for its potential applications to other configurations. The success of the contact stress model in determining strain energy release rates for cracks located near loads may find application where simple solutions for similar problems are needed. Future workers may wish to apply the technique used here— the use of the analysis of Williams, the approach to modelling the contribution of the contact stress field— to their areas of interest, to see if the results are of practical use. This question remains, because, ironically, the results of the strain mapping portion of the research have made analytical solutions for the short beam specimen an answer in search of a problem.

In summary, the problem of the short beam specimens that would not fail properly has been solved. While the general technique used to obtain strain energy release rate equations has potential for other applications, there seems to be little need for additional work upon the short beam configuration itself.

## **6.2 The Cracked Lap Shear Configuration**

Analysis of the cracked lap shear configuration is by no means so complete. The current effort suggests several areas for further work. The most interesting possibility would be to repeat the quantitative fractography and statistical analysis, using this time the observations of Reference 58 to divide the fracture surface into

opening-mode and mixed mode fracture. This might shed light upon the role played by mode split in the fracture behavior of the CLS specimen, an important issue which remains unresolved.

One question that has frequently been asked, when this work has been presented, is whether it is possible to automate the point counting technique. This is a good question, since the point counting process is very tedious and time-consuming. Increasing the speed at which the procedure could be performed would be a great step toward making it practically applicable. However, it seems unlikely that such automated point counting techniques are on the horizon. Automated point counting procedures exist, and are currently in use, but these are applied toward determining volume fractions of components with different chemical compositions. For the current application, it would be necessary to detect differences in more subtle aspects of appearance. Perhaps the field of artificial intelligence is capable of solving this problem, but it would be far more than an extension of current techniques.

It is important that this research has provided a demonstration of the potential of quantitative fractography and statistical analysis to contribute useful knowledge about composite fracture surfaces. Despite the inherent subjectivity of the method, it was used to contribute qualitative knowledge of the fracture surface that could be quantitatively substantiated. The variation of the thickness of the matrix layer along the crack plane was not obvious, particularly in the brittle-matrix specimens, yet the current approach detected it. Furthermore, it has been shown that the sample size at each distance from the crack starter can be reduced greatly, making the technique that much more practical. Theoretically, the sample size could be reduced still further, and future researchers may wish to experiment with this sample size to determine the minimum needed for consistent obtaining of useful data.

The effect of varying interlaminar matrix layer thickness upon the behavior of the CLS specimen is unclear. The current effort located variations in matrix layer thickness, but found no correlation between the locations of these variations and the regions of crack arrest, in all cases except one. However, there is the possibility that

resin thickness affects the fracture toughness values obtained from CLS specimens, particularly because of the effect of starter notch thickness.

The one instance in which the quantitative fractography did locate the arrest locations correctly— the case of specimen A— is difficult to explain away. It is especially difficult because the statistical analysis found a significant difference in the data between the two arrests and those outside that region. This significance was found when comparing two data sets totalling over 1,000 data points. It is unlikely that this is coincidental. This question points out the need for further work in the area of quantitative fractography of composite materials in general and of cracked lap shear specimens in particular.

The purpose of the simple mechanical model of arrest was to pose still more questions. Specifically, it was an attempt to explain the arrest phenomenon without invoking specific material behaviors that would cause the crack to stop growing. In this model, arrest is explained by loss of stiffness in the overall specimen, not by any events taking place in the vicinity of the crack tip. In fact, by postulating an initial barrier to crack propagation, this model suggests that crack arrest is more connected to the circumstances at the beginning of crack growth than to those at its end. Such a phenomenon could be due to the effect of the crack starter: its thickness can create resin pockets in the path of the crack, and its mechanical and bonding properties are different from those of the surrounding material. This work is only a beginning; the issue of why this initial barrier to crack growth exists is unresolved, and only one graph is presented to substantiate the model. A great deal of work remains, both in terms of theory and of database expansion, before this model can be judged.

## Appendix:

### Development of the Sublamine Model

The basis for sublamine modelling of composite material behavior is the variational formulation developed by Reissner<sup>[63]</sup>. Pagano<sup>[64,65]</sup> specified this formulation for the case of a laminated body, deriving a set of constitutive equations, equilibrium equations, and interface conditions for each layer of the laminate, as well as boundary conditions for the top, bottom, and edges of the laminate as a whole were derived. This led to a system of  $13N$  equations in  $13N$  unknowns, where  $N$  is the number of layers being considered in the system. This  $N$  may be different from  $\mathcal{N}$ , the number of plies in the laminate, because the analyst may choose to subdivide the plies into thinner layers for greater accuracy of solution, or he may assemble groups of plies into layers with smeared properties, for a more rapid solution. The latter course leads to the field of sublamine analysis.

It is important to note that the equations arising from the analysis of Reference 64 are ordinary differential equations, not linear equations. Thus, a system of  $13N$  such equations in  $13N$  unknowns becomes unwieldy for relatively small values of  $N$ .

The next step toward modern sublamine analysis methods was the global-local variational model developed by Pagano and Soni in Reference 48. Noting that



contemporary local models became intractable for even ten-ply layups (Pagano had tested his approach on two-ply layups in Reference 64, subdividing each ply into three sublayers), Pagano and Soni created a model that made it possible to combine local modelling of a particular region of interest with global modelling of the remainder of the structure. The form of the stress distribution in the locally-modelled region was assumed. Assumption of the form of the displacement field, a more convenient but less accurate assumption, was used for the global model.

The model of Reference 48 represents an attractive alternative to numerical approaches; however, further modification and simplification of its form was still useful. This led to the development of the sublaminar analysis, which has been most succinctly summarized by Armanios and Rehfield [66]. A sublaminar is simply a portion of the laminate that is considered as an homogeneous region. As in the global-local model of Reference 48, this unit can be a fraction of a ply, or it can be several plies, depending upon the rate of change of the stress state in the region to be analyzed. Additionally, plies can be divided normal to the midplane. An important difference between sublaminar analysis and the global-local analysis is that the former is based on a shear deformation displacement formulation within each sublaminar, of the form

$$\begin{aligned} u &= x_1 \epsilon + U(x_2) + x_3 \beta_1(x_2) \\ v &= V(x_2) + x_3 \beta_2(x_2) \\ w &= W(x_2) \end{aligned} \quad [A - 9]$$

where  $x_1$ ,  $x_2$ , and  $x_3$  correspond to  $x$ ,  $y$ , and  $z$ , respectively, in Figure 72.

Using this assumed displacement field, the following constitutive relations are derived:

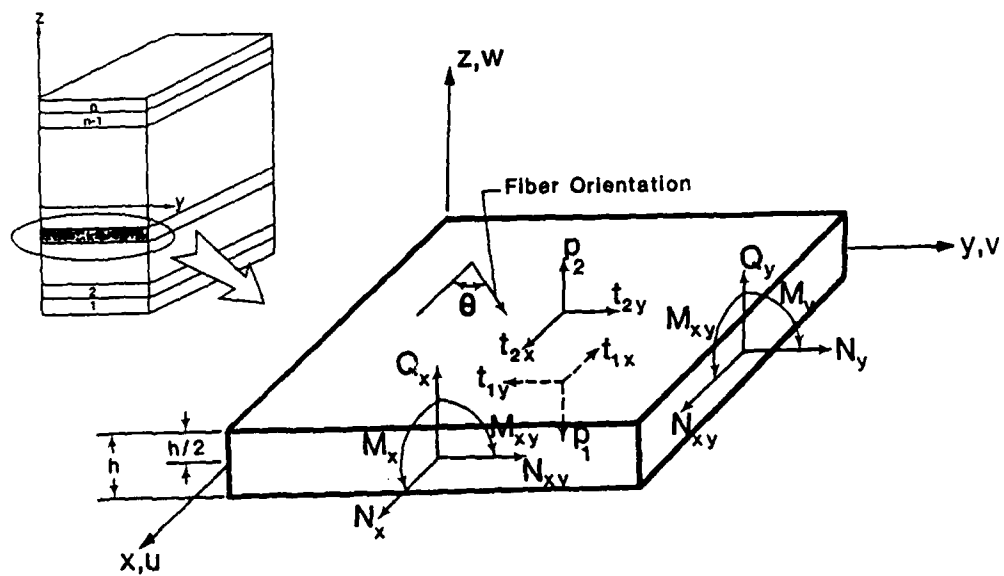


Figure 72. Notation and sign convention for a generic sublaminate

$$\begin{Bmatrix} N_{11} \\ N_{22} \\ N_{12} \\ M_{11} \\ M_{22} \\ M_{12} \end{Bmatrix} \begin{bmatrix} A_{11} & A_{12} & A_{16} & B_{12} & B_{16} \\ A_{12} & A_{22} & A_{26} & B_{22} & B_{26} \\ A_{16} & A_{26} & A_{66} & B_{26} & B_{66} \\ B_{11} & B_{12} & B_{16} & D_{12} & D_{16} \\ B_{12} & B_{22} & B_{26} & D_{22} & D_{26} \\ B_{16} & B_{26} & B_{66} & D_{26} & D_{66} \end{bmatrix} = \begin{Bmatrix} U_{,x_1} \\ V_{,x_2} \\ U_{,x_2} \\ \beta_{2,x_2} \\ \beta_{1,x_2} \end{Bmatrix} \quad [A - 10]$$

$$\begin{Bmatrix} Q_2 \\ Q_1 \end{Bmatrix} = \begin{bmatrix} A_{44} & A_{45} \\ A_{45} & A_{55} \end{bmatrix} \begin{Bmatrix} \beta_2 + W_{,x_2} \\ \beta_1 \end{Bmatrix} \quad [A - 11]$$

In addition, the equilibrium equations are found to be

$$\begin{aligned} N_{12,2} + \alpha_1 &= 0 \\ N_{2,2} + \alpha_2 &= 0 \\ Q_{2,2} + q &= 0 \\ M_{12,2} - Q_1 + m_1 &= 0 \\ M_{2,2} - Q_2 + m_2 &= 0 \end{aligned} \quad [A - 12]$$

where, using the nomenclature of Figure 72,

$$\begin{aligned} \alpha_1 &= t_{2x} - t_{1x} \\ \alpha_2 &= t_{2x} - t_{1y} \\ q &= p_2 - p_1 \\ m_1 &= \frac{h}{2}(t_{2x} + t_{1x}) \\ m_2 &= \frac{h}{2}(t_{2y} + t_{1y}) \end{aligned} \quad [A - 13]$$

Equations [A - 10], [A - 11], and [A - 12] are combined to form a system of

simultaneous coupled ordinary differential equations:

$$[\Psi] \begin{Bmatrix} U \\ V \\ W \\ \beta_1 \\ \beta_2 \end{Bmatrix} = - \begin{Bmatrix} \alpha_1 \\ \alpha_2 \\ -q \\ m_1 \\ m_2 \end{Bmatrix} \quad [A - 14]$$

where

$$[\Psi] = \begin{bmatrix} A_{66} \frac{d^2}{dx_2^2} & A_{26} \frac{d^2}{dx_2^2} & 0 & B_{66} \frac{d^2}{dx_2^2} & B_{26} \frac{d^2}{dx_2^2} \\ & A_{22} \frac{d^2}{dx_2^2} & 0 & B_{26} \frac{d^2}{dx_2^2} & B_{22} \frac{d^2}{dx_2^2} \\ & & -A_{44} \frac{d^2}{dx_2^2} & -A_{45} \frac{d}{dx_2} & -A_{44} \frac{d}{dx_2} \\ & & & (D_{66} \frac{d^2}{dx_2^2} - A_{55}) & (D_{26} \frac{d^2}{dx_2^2} - A_{45}) \\ \text{SYM} & & & & (D_{22} \frac{d^2}{dx_2^2} - A_{44}) \end{bmatrix} \quad [A - 15]$$

## REFERENCES AND NOTES

1. Press, Frank, "Advanced Materials and Competitiveness, *Metallurgical Transactions B*, vol. 21B (June 1990), pp. 415-418.
2. Ratwani, M.M., "Impact of Composite Materials on Advanced Fighters," *SAMPE Quarterly*, vol. 17 (January 1986), pp. 19-24.
3. Anderson, B.W., "The impact of carbon fibre composites on a military aircraft establishment," *Journal of Physics D: Applied Physics*, vol. 20 (1987), pp. 311-314.
4. Ugural, A.C., *Stresses in Plates and Shells*. New York: McGraw-Hill (1981).
5. Chan, W.S., and Ochoa, O.O., "Suppression of Edge Delamination in Composite Laminates By Terminating a Critical Ply Near the Edges," *29th Structures, Dynamics and Materials Conference*, Washington, D.C.: American Institute of Aeronautics and Astronautics, 1989, pp. 359-364.
6. Puppo, A.H., and Evensen, H.A., "Interlaminar Shear in Laminated Composites Under Plane Stress," *J. Compos. Mater.*, vol. 4 (1970), pp. 204-220.
7. Pipes, R.B., and Pagano, N.J., "Interlaminar Stresses in Composite Laminates Under Uniform Axial Extension," *J. Compos. Mater.*, vol. 4 (1970), pp. 538-548.
8. Pagano, N.J., and Pipes, R.B., "Some Observations on the Interlaminar Strength of Composite Laminates," *Int. J. Mech. Sci.*, vol. 15 (1973), pp. 679-

9. Pagano, N.J., and Pipes, R.B., "The Influence of Stacking Sequence on Laminate Strength," *J. Compos. Mater.*, vol. 5 (1971), pp. 50-57.
10. Pagano, N.J., "On the Calculation of Interlaminar Normal Stresses in Composite Laminates," *J. Compos. Mater.*, vol. 8 (1974), pp. 65-81.
11. Whitney, J.M., and Sun, C.T., "A Higher Order Theory for Extensional Motion of Laminated Composites," *J. Sound and Vibration*, vol. 30 (1973), pp. 85-97.
12. Reddy, A.D., Rehfield, L.W., Weinstein, F., and Armanios, E.A., "Interlaminar Fracture Processes in Resin Matrix Composites Under Static and Fatigue Loading," *Composite Materials: Testing and Design (Eighth Conference)*, ASTM STP 972, J.D. Whitcomb, Ed., American Society for Testing and Materials, Philadelphia, 1988, pp. 340-355.
13. Armanios, E.A., Rehfield, L.W., and Weinstein, F., "Understanding and Predicting Sublaminar Damage Mechanisms in Composite Structures, *Composite Materials: Testing and Design (Ninth Volume)*, ASTM STP 1059, S.P. Garbo, Ed., American Society for Testing and Materials, Philadelphia, PA, 1990, pp. 231-249.
14. Jordan, W.M., and Bradley, Walter L., "Micromechanisms of Fracture in Toughened Graphite/Epoxy Laminates," *Toughened Composites*, ASTM STP 937, Norman J. Johnston, Ed., American Society for Testing and Materials, Philadelphia, 1987, pp. 95-114.
15. Wang, J.T.S., and Dickson, J.N., "Interlaminar Stresses in Symmetric Composite Laminates," *J. Compos. Mater.*, vol. 12 (1978), pp. 390-402.
16. Wang, A.S.D., and Crossman, F.W., "Some New Results on Edge Effect in Symmetric Composite Laminates," *J. Compos. Mater.*, vol. 11 (1977), pp. 92-106.
17. Isakson, G., and Levy, A., "Finite-Element Analysis of Interlaminar Shear in Fibrous Composites," *J. Compos. Mater.*, vol. 11 (1977), pp. 422-428.
18. Rybicki, E.F., "Approximate Three-Dimensional Solutions for Symmetric Laminates Under Inplane Loading," *J. Compos. Mater.*, vol. 5 (1971), pp. 354-360.
19. Armanios, E.A., "New Methods of Sublaminar Analysis for Composite Struc-

tures and Applications to Fracture Processes," Ph.D. thesis, Georgia Institute of Technology, March 1985.

20. Armanios, E.A., and Rehfield, L.W., "Interlaminar Fracture Analysis of Composite Laminates Under Bending and Combined Bending and Extension," *Composite Materials: Testing and Design (Eighth Conference)*, ASTM STP 972, J.D. Whitcomb, Ed., American Society for Testing and Materials, Philadelphia, 1988, pp. 81-94.
21. Dattaguru, B., Everett Jr., R.A., Whitcomb, J.D., and Johnson, W.S., "Geometrically Nonlinear Analysis of Adhesively Bonded Joints," NASA-TM-84562, September 1982.
22. Whitcomb, J.D., and Dattaguru, B., "User's Manual for GAMNAS—Geometric and Material Nonlinear Analysis of Structures," NASA-TM-85734, January 1984.
23. Lubin, George, ed., *Handbook of Fiberglass and Advanced Plastics Composites*, New York: Van Nostrand Reinhold Company, 1969.
24. Whitney, J.M., and Browning, C.E., "On Short-Beam Shear Tests for Composite Materials," *Experimental Mechanics*, September, 1985, pp. 294-300.
25. Berg, C.A., Tirosh, J., and Israeli, M., "Analysis of Short Beam Bending of Fiber Reinforced Composites," *Composite Materials: Testing and Design (Second Conference)*, ASTM STP 497, American Society for Testing and Materials, Philadelphia, 1971, pp. 206-218.
26. Sandorff, P.E., "Saint-Venant Effects in an Orthotropic Beam," *J. Compos. Mater.*, vol. 22 (1980), pp. 199-212.
27. Whitney, James M., "Elasticity Analysis of Orthotropic Beams under Concentrated Loads," *Composites Science and Technology*, vol. 22 (1985), pp. 167-184.
28. Williams, J.G., "On the calculation of energy release rates for cracked laminates," *International Journal of Fracture*, vol. 36 (1988), pp. 101-119.
29. Lee, S.M., "Fracture of Adhesive Joints and Laminated Composites," *Polymer*

*Engineering and Science*, vol 27 (1987), pp. 77-81.

30. Kausch, H.-H., *Polymer Fracture*. New York: Springer-Verlag, 1978.
31. Rosen, Bernard, ed., *Fracture Processes in Polymeric Solids*. New York: Interscience Publishers, 1964.
32. Engel, L., Klingele, H., Ehrenstein, G.W., and Schaper, H., *An Atlas of Polymer Damage*. Englewood Cliffs, NJ: Prentice-Hall, 1981.
33. Hertzberg, R.W., *Deformation and Fracture Mechanics of Engineering Materials*. New York: John Wiley and Sons, 1983.
34. Bascom, W.D., Boll, D.J., Fuller, B., and Phillips, P.J., "Fractography of the Interlaminar Fracture of Carbon-Fibre Epoxy Composites," *J. Mater. Sci.*, vol. 20 (1985), pp. 3184-3190.
35. Newaz, G.M., "Transverse Toughness as a Material Characterization Parameter for Unidirectional Composites," *SAMPE Quarterly*, vol. 15 (January 1984), pp. 20-26.
36. Bascom, W.D., Ting, R.Y., Moulton, R.J., Riew, C.K., and Siebert, A.R., "The Fracture of an Epoxy Polymer Containing Elastomeric Modifiers," *J. Mater. Sci.*, vol. 16 (1981), pp. 2657-2664.
37. Bascom, W.D., Cottingham, R.L., Jones, R.L., and Peyser, P., "The Fracture of Epoxy- and Elastomer-Modified Epoxy Polymers in Bulk and as Adhesives," *J. Appl. Polym. Sci.*, vol. 19 (1975), pp. 2545-2562.
38. Johannesson, T., Sjöblom, P., and Seldén, R., "The Detailed Structure of Delamination Fracture Surfaces In Graphite/Epoxy Laminates," *J. Mater. Sci.*, vol. 19 (1984), pp. 1171-1177.
39. Richards-Frandsen, R., and Naerheim, Y., "Fracture Morphology of Graphite/Epoxy Composites," *J. Compos. Mater.*, vol. 17 (1983), pp. 105-113.
40. Armanios, E.A., Rehfield, L.W., and Reddy, A.D., "Design Analysis and Testing for Mixed-Mode and Mode II Interlaminar Fracture of Composites," *Composite Materials: Testing and Design (Seventh Conference)*, ASTM STP 893, J.M. Whitney, Ed., American Society for Testing and Materials, Philadelphia,



1986, pp. 232-255.

41. Hibbs, M.F., Tse, M.K., and Bradley, W.L., "Interlaminar Fracture Toughness and Real-Time Fracture Mechanism of Some Toughened Graphite/Epoxy Composites," *Toughened Composites*, ASTM STP 937, Norman J. Johnston, Ed., American Society for Testing and Materials, Philadelphia, 1987, pp. 115-130.
42. Salpekar, S.A., Raju, I.S., and O'Brien, T.K., "Strain-Energy-Release Rate Analysis of the End-Notched Flexure Specimen Using the Finite-Element Method," NASA-TM-100494 (also USAAVSCOM-TM-87-B-12), November, 1987.
43. Reeder, J.R., and Crews, Jr., J.H., "The Mixed-Mode Bending Method for Delamination Testing, *Proceedings of the 30th AIAA/ASME/ASCE/AHS/ASC/ASC Structures, Structural Dynamics and Materials Conference*. Washington, DC: American Institute for Aeronautics and Astronautics, 1989, pp. 1640-1647.
44. Johnson, W.S., and Mangalgiri, P.D., "Investigation of Fiber Bridging in Double Cantilever Beam Specimens," NASA-TM-87716, April, 1986.
45. Harris, C.E., and Morris, D.H., "A Fractographic Investigation of the Influence of Stacking Sequence on the Strength of Notched Laminated Composites," *Fractography of Modern Engineering Materials: Composites and Metals*, ASTM STP 948, J.E. Masters and J.J. Au, Eds., American Society for Testing and Materials, Philadelphia, 1987, pp. 131-153.
46. Rybicki, E.F., and Kanninen, M.F., A Finite Element Calculation of Stress Intensity Factors by a Modified Crack Closure Integral, *Engineering Fracture Mechanics*, vol. 9 (1977), pp. 931-938.
47. McCleskey, Stephen F., private communication, 31st AIAA/ASME/ASCE/AHS/ASC Structures, Structural Dynamics and Materials Conference, Long Beach, CA, April 2-4, 1990.
48. Pagano, N.J., and Soni, S.R., "Global-Local Laminate Variational Model," *Int. J. Solids Structures*, vol. 19 (1983), pp. 207-228.
49. Langhaar, Henry L., *Energy Methods in Applied Mechanics*. New York: John Wiley and Sons, 1962.
50. Ashton, J.E., and Whitney, J.M., *Theory of Laminated Plates*. Stamford, CT:

Technomic Publishing Co., 1970.

51. Lekhnitskii, S.G., *Theory of Elasticity of an Anisotropic Body*. Moscow: Mir Publishers, 1981.
52. Fugger, T.F., private communication with W.S. Johnson, NASA Langley Research Center, October 5, 1987.
53. Carman, C.D., private communication with W.S. Johnson, NASA Langley Research Center, August 28, 1987.
54. Miller, I., and Freund, J.E., *Probability and Statistics for Engineers*. Englewood Cliffs, NJ: Prentice-Hall, 1977. Ch. 10, pp. 275-279.
55. Gibbons, J. D., *Nonparametric Statistical Inference*. New York: McGraw Hill, 1971, pp. 140-149.
56. *ISI Sputterer-Coater Model PE-5000 Instruction Manual*. International Scientific Instruments, Inc., Mountain View, CA.
57. Miller, I., and Freund, J.E., *Probability and Statistics for Engineers*. Englewood Cliffs, NJ: Prentice-Hall, 1977. Ch. 9, pp. 264-265.
58. Yamashita, M.M., Hua, C.T. and Stumpff, P., "Expansion of Fractographic Data Base for Carbon Fiber Reinforced Plastics (CFRP)," *Proceedings of the International Symposium on Testing and Failure Analysis*. Metals Park, Ohio: ASM International, 1988, pp.289-297.
59. OBrien, T.K., private communication, July, 1990.
60. Miller, I., and Freund, J.E., *Probability and Statistics for Engineers*. Englewood Cliffs, NJ: Prentice-Hall, 1977. Ch. 3, p. 56.
61. Broek, David, *Elementary Engineering Fracture Mechanics*. Boston: Martinus Nijhoff Publishers, 1982.
62. Miller, I., and Freund, J.E., *Probability and Statistics for Engineers*. Englewood Cliffs, NJ: Prentice-Hall, 1977. Ch. 11, pp. 295-302.
63. Reissner, E., "On a Variational Theorem in Elasticity," *J. Math. and Phys.*,

vol. 29 (1950), pp. 90-95.

64. Pagano, N.J., "Stress Fields in Composite Laminates," *Int. J. Solids Structures*, vol. 14 (1978), pp. 385-400.
65. Pagano, N.J., *Stress Fields in Composite Laminates*. Air Force Materials Laboratory Report AFML-TR-77-114 (August, 1977).
66. Armanios, E.A. and Rehfield, L.W., "Sublaminar Analysis of Interlaminar Fracture in Composites: Part I— Analytical Model," *Journal of Composites Technology & Research*, Winter 1989, pp. 135-146.

## VITA

Bryan Hicks Fortson [REDACTED] He graduated in 1982 from the Massachusetts Institute of Technology, with a Bachelor of Science degree in Materials Science and Engineering. He entered active duty with the United States Air Force, serving as a materials research engineer with the Air Force Materials Laboratory at Wright-Patterson AFB, Dayton, Ohio. Concurrently he attended the University of Dayton, earning a Master of Science degree in Mechanical Engineering and a Master of Science degree in Management Science, both in 1986. He entered the Georgia Institute of Technology in the fall of 1986 to work for his Ph.D degree.

He is married to the former Michele Yvonne Byrdsong.